UNIVERSITÀ DEGLI STUDI DI PAVIA
FACOLTÀ DI INGEGNERIA
Dipartimento di Ingegneria Civile e Architettura

SHAPE MEMORY ALLOYS STRANDS: CONVENTIONAL 3D FEM MODELING AND SIMPLIFIED MODELS

Trefoli in Leghe a Memoria di Forma: Modellazione Convenzionale 3D FEM e Modelli Semplificati

Supervisor:
PROF. FERDINANDO AURICCHIO
Co - supervisor:
ING. MAURO FERRARO

Author:
VALENTINA MERCURI
UIN **406950**

Academic year 2013/2014

Alle mani di mio padre, cosumate dal lavoro,
era a loro che pensavo per restare sveglia
mentre scrivevo alle 4 del mattino

Acknowledgements

First of all I would like to thank my Supervisor Prof. Ferdinando Auricchio for his support during the course of this thesis. Working with him and his collaborators has been challenging but extremely exciting.
I'm deeply indebted with my co-Supervisor Mauro Ferraro for his invaluable patience and constant encourage in all hardest moments of this thesis. When something was wrong, he always had the right words to fix the situation and see things from a different point of view.
I also would like to thank Michele Conti for his help, for introducing me to the great world of supercomputing, unknown until few months ago and for his jokes always at right time.
I would like to acknowledge Walter la Carbonara and Biangio Carboni of *Università La Sapienza* for the material provided and clarifications about strand reference model.
It is a duty to thank the CINECA supercomputing center and all people of User support service for the fruitful correspondences. Special thanks are addressed to Maurizio Cremonesi whose suggestions have been more than essential to the conclusion of this thesis.

Abstract

This work of thesis focuses on the study of one of the most popular element in the construction industry and, more generally, in engineering: the strand. Because of their flexibility and high strength, strands are widely used throughout the mechanical, electrical, mining and naval engineering industries. These elements conventionally made of steel, have generated a renewed interest with the advent of so-called "smart materials". This special connotation has been associated to this materials since they can significantly change their mechanical properties (such as shape, stiffness and viscosity), or their thermal, or electromagnetic properties, in a predictable or controllable manner in response to their environment. Shape memory alloys (SMA) belong to this category and during recent years have aroused great interest among researchers for two main innovative properties: superelasticity and shape memory effect.

In this framework cables (or wire ropes) made from SMA wires are relatively new and unexplored structural elements. The purpose of introductory chapters of this work is to highlight the main advantages of linking SMA and conventional structural cables, showing the broad range of potential applications. Continuous improvement on finite element method (FEM) field has led to an increasing use of this tool in prediction of wire cable response. Although in scientific and technical literature several theoretical models of cables are available, these often lead to a partial description of cable behavior. Therefore, the potential of FEM approach make it clearly suitable to solve problems based on complex object such as strands.

In this thesis a particular type of strand having a specific geometric configuration is examined. The model comes from a project carried out by researchers of the Department of Structural and Geotechnical Engineering of *La Sapienza University*, Rome. This investigation concerns the development of a robust vibration absorber based on SMA and steel wire ropes assemblies, subjected to tensile and bending loads. This paper continues the study of SMA strands, with a particular emphasis on modelling aspects. In order to compare the response of steel and SMA materials, numerical simulations of the reference strand are performed. The studied models are generated using the finite element analysis Abaqus solver. Given the high computational cost related to the discretization chosen for the strand and the complexity of the problem considered, a cluster outfitted with different CPUs is required. For purposes of study, a simplified model for the modeling of wires and strands is proposed. This model is initially tested through simple problems and later implemented for the reference strand, previously mentioned. The simplified model is compared with 3D conventional one; finally some considerations about analysis results are reported.

Sommario

Il presente lavoro di tesi è incentrato sullo studio di uno degli elementi più conosciuti nell'ambito delle costruzioni e, più in generale, dell'ingegneria: il trefolo. Grazie alla loro flessibilità ed elevata resistenza, i trefoli hanno trovato largo impiego in campi ingegneristici come l'industria meccanica, elettrica, civile e navale. Questi elementi, convenzionalmente costruiti in acciao, hanno generato un rinnovato interesse con l'avvento dei cosìddetti "Smart materials". Questi materiali vengono definiti intelligenti poichè possono cambiare significativamente le loro proprietà meccaniche (come la forma, la rigidezza e la viscosità), termiche o elettromagnetiche in maniera controllata in risposta agli stimoli provenienti dall'ambiente circostante. Le leghe a memoria di forma (SMA) fanno parte di questa categoria e negli ultimi anni hanno destato grande interesse tra i ricercatori soprattutto per due proprietà innotive che le caratterizzano: la superelasticità e l'effetto a memoria di forma. All'interno del quadro descritto, i cavi (o funi metalliche) composti da fili in SMA, rappresentano elementi strutturali relativamente nuovi ed inesplorati. Lo scopo dei capitoli introduttivi è quello di evidenziare i principali vantaggi che si riscontrano nell'unire le SMA ai convenzionali cavi strutturali, mostrandone l'ampia gamma di applicazioni potenziali. Il miglioramento continuo nel campo degli elementi finiti (FEM) ha portato ad un crescente uso di questo strumento nel prevedere la risposta dei cavi. Sebbene in letteratura scientifica e tecnica siano disponibili diversi modelli teorici per trefoli e funi, spesso questi portano ad una descrizione parziale del loro comportamento. Quindi le potenzialità dell'approccio FEM lo rendono particolarmente idoneo per risolvere problemi riguardanti oggetti complessi come i trefoli.
In questo lavoro viene esaminato un particolare tipo di trefolo avente una specifica configurazione geometrica. Il modello nasce da un progetto sviluppato dai ricercatori del Dipartimento di Ingegneria Strutturale e Geotecnica dell' *Università La Sapienza di Roma.* Questa ricerca riguarda lo sviluppo di un dispositivo capace di assorbire le vibrazioni basato sull'assemblaggio di trefoli in acciaio e SMA, sottoposti a sollecitazioni di trazione e flessione. Il presente lavoro prosegue lo studio sui trefoli in SMA, rivolgendo particolare attenzione agli aspetti inerenti la modellazione. Nello specifico, vengono eseguite delle simulazioni numeriche per il trefolo di riferimento, volte a confrontare la differente risposta di una trefolo in acciaio rispetto ad uno in SMA. I modelli studiati sono stati generati utilizzando il software ad elementi finiti Abaqus. A causa dell'ingente costo computazionale legato alla discretizzazione scelta per il trefolo e alla complessità del problema considerato, è stato necessario ricorrere all'utilizzo di un cluster per l'uso in parallelo di più processori. A scopo di studio, viene proposto un modello semplificato per la modellazione di fili e trefoli. Questo modello viene testato inizialmente attraverso dei problemi semplici e successivamente implementato per il trefolo di riferimento. Il modello semplificato viene confrontato a quello convenzionale 3D. Si riportano in fine alcune considerazioni in merito ai risultati ottenuti dalle analisi eseguite.

Contents

List of Tables

List of Figures

Chapter 1

Introduction to shape memory alloy cables

The purpose of this first chapter is to highlight the main advantages of linking innovative materials, i.e., shape memory alloys (SMA)[1] and conventional structural cables.
Starting from an introduction on traditional structural cables geometry, composition and application fields, the general framework is completed with a brief historical evolution of smart materials and a survey of the principal SMA properties, focusing on the main reason of its extraordinary success on innovative applications. In order to motivate this work, the potential performance advantages of SMA structural cables over conventional metal cables are presented.
At the end of this chapter the aim and the structure of this thesis is described.

1.1 Structural cables

A common property to structural elements such as ropes, yarns, cords, cables and strands is their ability to resist relatively large axial loads in comparison to bending and torsional loads. Rope, because of this property, is one of the oldest tool that humans have used in their efforts to produce a better life for themselves and to achieve a technological improvement [1].

1.1.1 Construction and components

Conventional structural cables (or ropes) are made of thin filaments (or wires) of steel, natural or synthetic materials helically wound into strands, which in turn are wound around a core. The various components of a wire rope are shown in Figure 1.1; a brief definition for each single component is reported below.

- **Wire**: is a single, continuous length of metal (generally) cold-drawn from a rod.
- **Core**: the axial member of a wire rope about which the strands are laid. It may be fiber, a wire strand or an independent wire rope.
- **Strand**: an arrangement of wires helically laid around an axis;
- **Rope**: a plurality of strands laid helically around an axis or core.

The terms used to describe these component parts should be strictly adhered, in order to get clarity on the composition and to avoid misunderstandings when reporting on the conditions of

[1] In the following the acronym SMA for shape memory alloy is used

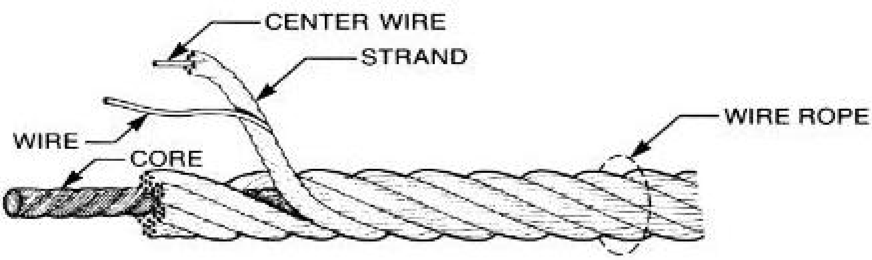

Figure 1.1: Wire rope components.

ropes. Describing wires as strands and strands as wire can be grossly misleading. For example, a report that a rope has a broken strand in most applications calls for immediate discarding of the rope, and subsequent cessation of its use, while a report that a rope has a broken wire in it should call for early inspection but seldom for discarding the rope.
The size and number of wires in each strand, as well as the size and number of strands in the rope greatly affect the mechanical behaviour of the rope. In general, a large number of small-size wires and strands produces a flexible rope with good resistance to fatigue bending. The rope construction is also important for tensile loading (static, live or shock), abrasive wear, crushing corrosion and rotation. Wire ropes are identified by a nomenclature referenced to: i) the number of strands in the rope; ii) the number(nominal or exact) and arrangement of wires in each strand; iii) a descriptive word or letter indicating the type of construction, i.e., the geometric arrangement of wires. Some examples of strands and wire rope patterns are reported in Figure 1.2 and Figure 1.3.

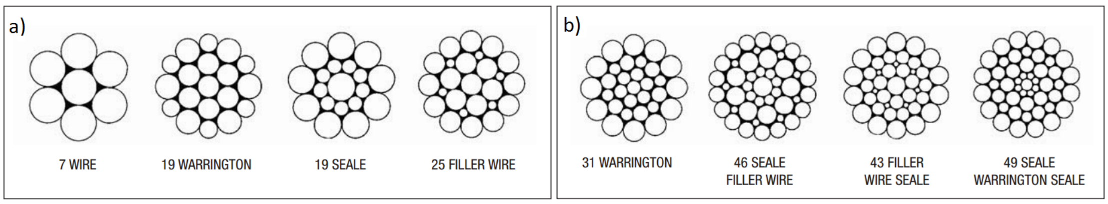

Figure 1.2: Strand cross sections: a) four basic strand patterns; b) combination strand patterns

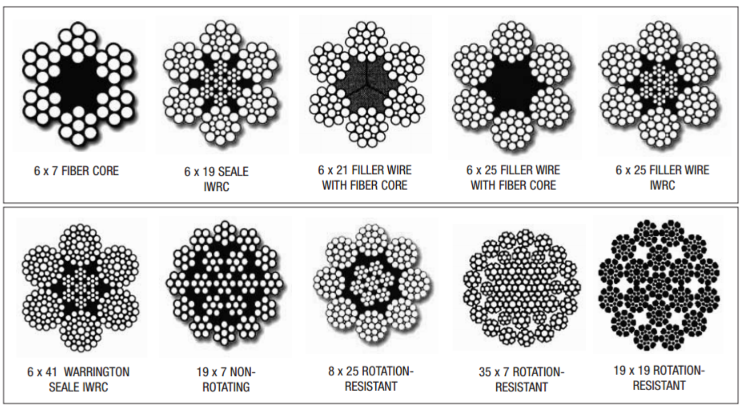

Figure 1.3: Cross sections of some commonly used wire rope constructions

The chirality of both the wires in a strand and of the strands in a rope can be laid in different way. Specifically, others significant technical terms are introduced, which are important in the comprehension of wire rope's structural organization.

- **Lay**: this could have two meanings (1) the way the wires in the strands and the strands in the rope are formed into the completed rope; (2) the length along the rope that one strand uses to make one complete revolution around the core.
- **Left Lay Strand**: a rope strand in which the cover wires are laid in a helix having a left-hand pitch; **Left Lay Rope**: a rope in which the strands are laid in a helix having a left-hand pitch.
- **Right Lay Strand**: a rope strand in which the cover wires are laid in a helix having a right-hand pitch; **Right Lay Rope**: rope in which the strands are laid in a helix having a right-hand pitch.
- **Regular Lay Rope**: wire rope in which the wires in the strands and the strands in the rope are laid in opposite directions. This type of configuration allows the wire rope to be compact, well balanced and with excellent stability.
- **Lang Lay Rope**: wire rope in which the wires in the strands are laid in the same direction that the strands in the rope are laid.

Figure 1.4 points out typical wire rope lay.

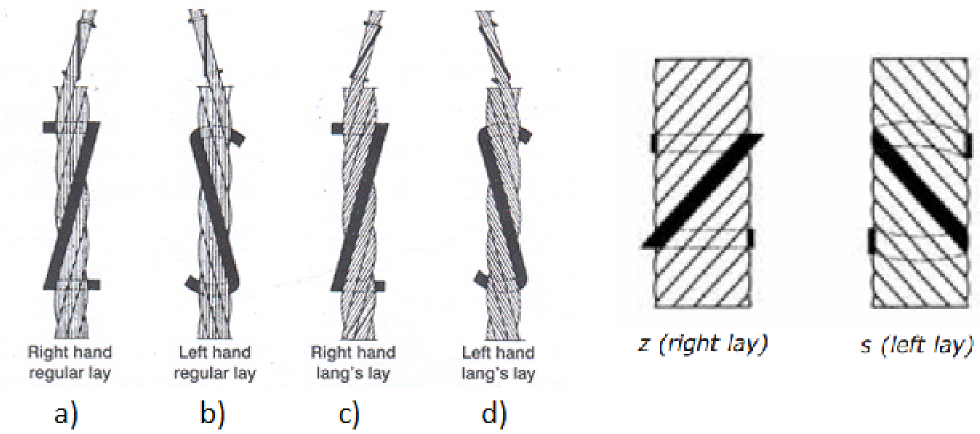

Figure 1.4: Configurations:a)RHOL(sZ),b)LHOL(zS),c)RHLL(zZ),d)LHLL(sS)

Note that the first lowercase letter in parenthesis,(caption of Figure 1.4), denotes strand direction and the second uppercase letter denotes rope direction.

1.1.2 Application fields

Wire ropes have been used for centuries as structural tension elements for a variety of applications. Due to their flexibility and high strength, these elements are nowadays used in:

- **Civil engineering structures** for power cables, bridge stays, and mine shafts;
- **Marine and naval structures** for salvage/recovery, towing, vessel mooring, yacht rigging and oil platforms;
- **Aerospace structures** for light aircraft control cables and astronaut tethering;

- **Electrical, heavy and mechanical industries** for electromechanical cables, lifting crane rope for lifting and moving material and equipment, indoor cranes and gantry cranes.

A vast range of problems is solved with strands and ropes. These elements are crucial components in all industries and economic sectors, starting from those of small-diameter such as disk drive head cables, up to those with larger diameters employed in the offshore oil rig lift.

1.2 General aspects of shape memory alloys

SMA belong to the category of the so-called smart materials, or responsive materials. The first problem encountered with these unusual materials is defining what the word "smart" actually means. This word describes something which is astute or 'operating as if by human intelligence' and this is what they are. From dictionary definition they are "materials that can significantly change their mechanical properties (such as shape, stiffness, and viscosity), or their thermal, optical, or electromagnetic properties, in a predictable or controllable manner in response to their environment" [2]. They respond to environmental stimuli with particular changes in some variables, e.g., temperature or magnetic fields and mechanical stress. SMA are materials in which large deformation can be induced and recovered through temperature changes (shape memory effect) or stress changes (pseudo-elasticity). Thanks to these innovative and potential properties, they are useful not only as structural elements, appreciable for their mechanical toughness, but they are also capable of fulfilling sensing and/or actuation functions.

1.2.1 A little bit of history

SMA are one of the most well known types of smart material and they have found extensive uses since their discovery in late '30s.
A shape memory transformation was first observed in 1932 in an alloy of gold and cadmium, and then later in brass in 1938. Particularly, the concept of thermoelastic martensitic transformation, which explained the reversible transformation in martensite, was introduced in 1949 by Kurdjumov and Khandros [3] based on experimental observations of the thermally reversible martensitic structure in CuZn and CuAl alloys.
Nevertheless, the great interest in the academic field, the reversible martensitic transformation and SMA had very little practical interest until 1962, when Buehler and co-workers discovered the properties of Nickel-Titanium (NiTi) alloy during an investigation for heat shielding. In fact, in addition to its good mechanical properties comparable to some common engineering metals, the material possessed the shape recovery capability. Following this observation, the term "NiTiNOL" was coined because it is made from nickel and titanium and its properties were discovered at the Naval Ordinance Laboratories. The term Shape Memory Effect (SME) was given to the associated shape recovery behavior.
In the wake of this discovery, in 1969, the world witnessed the first industrial application with the shape memory effect used on a sleeve of hydraulic lines in a fighter plane [4]. The effects of heat treatment, composition and micro structure were widely investigated and began to be understood during this period.
The slow acquisition of knowledge of the material and its thermomechanical behavior, coupled with the high production cost, caused difficulties in practical perennial use in the 1970s-1980s. Scientific research into the topic truly began in the 1980s, associated with the first experimental investigations and the earliest attempts at modeling. Unusual SMA macro behavior and properties imply non-conventional constitutive models. The traditional inelastic model do not provide an adequate description of complex behavior of this material, so a new class of inelastic models was developed, called *generalized plasticity* based on an internal-variable formalism. In fact, a consistent material model is strictly required as base of a computational tool reproducing SMA macroscopic behavior, helpful on the project of shape memory devices.
The discovery of Nitinol has spearheaded active research interest into SMA and many commercial applications have been developed, growing need for computational tools able to support design

process.

1.2.2 SMA properties

SMA have the ability to undergo reversible micromechanical phase transition processes changing their crystallographic structure. The name "shape memory material" suggest to the reader the main feature of these materials, i.e., the property of "remembering" thermic treatments to which they have been subjected. Specifically, SMA can associate a geometric shape to a particular thermic state (tipically high temperature). This property called *shape memory effect (SME)*, allows to recovery the original shape even when strains are presents with an heating process. Furthermore, at sufficiently high temperature they exhibit the *pseudoelasticity (PE)* or superelasticity, i.e. the recovery of large deformations during mechanical loading-unloading cycle[2].

In the following paragraphes, both SME and PE are described in detail. Furthermore, other secondary properties of engineering interest will be reported.

Shape memory effect and pseudoelasticity

PE and SME are related to reversible martensitic phase transformation, a solid-solid diffusion-less phase transformation between a crystallographically more-ordered phase, the *austenite* or *parent* phase, and a crystallographically less-ordered phase called *martensite*. Typically, the austenite phase is stable at lower stresses and higher temperatures, while the martensite is stable at higher stresses and lower temperatures.
In the stress-free state, SMA is characterized by four transformation temperatures: M_s and M_f (with $M_s > M_f$) during cooling and A_s and A_f (with $A_s < A_f$) during heating. While the former two indicate the temperatures at which the transformation from austenite into martensite (forward transformation) respectively starts and finishes, the latter are the temperatures at which the inverse transformation starts and finishes. The uni-axial thermomechanical response of SMAs can be summarized by the phase diagram shown in Figure 1.5 and the associated effects with the possible thermomechanical loading paths are discussed next.

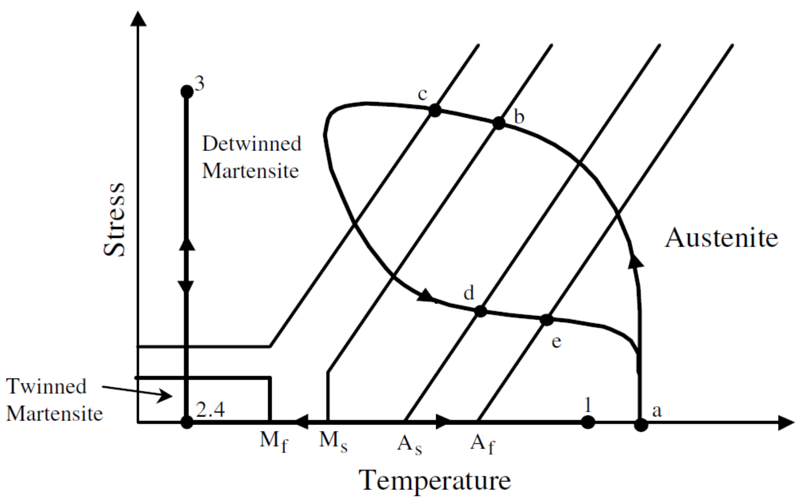

Figure 1.5: Stress–temperature diagram showing the relationship of stress and temperature and the austenitic and martensitic domains

The transformation from one structure to the other does not occur by diffusion of atoms, but rather by shear lattice distortion. Each martensitic crystal formed during martensitic transforma-

[2]In the following these abbreviations are used: SME for shape memory effect and PE for pseudoelasticity

tion can have a different orientation direction, called *variant*.
If there is no preferred direction during the transformation, the martensite takes advantage of the existence of different possible habit planes [3], forming a series of crystallographically equivalent variants. The product phase is then thermed *multiple-variant martensite* and is characterised by a *twinned* structure (Figure 1.6).

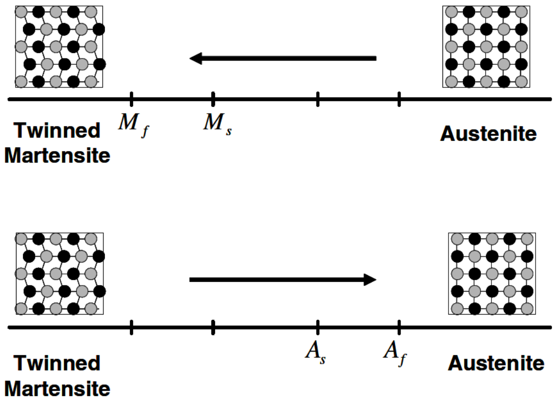

Figure 1.6: Temperature-induced phase transformation of SMA without mechanical loading(Lagoudas, 2008).

While, if there is a preferred direction for the occurrence of the transformation (often associated with a state of stress), all the martensitic crystals tend to be formed on the most favourable habit plane. The product phase is then termed *single-variant martensite* and is characterized by a *detwinned* structure [6] (see Figure 1.7).

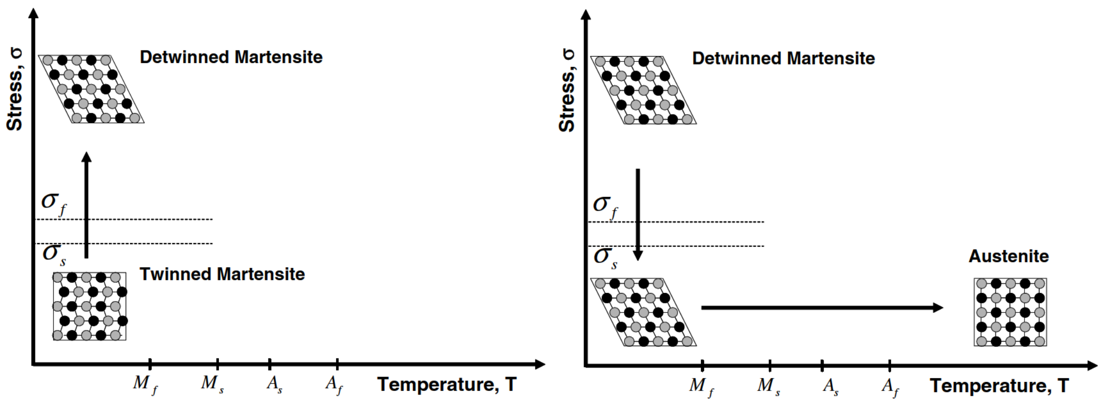

Figure 1.7: Schematic of the shape memory effect of SMA showing the detwinning of the material with an applied stress; Schematic of the shape memory effect of an SMA showing the unloading and subsequent heating to austenite under no load condition (Lagoudas, 2008).

When an unidirectional stress is applied to a martensitic specimen, there is a critical value whereupon the detwinning process of martensitic variants takes place [7]. The loading path 1-2-3-4-1, in which the SME is observed is shown in Figure 1.5. During the cooling of the parent phase (1-2) it transforms to twinned martensite. The material is then loaded (2-3) and the stress remains almost constant, until the martensite is fully detwinned. Further loading causes the ineleastic straining of the detwinned martensite. Upon unloading (3-4) the material remains in detwinned state and the large residual strains are not recovered. Finally, by heating above A_f (4-1), martensite transforms into austenite and the specimen totally recover the deformation and its initial undeformed

[3]The interface that separates the martensite from the parent phase is called the habit plane [5]

shape. This is the shape memory effect. The same path, schematically plotted in stress–strain temperature space is shown in Figure 1.8 (a).
Consider the specimen in the austenitic phase and at a temperature greater then A_f. Accordingly, at zero stress only the austenite is stable. If the specimen is loaded, remaining in isothermal conditions, the material present a non linear behaviour in the branch ABC as shown in Figure 1.8 (b), due to the stress induced conversion of austenite into martensite. Upon unloading, keeping again the temperature constant, since martensite is unstable without stress at temperature greater than A_f, a reverse transformation occurs (CDA), but at a lower stress level than during loading, producing an hysteretic effect. At the end of loading-unloading cycle,there is a spontaneously and completely recovery of the strain. This is the pseudoeasticity (or superelasticity) effect. The equivalent path (a-b-c-d-e) on the stress-temperature diagram is shown in Figure 1.5.

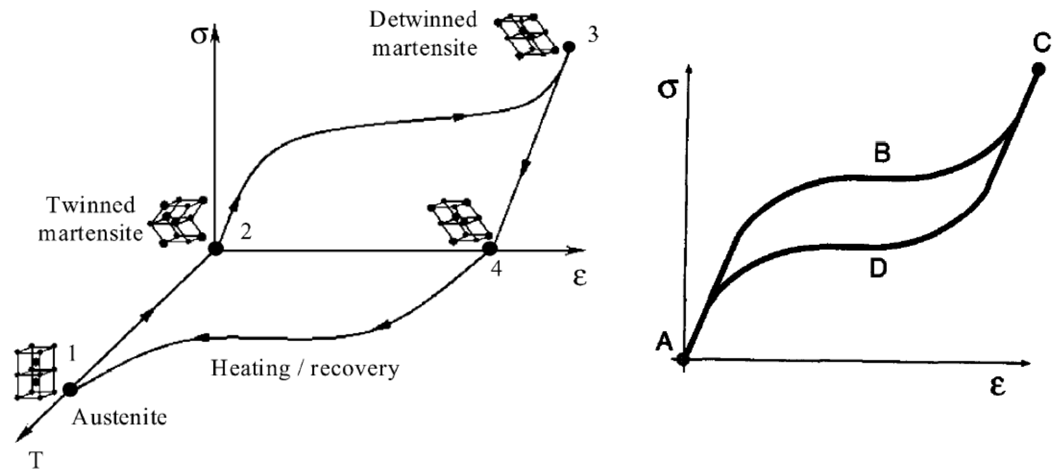

Figure 1.8: a) Shape memory effect; b) Pseudoelasticity

Additional SMA properties

SMA presents others remarkable properties, in addition to SME and PE, which are of great practical interest in a wide variety of applications.

- *Damping capacity*
- *Kink resistance*
- *Costant strain*
- *Fatigue behavior*

SMAs exhibit a *damping capacity*, the dissipation of mechanical energy into heat, that is far greater compared to standard materials. The high damping capacity of the thermoelastic martensitic phase is related to the hysteretic movement of interfaces (martensite variant interfaces, twin boundaries). This property is influenced by vibration frequency, temperature rates (heating/cooling) and strain amplitude. Recent literature reports that the martensite of Cu based alloys and Ni–Ti shows a damping capacity of at least an order of magnitude higher than classic structural metallic materials. For high amplitudes (10^-4), the loss factor in martensite can be of the order of 6–8%. During impact loading 10% and more can be obtained [8]. These aspects have generated a new interest for the damping capacity of SMA. Civil engineering applications are recently attracting more attention, especially for protection of civil constructions, such as buildings and bridges against earthquake vibration damage.

Another competitive feature of these alloy is the *kink resistance*, i.e., the capacity for which an excessive stress concentration is avoid through a more uniform strain distribution. When strains are locally increased beyond the plateau strain, stresses increased strongly. This causes strain to partition to the areas of lower strain, instead of increasing the peak strain itself. This phenomenon can be very dangerous in certain applications and it is not so uncommon in steel devices, particularly in metal cables. Under impact loading, steel cable is susceptible to "birdcaging", which is a bulbous-like permanent deformation mode that involves kinking of individual wire elements [9]. This is caused by excessive compression (often resulting from a dynamic event), and usually leads to scrapping of the cable. Kink resistance of SMA decreases the probability to incur ropes permanent damages.

A peculiar characteristic of the SMA stress-strain curve is the wide plateau that coincides with the ABC martensitic transformation. Due to this property of *constant strain*, if substantially ishothermical conditions persisted, is possible to carry out devices that applies a constant stress corresponding to a wide range of strain. As example for the civil engineering applications, the transformation plateau enables to design cables that have inherent overload protection for adjacent structures and large energy absorption capabilities under impact loading.

Since SMAs are widely preferred for actuation and sensing applications that require multiple cycles, involving repeated thermomechanical loading path, knowledge of fatigue behaviour is essential. The *fatigue behavior* depends on numerous factors such as fabrication process, heat treatments, type of loading (applied stress, strain, and temperature variations), alloy composition and microstructure. If a martensitic SMA is cyclically loaded, a large hysteresis loop is obtained, which is similar to that exhibited by conventional steels. However, the hysteresis of martensitic SMA is not to be ascribed to dislocation glide [4], but rather to the friction developed along the interfaces between martensitic variants, during their re-orientation, growth and shrinkage. This provides SMA's with a fatigue resistance much higher than a conventional plastically deformed metal [10]. Due to its excellent deformation behaviour and a very good fatigue resistance, Ni-Ti has been preferred to other SMA and successfully used in many investigations on damping [11]. The possibility of obtaining a very high fatigue resistance together with a stable and repeatable cyclic behaviour, makes SMA very attractive to be used in passive seismic control devices, dampers and actuators.

1.2.3 Application fields

Both traditional and innovative properties present in SMA, explain the increasing interest on these alloys. Although medical market have been the most successful field of application of SMA products, it must also be recognized that continuous efforts in material research have revealed the potential of those alloys for non-medical applications. The spread of SMA in different market areas requires perfect control of the material performance. The initial competition between Cu-based and Ni–Ti-based alloys has certainly contributed to a more detailed and fundamental research which finally lead to the superiority of Ni–Ti-alloys. A higher quality and reliability, combined with a significant decrease in prices allows moreover to consider new potential applications with tight budgets or cost factors [12].
The main fields of interest to the development of SMA devices are following reported, especially focusing on civil engineering area.

[4] Dislocation glide is the migration of a line defect along a glide plane, i.e. the plane in a crystal on which the movement occurs.

- **Medical technology**: stents, orthodontic wires, guidewires and automation systems, clinical instruments;
- **Electronic Engineering**: icebracking and weakening control of power cable, circuit-breakers and fixable fuses for transformers;
- **Aerospace Engineering**: couplings and flaps control on the trailing edge of aircraft wings;
- **Building security**: fire-stop valve, fire detection systems and automation systems;
- **Mechanical Engineering**: mechanical shock absorber, activators in several possible automotive applications, industrial piping tips and washers.

Although SMA have been known for decades, they have not been used much in the building industry until rather recently. The complete understanding of their extraordinary properties are still being developed; nevertheless the current state of the art provides an adequate basis for giving an overview of the possible applications of SMAs in civil structures.

- **Civil Engineering structures**: for passive, active and semi-active control of civil structures, for seismic protection devices, vibration control and pre-stressing or post-tensioning of structures with fiber and tendons, actuation and information processes essential to monitoring, self-adapting and healing of structures.

  Several studies relating to control of civil structures subjected to external dynamic loading, are available in the literature. Passive control devices, as example, take advantage of the SMA's damping property to reduce the response and consequent plastic deformation of the structures under severe loadings. SMAs can be effectively used for this purpose via two mechanisms: ground isolation system and energy dissipation system [13]. SMA isolator provides variable stiffness to the structure according to the excitation levels, in addition to energy dissipation and restoration after unloading; SMA energy dissipation element mainly aims to mitigate the dynamic response of structures by dissipating energy. SMA isolation systems include SMA bars for highway bridges, SMA wire re-centering devices for civil buildings, SMA spring isolation system and SMA tendon isolation system for a multi-degree-of-freedom(MDOF)shear frame structure. The SMA energy dissipation devices have been seen in the forms of braces for framed structures, dampers for cable-stayed bridges or simply supported bridges, connection elements for column and retrofitting devices for historic buildings.

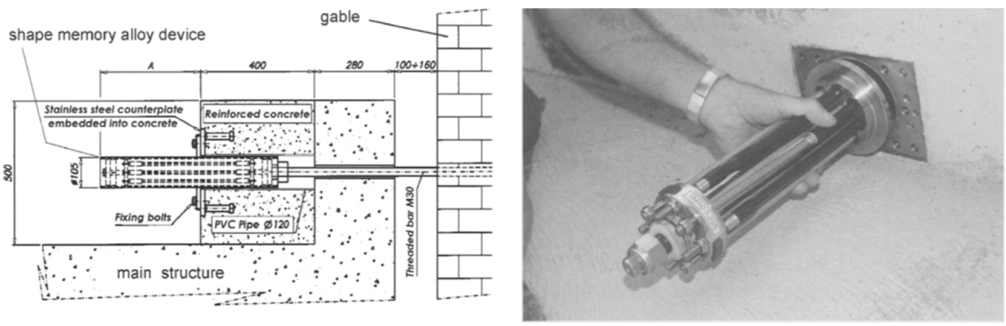

Figure 1.9: Shape memory alloy device used for the earthquake suitable connection of the historic gable and the main structure of the Basilica San Francesco in Assisi, Italy [14]

Related to monumental construction, an example of a real full scale application of a superelastic SMA device, is the earthquake resistant retrofit of the Basilica San Francesco in Assisi, Italy [14]. The historic gable was connected with the main structure by devices employing

SMA rods (Figure 1.9). Steel rods were traditionally used to prevent the typical monumental mechanisms of collapse. However, this technique often does not prevent the collapse but it only changes the mechanisms. Furthermore, steel bars high stiffness produces the transmission of large forces to the masonry wall, which may cause the breaking of the anchor for punching, especially with a deteriorated or poor-quality masonry. The purpose was to produce devices capable of preventing overturning, free from steel rods disadvantages.
These examples are just some applications of SMA products. New ideas for using SMA in civil engineering come from an improved concept for the active confinement of concrete members. As known wrapping columns with bands or sheets of steel or FRP [5] increases the load bearing capacity and ductility. Utilising the shape memory effect for tensioning the wrapping can enhance the effect of confinement. Tests on SMA confined concrete members were carried out by Krstulovic-Opara et al. in [15]. The calculations showed a lower axial strain for the active SMA confined column compared to the steel or CFRP [6] confined column at the same load.
Many of the mentioned applications, require the use of SMA wire cables . In an interest work of Reedlunn et al. [9] [16], advantages and potentials of SMA cables compared to conventional steel one are underlined, showing how cable structure have superior properties than a monolithic bar of comparable size. Wire ropes are relatively damage resistant, since failure of a single wire in a strand has less dramatic consequences than fracture in a monolithic bar. Furthermore, they have large design flexibility, due to the wide range of possible cross-section geometries and size, filament diameters and lay of individual components. They are relatively stiff in tension, yet flexible in bending and torsion, resulting in ease of handling and excellent fatigue performance under cyclic loads compared to solid bars of the same overall diameter. These features joined to SMA properties give rise to a promising way that could resolve numerous engineering task. SMA ropes are relatively kink resistant compared to steel cables, and transient overloading is less likely to incur in permanent damaged. The transformation plateau in superelastic behaviour could be exploited to design cables that have inherent overload protection for adjacent structure and large absorption load protection under impact loading. Furthermore, in the shape memory mode, they could be employed as thermally-active structural members. SMA cables have significant future as high forcer, thermal latches and shock absorber devices which could be useful for a number of infrastructure and transportation applications.

1.3 Thesis aim and organization

Several SMA applications have been reported in subsection 1.2.3 with particular emphasis on civil engineering area. In this framework cables (or wire ropes) made from NiTi SMA wires are relatively new and unexplored structural elements that combine many of the advantages of conventional cables with the adaptive properties of SMA (shape memory effect and superelasticity) and have a broad range of potential applications.
Starting from a project carried out by researchers of Department of Structural and Geotechnical engineering, *Università La Sapienza di Roma*, this work continues the study of SMA wire strands with particular emphasis on modelling aspects. As technology and computer sciences are developing and become more available, finite element analyses[7] start to be frequently used in predicting the wire rope behavior. Especially in this case, both for material complexity and to achieve a detailed description of strands mechanical behavior and response, 3D finite elements simulations are required. Due to problem complexity large computing resources are required. Within the LISA project[8], the PLX-GPU cluster of supercomputer center CINECA has been used for running all

[5]FRP: Fibre Reinforced Polymer
[6]CFRP: Concrete Fibre Reinforced Polymer
[7]In the following the acronyms FEA and FEM are respectively used for Finite Element Analysis and for Finite Element Method
[8]LISA project (Interdisciplinary Laboratory for Advanced Simulation) is an initiative promoted by Lombardia region and Consortium CINECA to support technological innovation and to increase the attraction of the Lombard

computing jobs.
The aim of the thesis is compare Steel and SMA strands response, within the framework of conventional 3D modelling. Three different meshed model has been carried out for the reference model. SMA and elastic materials have been implemented for both kind of mesh and corresponding analysis results have been compared to evaluate material behavior.
To the purpose of study, a simplified model has been investigated. Finite element selected for meshing the reference model is a brick solid element, used in conventional 3D modeling of solid structures. For the simplified model, beam and shell elements are chosen. Simple preliminary tests, performed on specimens subjected to different load cases, have led to the definition of the strand simplified model. For the simplified model linear elastic material (steel)has been used. The drastic reduction of degrees of freedom going from the first model to the second one, justifies the decrease of computational times, that is a constant challenge in the context of numerical 3D modelling. Despite this, there are clear strengths of the 3D model compared to the simplified one. Finite element strand models have been generated by the FEA (Finite Element Analysis) commercial solver Abaqus (Dassault Systémes, Providence, RI, USA). In addiction, Matlab program has been used to automatically generate simplified model geometry, mesh and constraints.
The content of the following chapters is summarized below:

- **Chapter 2**: after a quick literature review on constitutive model available for SMA superelastic behavior, theoretical modelization of Auricchio-Taylor model are presented. Material parameters chosen for SMA strand are reported. Finally, a simple numerical example, related to explicit FEA, is presented.

- **Chapter 3**: starting with an overview on authors using Finite element approach to predict the mechanical behaviour of cables and correlated modelling issues, the reference strand model is presented in detail. Referring to the strand problem developed by researchers at *Università La Sapienza di Roma*, geometric specifications, material assumptions and 3D modelling features are reported, in order to provide full knowledge of the starting model.

- **Chapter 4**: a simplified models is investigated as alternative to reference modelling approach based on 3D finite elements. Through simple tests carried out on single-wire and double-wire specimens, the simplified model is evaluated. A Matlab code that allows to implement automatically geometry and constraints of the simplified strand model is described. By using the over-cited code, a simplified model of the reference strand is created and subsequent compared to the corresponding 3D model.

- **Chapter 5**: comparison between steel and SMA strand is carried out, referring to the case of study described in chapter 3. High-performance computing tools of CINECA resources have been used to run all strands analysis. The System Architecture of these resources will be specified, focusing on IBM PLX cluster. A complete frame of the analysis performed on this server are provided, specifying each voice of requesting resources (i.e. number of CPUs, walltime etc.) and others fundamental job parameters. Three different mesh are considered for the strand in exam and mass scaling approach is addressed. Graphs and output in the variables of interest are reported for the jobs performed. Analysis results are compared to underline different material behavior.

- **Chapter 6**: conclusions about numerical results from models comparison and possible future research on topic are discussed.

---
territory through the exploitation of expertises and platforms for numerical modelling tools

Chapter 2

Auricchio-Taylor constitutive model for superelasticity

Starting from a brief review on available constitutive models for SMA, focusing on PE property prediction, the adopted Auricchio-Taylor model for the strand problem is described. It has been implemented in Abaqus to simulate the superelastic behavior of alloys such as Nitinol at finite strains. It is provided in the form of a built-in user material model for both VUMAT Abaqus/Standard and Abaqus/Explicit. This model has been well tested and performs robustly for all applicable elements. In the following chapters, SMA wire and strand tests are performed considering only PE effect; this will be taken into account during the parameters setting in Abaqus material definition. These parameters, used for all SMA simulations, together with a simple test on VUMAT, are here reported.

2.1 Toward Aurocchio-Taylor constitutive model

With the fundamental concepts of SMA behavior, introduced in the first chapter, the necessity to investigate methods by which SMA behavior might be accurately predicted become evident.
Several constitutive models for SMA have been proposed in literature during '90s. In 1990 C. Liang and C.A. Rogers presented a one-dimensional thermomechanical constitutive model for SMA, based on basic concepts of thermodynamics and phase transformation kinetics [17]. Within a subsequent paper [18] they studied a multi-dimensional model for SMA, considering a newly introduced internal state variable, the martensite fraction, instead of using the traditional plastic flow theory. Graesser and Cozzarelli used constitutive equations to model stress-strain response associated with martensitic twinning hysteresis and austenite-martensite/martensite-austenite superelasticity [19]. The presented equations express the growth of inelastic strain in a rate-type formulation similar to viscoplastic laws. Without claiming to represent all of the models studied, other examples can be found in [20] [21] [22] [23] [24]. Within his book [25], Lagoudas presents an accurate summary of the several thermomechanical models for SMA, investigated throughout the decades[1].

In 1995 the new family of inelastic models based on the concept of *generalised plasticity* is developed by Lubliner and Auricchio [26]. This theory based on an internal variables formalism and some fundamental axioms, includes conventional plasticity as a special case. This generality makes the model an adequate tool for representing constitutive materials with complex behavior. The work presented by Lubliner and Auricchio, represents a first attempt to apply generalised theory to the response of SMA. Within this framework Auricchio et al. have proposed a three-dimensional model for the superelastic behavior of SMA within a small-deformation regime. An extension of

[1] See chapter 3, section 3.6 "Overview of Other Thermomechanical Constitutive Models for SMAs".

this case is presented in [27], where the model is developed to reproduce always the PE effect but for a large-strain three dimensional model. This paper represents the base of the Abaqus user subroutine, for the definition of SMA material within Abaqus simulations. This set of work on isothermal pseudoelasticity is based on a multiplicative decomposition of the deformation gradient **F** in the form:

$$\boldsymbol{F} = \boldsymbol{F^e}\boldsymbol{F^{tr}}$$

where $\boldsymbol{F^e}$ is the elastic part of the deformation gradient and $\boldsymbol{F^{tr}}$ is an internal variable related to the phase transformations. Another assumption is to introduce a scalar parameter, ξ representing the single-variant martensite since in the model, not distinguishing between the different variants in which martensite may occur. A phase diagram based formulation is used and three phase transformation are considered: the conversion of austenite into single-variant martensite (A$\rightarrow$S), the inverse transformation(S$\rightarrow$A) and the reorientation of the single-variant martensite(S$\rightarrow$S). The model considers three-dimensional response using a Drucker-Prager-type surface[2] to model the pressure dependence of phase occurring in some alloys. An exponential hardening law is used, and focus is placed on finite element implementation of the model. They report a time-discrete isothermal version of the three dimensional problem, using a return-map algorithm as integration scheme, addressing the algorithmically consistent tangent.
The model, here briefly summarized, is explained in detail in [6,27], where the complete formulation is reported.

ABAQUS MODEL TIME-CONTINOUS FRAMEWORK

Control variables: $\boldsymbol{\varepsilon}$, T

where $\boldsymbol{\varepsilon}$ is the total strain and T the temperature.

Internal variables: $\boldsymbol{\varepsilon^t}$, ξ

where $\boldsymbol{\varepsilon^t}$ is the transformation strain tensor. *Constitutive equations*:

$$\Delta\varepsilon = \Delta\varepsilon^{el} + \Delta\varepsilon^{tr}$$

$$\Delta\varepsilon^{tr} = a\Delta\xi_S\frac{\delta F}{\delta\sigma}$$

$$F_s \leqslant F \leqslant F_s$$

where ξ_S is the fraction of martensite and F is a transformation potential.

The intensity of the transformation follows a stress potential law:

$$\Delta\xi_S = f(\sigma, \xi_S)\Delta F$$

The transformation potential follows a linear Drucker-Prager rule:

$$F = \bar{\sigma} - p\tan\beta + CT$$

where p is the pressure, β and C are material parameters.

[2]Drucker-Prager model is a simple yield function which models pressure sensitivity material by adding a linear pressure term to the von-Mises yield stress

2.2 Material definition for superelastic VUMAT

Within an Abaqus simulation is possible to use the option *USER MATERIAL to input material constants for use in a user-defined mechanical model. User subroutine UMAT is specific for Abaqus/Standard analysis, while user subroutine VUMAT is specific for Abaqus/Explicit analysis. All simulations in this work are carried out by Explicit method, thus the focus will be on VUMAT user subroutine.

2.2.1 Some specifications about VUMAT subroutine

The VUMAT subroutine simulating Ni-Ti alloys response is based on the overcited Auricchio-Taylor model. The superelastic behavior is defined on the uniaxial behavior shown in VUMAT user interface documents [28] [29]. This material is included in the model by using the over cited *USER MATERIAL option. The formulation uses 24 solution-dependent state variables (SDVs) in the elastic case, 31 when plasticity is included; this number is specified using the *DEPVAR option. The material data required as input are explained in the aforementioned user interface documents. Different behavior in tension and compression can be specified by providing ${\sigma_{CL}}^S$ (start of transformation during compression). The model also allows for user control of the volumetric transformation strain (${\varepsilon_V}^L$) in the cases for which there is different behavior in tension and in compression. If ${\varepsilon_V}^L$ is not specified, it is assumed to be zero and a non-associated Drucker-Prager type formulation is used. This is recommended as the default behavior, if such data is not available, since ${\varepsilon_V}^L$ is usually very small.
In Abaqus/Explicit the use of this material model requires the specification of 14 material constants on the data lines of the *USER MATERIAL option. The NAME parameter on *MATERIAL must be a specific name, connected to the finite element chosen for the simulation. 3D Solid elements are supported for use with the material model and the correlated NAME parameter is ABQ_SUPER_ELASTIC_N3D.
The material model can be used with analysis procedures that support mechanical behavior. The following procedures are commonly used in typical applications involving superelastic alloys: *STATIC, *COUPLED TEMPERATURE-DISPLACEMENT, *DYNAMIC, *DYNAMIC, EXPLICIT. The Nitinol VUMAT does not contain any non thread-safe statements such as data, save, and common. Thus, it is safe to use this VUMAT in parallel execution for both thread-based (mp_mode=threads) parallelization and MPI-based (mp_mode=mpi) parallelization [3].

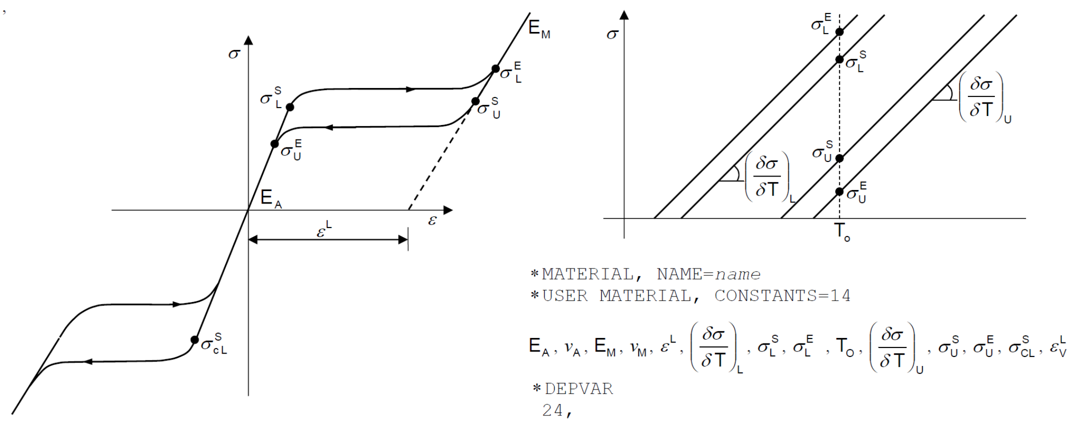

Figure 2.1: Superelastic behavior based on the uni-axial tension test

[3]MPI(*distributed memory*) and thread *shared memory*)options are communications protocol used in parallel computing environments. In computer science,(*distributed memory*) refers to a multiple-processor computer system in which each processor has its own private memory. In contrast, a *shared memory* multi processor offers a single memory space used by all processors.

2.3 Material parameters

For this work, the material parameters estimated by Auricchio's group [30] are adopted. These are shown in report [31], where the capabilities of three different SMA user-defined subroutines with a set of FEA involving different material behaviors are discussed. Material parameters are reported in Table 2.1. Estimated values of σ_L^S, σ_L^E, σ_U^S and σ_U^E must be rescaled because they are referred to the reference temperature value T_0. Also for Abaqus UMAT the ε^L value must be rescaled with the coefficient $\sqrt{\frac{2}{3}}$.

E_a	Austenite elasticity	53000 MPa
ν_a	Austenite Poisson's ratio	0.33
E_m	Martensite elasticity	53000 MPa
ν_m	Martensite Poisson's ratio	0.33
ε^L	Transformation strain	0.046
$\left(\frac{\delta\sigma}{\delta t}\right)_L$	$\delta\sigma/\delta t$ T loading	6.1 MPa/K
σ_L^S	Start of transformation loading	142 MPa
σ_L^E	End of transformation loading	282 MPa
T_o	Reference temperature	243 K
$\left(\frac{\delta\sigma}{\delta t}\right)_U$	$\delta\sigma/\delta t$ T unloading	6.1 MPa/K
σ_U^S	Start of transformation unloading	92 MPa
σ_U^E	End of transformation unloading	− 108 MPa
σ_{CL}^S	Start of transformation stress during loading in compression	142 MPa
ε_V^L	Volumetric transformation strain	0.046

Table 2.1: Material parameters

2.3.1 A simple test on SMA VUMAT parameters

In this section a simple test is reported to underline PE property of SMA and verify chosen parameters for the models in exam. Explicit procedure is chosen for the simulation.
A three dimensional unit cube ($1mm \times 1mm \times 1mm$) is tested under a uniaxial loading-unloading cycle, both in tension and compression, as showed in Figure 2.1. The cube consists on a single finite element. The mesh discretization consists in a unique eight-node brick element with reduced integration (C3D8R).
It is constrained with proper boundary conditions defined in the default Abaqus *initial step*[4], with symmetry conditions correlated to uniaxial loading test. A displacement of 0.065 mm is applied along z direction in the nodes belonging to the free face of the cube. This BC is created within the *Displacement* step (total time equal to 1 seconds) and associated to the *Test* amplitude that allow allows arbitrary time variations of displacement. This amplitude consists of a ramp that

[4]See section 3.2.3

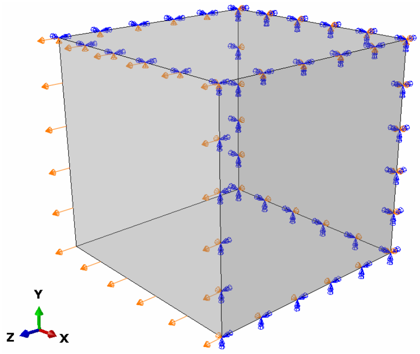

Figure 2.2: SMA cube subjected to uniaxial test

goes from 0 to 1 (at time t1 = 0.25 s) and then returns to 0 (t2 = 0.5 s); the same path with negative sign (-1 at t3 = 0.75 s) there is during the "unloading" phase.

The material associated to the solid section is ABQ_SUPER_ELASTIC_N3D, which parameters are reported in Table 2.1. Nodal temperature are kept constant during the analysis and tests are conduced at three different temperatures (270 K, 290 K, 310 K).
The results of tests made on Abaqus VUMAT for PE behaviour are reported in Figure 2.3. The stress-strain diagrams show the conventional SMA behavior. Tests performed at different temperatures underline the stress-temperature linear relationship.

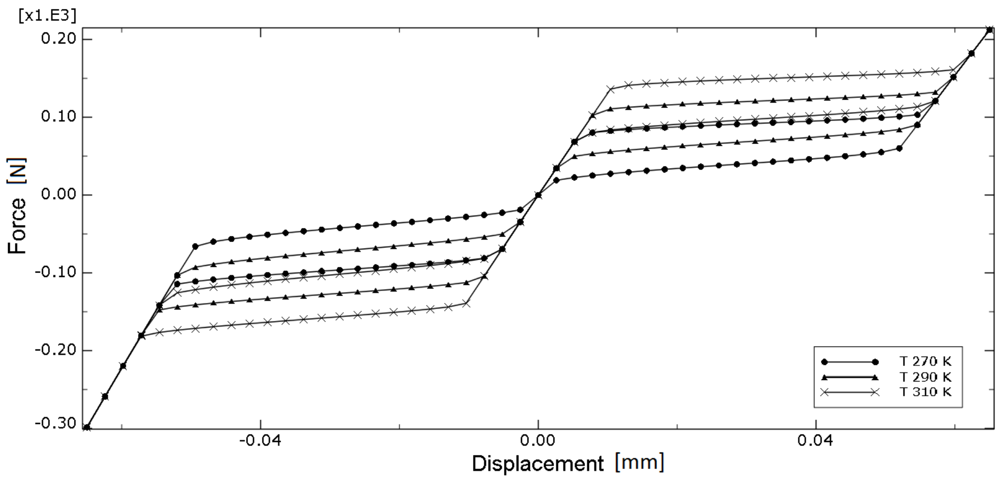

Figure 2.3: Force-displacement diagram computed with superelastic VUMAT at different temperatures

Chapter 3

Conventional 3D strand modelling

Continuous improvement on FEM field, led to an increasing use of this tool in the description of wire cables response. In the present chapter a brief review on finite element approaches embedded in wire rope analysis is presented.
Many types of wire ropes and strands are currently in use, for this reason is unimaginable to accurately model every assembly and material used in the construction of wire cables. A particular strand with a specific geometrical configuration is examined. This model comes from an investigation about the development of a robust vibration absorber based on SMA and steel wire ropes assemblies, subjected to tensile and bending loads. The goals of this project, carried out by W. La Carbonara and B. Carboni from *Università La Sapienza di Roma*, are:

- investigate a new class of non-linear hysteretic behaviors by coupling the damping due to phase transitions of SMA, friction between wires and stretching-induced geometric non-linearity;
- obtaining families of constitutive behaviors with three mechanisms integrated together in one rheological device.

Starting from La Carbonara and Carboni research work, the strand reference model is discussed, describing the different steps of modelling. At the end of chapter, model characteristics that make it computationally expensive are illustrated. Motivated by these considerations, the idea of a simplified strand model is introduced and discussed in detail in chapter 4.

3.1 Review of ropes modelling

Steel cables were first used in the German mines of the Harz Mountains in 1836 [32]. Ever since, they have been widely employed for many different applications and engineers have tried to predict geometry and properties of ropes by analytical methods.
In scientific and technical literature several theoretical models of cables are available. In this fields, a real pioneer is Hruska, whose work dates back to the early 50s. The author worked out a simple theory for the calculation of stresses, radial and tangential forces in wire ropes. Benefiting from Kirchhoff-Love's theory [33], Costello [1] and later Utting and Jones [34, 35] have followed a more fundamental approach, making different assumptions relative to the rope geometry and the inter-wire contact condition. Utting and Jones' analysis includes contact deformations and friction effects, whereas in Costello's such phenomena are neglected. Considering multi-layered strands in offshore applications, Hobbs and Raoof [36] have introduced a quite different approach in which the characteristics of each layer, including the internal friction phenomena, are homogenized. Feyrer investigates the behavior and fatigue properties of wire ropes under tensile load and also behavior of wire ropes under bending and tensile stresses in his book, in which his theoretical and experimental studies are collected [37].
Due to the complex build-up of wire cables and their non-linearity in geometry and material,

prediction of wire cables response has only been partially achieved. It often resulted in complex relations which additionally rely on assumptions and varies generally unknown parameters [38]. Furthermore, using the analytical solutions of the wire rope theory it is not possible to analyse and get the results at any specific point of the model. Therefore finite element approach become clearly adapted to solve this problem.

Finite element predictions of rope properties started at the beginning of the 70s. During these years, FEM was used for the study of cables by Carlson and Kasper [39], who built a simplified model for armored cables. In 1996, Chiang [40] modelled a small length of a single strand cable for geometric optimization purposes. Standard volumic finite elements are used for mesh, although these elements are not suitable for the study of all the inter-wire motions (rotations and displacements). Furthermore, as the accurate modeling of a cable requires a large number of elements, an accurate description of the cable behavior is often not possible. With the goal of decrease these costs, Jiang et al. [41] proposed a concise finite element model for cables using three-dimensional solid brick elements, which takes benefit from the structural and loading symmetries. In order to extend the range of applications of the finite element models, Durville [42] designed a specific finite element for cables undergoing large deformations with inter-wire friction interaction. A special emphasis is put on the modeling of contact, based on an a priori discretization of the contact problem, independently of the finite element discretization of the structure. In following studies, Durville carried on the automatic creation approach of contact elements, reporting numerical tests for randomly generated samples of entangled materials [43]. Using advanced 3D modeling techniques, G.M. Kastratović et al. [44] explored FEA of IWRC[1] (see Figure 3.1 and 3.2), focusing on several types of contacts between wires and using different meshed 3D models.

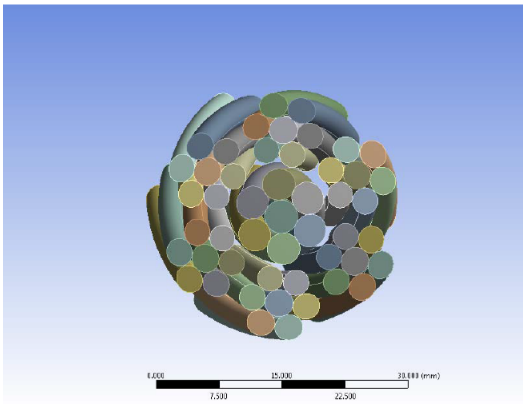

Figure 3.1: Cross section of IWRC [44]

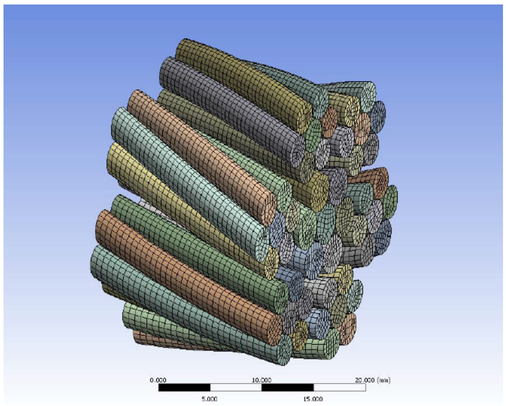

Figure 3.2: 3D Finite Element IWRC Model mesh [44]

Others modeling schemes for IWRC are proposed by C. Erdönmez and C.E. İmrak in [45] [46]. These authors also created a realistic 3D structural model for a wire strand and reported numerical results for axial loading and bending over a sheave problems, reported in Figure 3.3. G. Shibu et al. [47] conduced FEA of a three layered straight wire rope, placing the accent on the linear elastic global behaviour of steel strand under small strain. Gerdemeli et al. [48] investigated with FEM fatigue life of axial loaded wire rope in computer environment. In the scientific and technical literature there is a lack of information on the rope behaviour during fire. To this purpose, Fontanari et al. [49] proposed a methodology for determining fire resistance of metallic wire ropes for ropeways and civil applications. A FE parametric model was built up both for a full-locked rope and a for a Warrington-Seale strand rope, to simulate the devices response to heavy thermal

[1]IWRC is the acronym for Independent Wire Rope Core, a special component of complex wire rope. It is used as a rope by itself in some rare applications but commonly it is used as a core for more complicated designs of wire ropes such as Seale IWRC and Warrington IWRC (see Figure 1.2 and 1.3 in chapter 1).

transients resembling a fire scenario.

The examples reported represent only a small portion of the total FE studies conduced to analyse wire strands behaviour in the wide range of problem cases linked to ropes and cables applications. In the recent years, the developments in finite element software as well as in computer technology, have made it much more feasible not only from a scientific but also from a practical point of view.

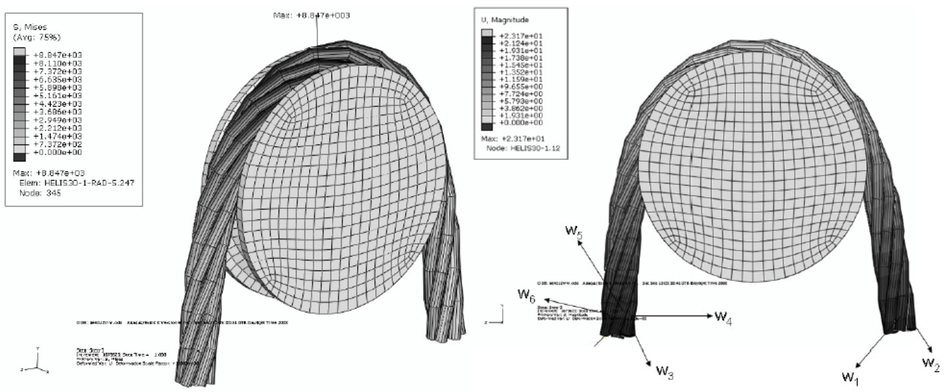

(a) Von-Misses stress (b) Deformation

Figure 3.3: Stress and deformation distribution of the wire strand bent over a sheave [50]

3.2 Strand reference model

In the present work, the model chosen as refence model is a three layered straight strand having a total diameter of 3cm: it is made from a central straight wire (core) and two outers layers, respectively composed by 6 and 12 wires helically wrapped around the central wire. The first layer is wrapped in right-hand way with a pitch length of 15.7 mm, while second layer is wrapped in left-hand way with a pitch length of 25.7 mm. The lay of the wires in layer 1 is opposite to the lay of the wires in layer 2 in order to to reduce the axial twisting moment in the strand.
The goal of the model is to describe a hysteretic load-displacement cycle in the transverse direction to the rope axis, after a pretension of the strand. One end of the strand is fixed, while the other one is initially subjected to a longitudinal displacement and then to a transversal displacement respect the rope axis. This analysis is executed using the Abaqus/Explicit solver under the assumption of quasi-static regime.
The strand structure has been constructed using the commercial software Autocad and then imported to Abaqus/CAE software for FE analysis. To better understand the problem in object, in Figure 3.4 is represented the strand cross section organization.

3.2.1 Strand construction and geometry

Geometric validation of the strand and calculus of wires radius is obtained by means of Costello's study. Following, the adopted relations are briefly illustred.

Costello's equations

The configuration and cross section of a loaded simple strand is shown in Figure 3.5. For initial condition the strand include a center wire of radius R1, surrounded by m helical wires of radius R2. It is assumed that the center wire is of sufficient size to prevent the outer wires from contact each other in order to minimize the effect of friction in the bending of the strand [1].

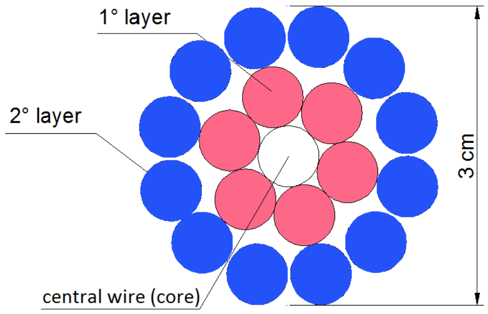

Figure 3.4: 12+6+1 straight strand cross section

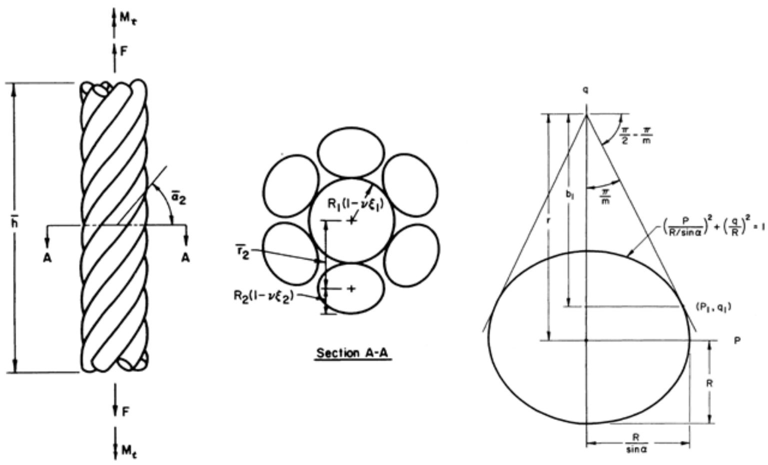

Figure 3.5: Loaded simple straight strand and and wire cross section perpendicular to axis of strand [1].

The initial radius of the helix for an outer wire is given by the expression:

$$r_1 = R_1 + R_2$$

The initial helix angle α_2 of an outer wire is determined by the expression:

$$\tan \alpha_2 = \frac{p_2}{2 \cdot \pi \cdot r_2}$$

where p_2 is the initial pitch of an outer wire. An expression is derived to determine the minimum value of R_1 in order to prevent the outer wires from contact each other. A wire cross section in a plane perpendicular to the strand is shown in Figure 3.5. Since the wires are thin, the equation of cross section can be assumed as elliptical and (p,q) is any point on the ellipse. Hence,

$$\left(\frac{p}{R/\sin \alpha}\right)^2 + \frac{q}{R}^2 = 1$$

$$\frac{dq}{dp} = \pm \frac{p \cdot \sin^2 \alpha}{R\sqrt{1 - \left(\frac{p \cdot \sin \alpha}{R}\right)^2}}$$

Also at the point (p_1, q_1) the slope is equal to $-\tan\left(\frac{\pi}{2} - \frac{\pi}{m}\right)$ as shown.

Hence, the solution for (p_1, q_1),

$$\tan\left(\frac{\pi}{2}-\frac{\pi}{m}\right)=\frac{p\cdot\sin^2\alpha}{R\sqrt{1-\left(\frac{p\cdot\sin\alpha}{R}\right)^2}}$$

$$p_1=\frac{R}{\sin\alpha}\tan\left(\frac{\pi}{2}-\frac{\pi}{m}\right)\frac{1}{\sqrt{\sin^2\alpha+\tan^2\left(\frac{\pi}{2}-\frac{\pi}{m}\right)}}$$

$$q_1=\frac{R\cdot\sin\alpha}{\sqrt{\sin^2\alpha+\tan^2\left(\frac{\pi}{2}-\frac{\pi}{m}\right)}}$$

In Figure 3.5 it is shown that $r=b_1+q_1$. Hence,

$$b_1=b_1\tan\left(\frac{\pi}{2}-\frac{\pi}{m}\right)$$

$$r=R\sqrt{1+\frac{\tan\left(\frac{\pi}{2}-\frac{\pi}{m}\right)}{\sin^2\alpha}}$$

The last equation defines the radius of the wire helix in which the wires are just in touch with each other. Hence, in order not to be in contact outer wires with each other the following equation must be valid:

$$R_2\sqrt{1+\frac{\tan\left(\frac{\pi}{2}-\frac{\pi}{m}\right)}{\sin^2\alpha}}<R_1+R_2$$

The presented relation can be extended to multi-layered strands. Considering the addition of another layer, as in the designed strand, an extension of the previous considerations results in the equation of the third radius:

$$r_3=R_1+2R_2+R_3$$

Geometrical parameters, chosen for the strand reference model, are reported in table 3.1 (see also Figure 3.6 and Figure 3.7).

Geometrical parameters			
$D_{tot}[mm]$	30	$p_1[mm]$	15.7
$R_1[mm]$	0.3	$p_2[mm]$	$(-)25.7$
$R_2[mm]$	0.3	α_1	76.21
$R_3[mm]$	0.295	α_2	73.61
$R_{3^*}[mm]$	0.313	$r_1[mm]$	0.613
m_1	6	$r_2[mm]$	1.203
m_1	12	$L_{tot}[mm]$	62.8

Table 3.1: Geometrical parameters

For the central core and the outer wires of the first layer a circular section has been defined, while for the second layer, wires present an elliptic section. For the particular strand in exam, relations are applied in order to allow a minimum contact between elliptic wire sections, accepting small overlaps in the initial configuration state.

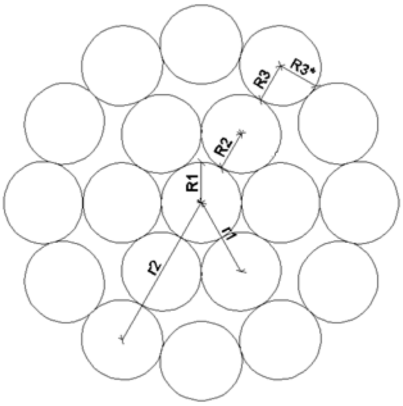

Figure 3.6: Radius of wires in the cross strand section

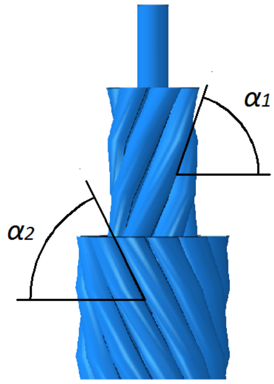

Figure 3.7: Angles of outer helical wires rotation

The first step of a modelling using Abaqus/CAE, is the definition of *parts* that will form the *assembly* of the model. In this case, since different sections have been chosen for the core and the wires of the outers layers, parts creation requires particular care. To define each part of the model, dates obtained from Costello's equations are used to draw the strand base section in Autocad. The presence of contact between wires causes some problems in modelling phase; importing the strand section as an unique part, wires overlaps generate errors. To solve this problem 4 distinct parts have been created:

- "CORE" part for the central core;
- "LAYER1" part for the first outer layer;
- "LAYER2-1" and "LAYER2-2" parts for the second outer layer, each part containing the 6 elliptic wires alternating not in contact.

In program Abaqus is not possible to create directly elliptical sections, neither to extrude these sections imported from Autocad. Thus, in Autocad dxf.file are simply reported the axes (minor and major) of the ellipses. Then, during the sketch phase, these are drawn on the reference axes imported from Autocad.
In Figure 3.8 are grouped the four parts created and the assembly view:

The geometry of the core has been obtained by a linear z-axis extrusion. Each wire has been generated by the extrusion of the cross section along a helix corresponding to the centroidal line of the wire.

3.2.2 Material, mesh and interaction property definition

Once created the different parts, a solid section with a circular profile is assigned to each wire. A material definition is used to define the material properties of the section which is then associated with the section definition. Linear, isotropic and elastic steel material is chosen. Material properties are summarized in the following table.

Young modulus $E[N/mm^2]$	210000
Poisson's ratio ν	0.3
Density $\rho[Kg/mm^3]$	$7.86 \cdot 10^{-6}$

Table 3.2: Material properties

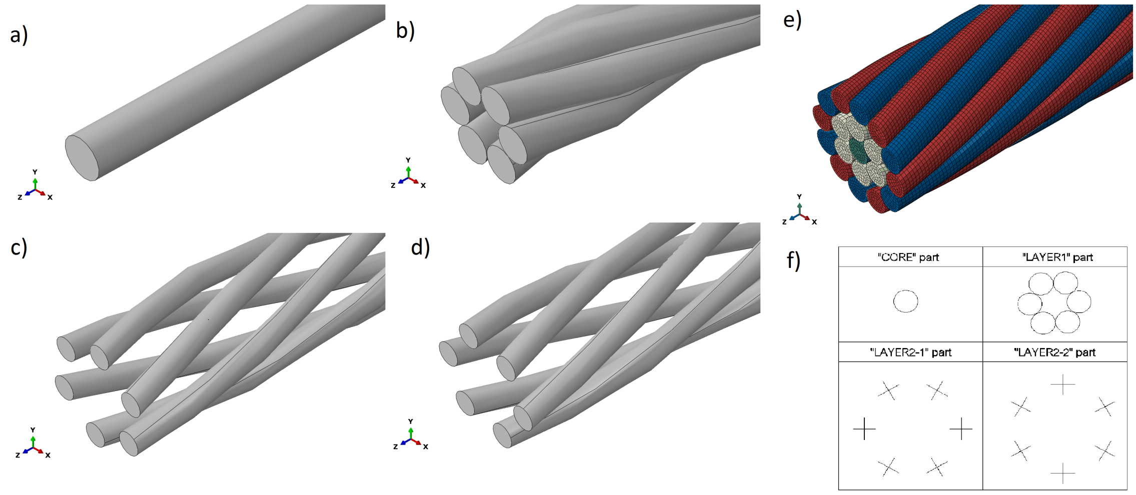

Figure 3.8: Model parts: a) "CORE" part; b) "LAYER1" part; c) "LAYER2-1" part; d) "LAYER2-2" part; e) Assembly view; f) parts sections imported from Autocad

A wide choice of element formulations is available in Abaqus. In this model, eight-node linear brick, reduced integration, hourglass control type element (C3D8R element) is used for structural discretization (see Figure 3.9). All of the stress/displacement continuum elements have translational degrees of freedom at each node. A dense mesh is generated for the model, with a total number of nodes equal to about $1 \cdot 10^6$ ($3 \cdot 10^6$ DOFs).

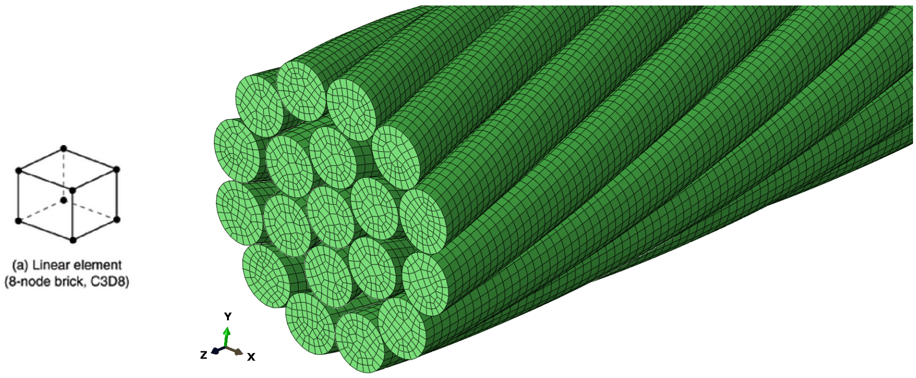

Figure 3.9: Model discretization

Contacts between wires exist and must be taken into account. Solid sections can be in contact with each other in an Explicit analysis. Within the *Interaction Module* an *Interaction Property* is defined, selecting *Tangential Behavior* among mechanical properties and specifying *Penalty Friction Formulation* with friction coefficient equal to 0.5. The *General contact (Explicit)* type of interaction is created for the model, associating to it the interaction properties previously defined and selecting the option *All with self.* In this way Abaqus considers possible contact between any element of avoiding the difficult identification of the slave and master surfaces required in the classical formulations of the contact problem. General contact algorithm allows very simple definitions of contact with very few restrictions on the types of surfaces involved. Penalty contact method is used to enforce contact constraints, which searches for node-into-face and edge-into-edge penetrations in the current configuration. General contact in Abaqus/Explicit can effectively deal with the large number of contacts, as in the problem under consideration.

3.2.3 Steps and boundary conditions

Abaqus simulation are composed of steps within which perform various calculations that can be connected or not between them. By default, there is the *initial step* in which it is usually going to define boundary conditions (BCs)[2], interaction properties etc., which are valid for all the operations that are going to be executed in the various successive steps. The *initial step* is followed by one or more analysis steps. Each analysis step is associated with a specific procedure that defines the type of analysis to be performed during the step.
In this specific case two steps are considered:

- **Step initial**.
  In the first step the condition of extreme fixed is defined. The "clamp" BC created for the selected edge and then propagated in the next step, consists in the condition of *encastre* which set equal to zero all the kinematic variables of the end wires surfaces.

- **Step displacement**.
  In the second step the longitudinal displacement and then cross displacement are realised, considering active geometric non-linearity. Two BCs are associated to step displacement: the "tensile" BC consists in the displacement of traction along z-axis, defined on the opposite edge to that fixed; the "displacement" BC consists of assigning a sinusoidal transverse cycle, measuring the relative restoring force to encastre.
  These two BCs are implemented with the use of so-called *Amplitudes* which are time-dependent functions that multiply the BCs or the strength to be able to reproduce the temporal trends of the shares. Referring to step displacement, two amplitudes are constructed: the first (*tensile*) amplitude consists of a ramp that goes from zero to one (at time t1 = 0.04728672 s) and then remains constant (up to the time tf = 0.2364336 s); the second (*sinusoidal*) amplitude starts with a value equal to zero from time zero to time t1 and then produces a sine wave unitary amplitude that returns to zero at time tf. The frequency of 5.28 Hz chosen is not effectively static; in section 3.3, final considerations will be explain this aspect. *Tensile* amplitude function is associated to tensile BC, which consists of a longitudinal displacement of 0.8 mm; while *sinusoidal* amplitude function is associated to the displacement BC, which consists in a zero displacement in the transverse direction X and a displacement of 10 mm in the transverse direction Y.
  In this way the initial pre-stress and the cycle of transverse displacement are achieved in a single step.

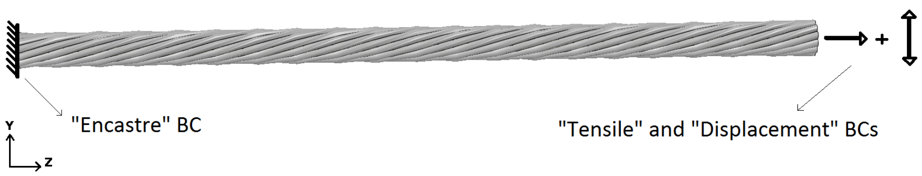

Figure 3.10: Boundary conditions

Name	Initial	displacement
ENCASTRE	Created	Propagated
TENSILE	-	Propagated
DISPLACEMENT	-	Propagated

Table 3.3: BCs step definition

[2] In the following the acronym BCs for boundary condition is used

3.2.4 Output definition

Abaqus provides some amount of default post-processing in base models while particular outputs must be selected, for example results related to contact. To this purpose it needs to define *Set* and *Surface*. The first set created is a *node type* set and refer to central node of the mesh at the edge subjected to both longitudinal and transversal displacement. Then, three surfaces are defined: a first collecting embedded surfaces at one end (*bottom-surf*), a second grouping of the areas subject to displacement BCs to the other end (*up-surf*), and finally a third which contains all the side surfaces of the various wires (*contact-surf*). In *Field output request* section, for the whole model are required:

- *Displacement, Stresses, Forces, and Strains* (default output);
- *Contact stresses*; these allow to plot the tensions of contact between the wires.

In *History output request* section,5 output cases are defined:

- Within the *Domain* section of the editor, *General contact surface* is selected and associated to *contact-surf* surface, requiring as outputs among the quantities of the menu *Contact*, the contact surface and the total force of contact;
- Within the *Domain* section of the editor, *Set* tipology is selected and associated to *central node* set, requiring the output *Displacement*, in order to obtain as output the assigned displacement history;
- Within the *Domain* section of the editor, *Integrated output section* is selected and associated to *bottom-surf* surface, requiring the amount Forces/Reaction. In this way, constraining reaction is evaluated for integration of the stresses in the section;
- The previous request is repeated for the surface *up-surf*. In this way it evaluates the same Forces/Reaction for integration of the stresses on the opposite end section;
- Within the *Domain* section of the editor, *Whole model* is selected, indicating the voice *Energy* output in order to have the energy dissipated by friction.

3.3 Considerations about Reference model

The model described in this document is very expensive from the computational point of view due to the number of domains involved as well as the complex contact geometries. The explicit time discretization is unavoidable, especially for the strong non-linearity of the mechanical problem. The displacement cycle applied at a frequency of 5.28 Hz, is due to the necessity of having acceptable computational times. In fact, lower is the frequency with which the displacement is applied, greater is the simulation time, and then the time necessary to solve the problem. In this case, the frequency of 5.28 Hz could be considered as a quasi-static action, thanks to the initial traction on the rope. This pretension significantly stiffens the strand, raising its natural frequency. For models of this type it is necessary the use of a cluster that has different processors, only in this way is possible to reduce calculation times. As will be shown in detail in chapter 5, to complete the simulation time, mass scaling approach and a particular frequency output are adopted. Nevertheless, the computational cost associated to the 3D strand model[3]) make unusable some analyis results, especially for the case of SMA material. For this purpose, two less refined mesh will be generated for the strand and original reference model discretization ($3 \cdot 10^6$ DOFs) will not be considered during steel-SMA strand response comparison.

[3]Following, "3D strand" and "3D model" will be used to refer to a model meshed by 3D solid finite elements

Starting from these considerations, a simplified model using non conventional elements is investigated in the following chapter. This represents an attempt to create a model with the following features:

- a reduced number of DOFs compared to the reference 3D model;
- ease in the model implementation (to this purpose, a matlab code will be necessary for the automatic generation of the strand model);
- able to simulate the quasi-static problem presented for the reference model.

In chapter 4 a detailed description of the simplified model presented.

Chapter 4

Simplified models

By this time in literature there are many examples of FEM applied in ropes and strands modeling. Talking about FEA of wire strands, the use of 3D continue finite elements is found on almost all the studied cases. The solid (or continuum) elements in Abaqus can be used for linear analysis and for complex non-linear analysis involving contact, plasticity, and large deformations, problems that may affect the use of ropes and cables. Furthermore, triangular and tetrahedral elements are geometrically versatile and are used in many automatic meshing algorithms. It is very convenient to mesh a complex shape such as helical geometries of strands with triangles or tetrahedra, and the second-order triangular and tetrahedral elements in Abaqus/CAE are suitable for general usage. Nevertheless, often the use of these elements implies the generation of dense mesh to obtain accurate results. If this aspect is associated to complex simulations the model efficiency could decrease, with an increase of computational costs.
In this chapter a simplified model is investigated, based on *shell* and *beam* elements. Some tests will be performed for the presented model, both on simple wires and on strand problem referring to the reference model. The simplified model does not pretend to provide an effective alternative to conventional 3D FE based models, rather create interest in unconventional models for wires and strands modeling.

4.1 MPC Beam Model

The simplified model or *MPC Beam Model*[1] consisted of a circular rod modelled by *beam* elements, used for the central axis of the rod, and a shroud of *shell* elements, constrained at each node by a multi-point kinematic constraint. The basic idea of the MPC Beam Model is to model separately the axial-bending load problem and the contact problem. The external shells provide a consistent contact surface, while the internal beam elements simulate the tensio-flexure wire behaviour.

4.1.1 Model construction and mesh discretization

In the first modeling step, two geometric parts are created in Abaqus/CAE:

- **"BEAM" part**;
- **"SHELL" part**.

To better understand the following modeling steps, a scheme of the created parts is reported in Figure 4.1.

[1]In the following the name *MPC Beam Model* will be used to identify the simplified model. The name takes inspiration from the type of kinematic constraint used in the modeling.

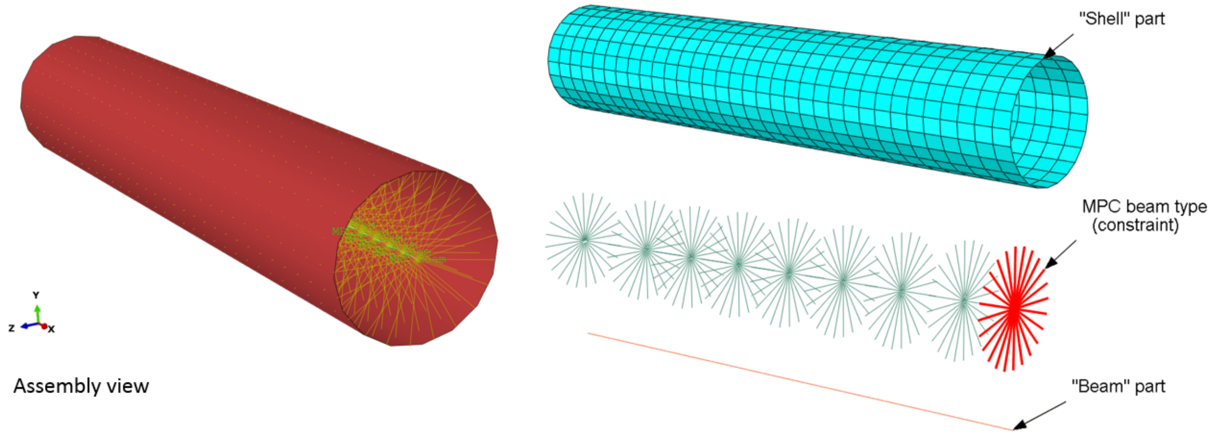

Figure 4.1: Assembly view and exploded view

- **"BEAM" part**

Within the Part module, a 3D deformable Wire (type planar) is defined. All beam elements must refer to a beam section property that defines the material associated with the element as well as the beam section profile (i.e., the element's cross-sectional geometry). Thus, after the sketching phase and the material property definition, a solid section with circular profile is assigned to the created part. Abaqus calculates the cross-section behavior of the beam by numerical integration over the cross-section when beam section profile is geometrically defined, allowing both linear and non-linear material behavior. A trapezoidal integration scheme is used for the solid beam in space: 3 integration points radially, 8 circumferentially and 1 point situated at the center of the beam (17 total, see Figure 4.2). The radius of the circular profile must be chosen in an appropriate manner, taking into account the thickness that will be assigned to the outer shell.
As suggested by the part name, a linear beam element (B31: a 2-node linear beam in space) is selected for the wire discretization. Three-dimensional beams have six degrees of freedom at each node: three translational degrees of freedom (1–3) and three rotational degrees of freedom (4–6). The linear beams (B21 and B31) are shear deformable and account for finite axial strains; therefore, they are suitable for modeling both slender and stout beams.

- **"SHELL" part**

Within the Part module, a 3D deformable Shell (type extrusion) is defined. All shell elements must refer to a shell section property that defines the thickness and material properties associated with the element.
The stiffness of the shell cross-section can be calculated either during the analysis or once at the beginning of the analysis. For the first method Abaqus uses numerical integration to calculate the behavior at selected points through the thickness of the shell. In the second approach, Abaqus models the shell's cross-section behavior directly in terms of section engineering quantities (area, moments of inertia, etc.), so there is no need for Abaqus to integrate any quantities over the element cross-section. Although this option is less expensive computationally, it is recommended when the response of the shell is linear elastic, therefore not very effective in those problems where a non-linear response is expected. Thus, for the model under consideration is preferred the first approach. For stiffness calculation during analysis, Simpson's rule and Gauss quadrature are provided to calculate the cross-sectional behavior of a shell. Gauss quadrature provides greater accuracy than Simpson's rule when the same number of section points are used. Nevertheless, in Gauss quadrature Abaqus does not foresee section points on the shell surfaces; therefore, Gauss quadrature should be used only in cases where results on the shell surfaces are not required. In this work, the shell part has been designed in order to simulate the contact behavior between

wires and to obtain results output on the shell surfaces. Thus, Simpson'rule is chosen as thickness integration method, with 5 thickness integration points shown in Figure 4.2.

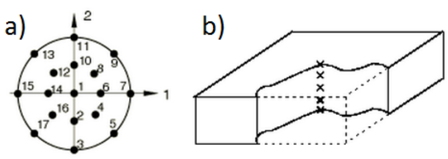

Figure 4.2: Integration schemes: a) default integration points for beam in space; b) section points through the shell thickness

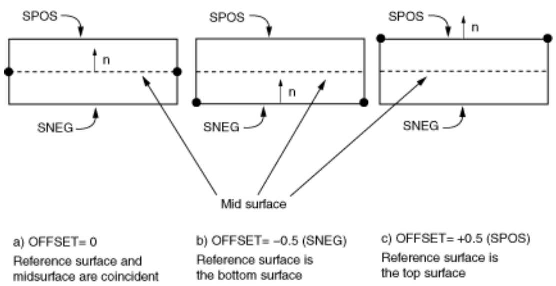

Figure 4.3: Schematic of shell offset

After the sketching phase and the material property definition, a homogeneous shell section with is correlated thickness is assigned to the created part. Editing section assignment is possible to define the reference surface of the shell. The reference surface is defined by the shell element's nodes and normal definitions. The degrees of freedom for the shell are associated with the reference surface. All kinematic quantities, including the element's area, are calculated there. When modeling with shell elements, the reference surface is typically coincident with the shell's midsurface. However, many situations arise in which it is more convenient to define the reference surface as offset from the shell's midsurface. As example, shell offsets can be useful to define a more precise surface geometry for contact problems where shell thickness is important. In order to define the most appropriate reference surface, two cases are considered for the studied model:

- ***Midsurface model*** where the default offset 0 is set and the middle surface of the shell is the reference surface (see Figure 4.3);
- ***Topsurface model*** where the offset is set on "topsurface" option (by specifying when the value offset is equal to 0.5) and the reference surface consists on the top surface of the shell (see Figure 4.3).

According to the considered model, some clarifications about Shell part thickness and radius are necessary. Consider a wire having a radius $r = r_b + s$, where r_b is the radius of the circular profile associated to Beam part and s is the thickness of the shell section. In sketch module, if MidSurfce model is considered, the shell radius r_s to draw will be given by $r_s = r - s/2$; while for the TopSurface model it will be given by $r_s = r - s$. This simple rule is adopted to represent the real cross section of the wire object, without add or subtract area to the real section. Furthermore this avoid inconsistencies between those indicated during Sketch phase and as defined in Property module. Figure 4.4 shows the cross section of the wire model both for Midsurface model and Topsurface model and their geometrical section properties are reported.
To meshing the Shell part, a linear shell element (S4R: a 4-node doubly curved thin or thick shell, reduced integration, hourglass control, finite membrane strains) is selected. In Abaqus/Explicit conventional shell elements are general-purpose; finite membrane strain and small membrane strain formulations are available. The S4R shell elements have six degrees of freedom at each node (three translations and three rotations). These elements allow transverse shear deformation. They use thick shell theory as the shell thickness increases and become discrete Kirchhoff thin shell elements as the thickness decreases; the transverse shear deformation becomes very small as the shell thickness decreases.

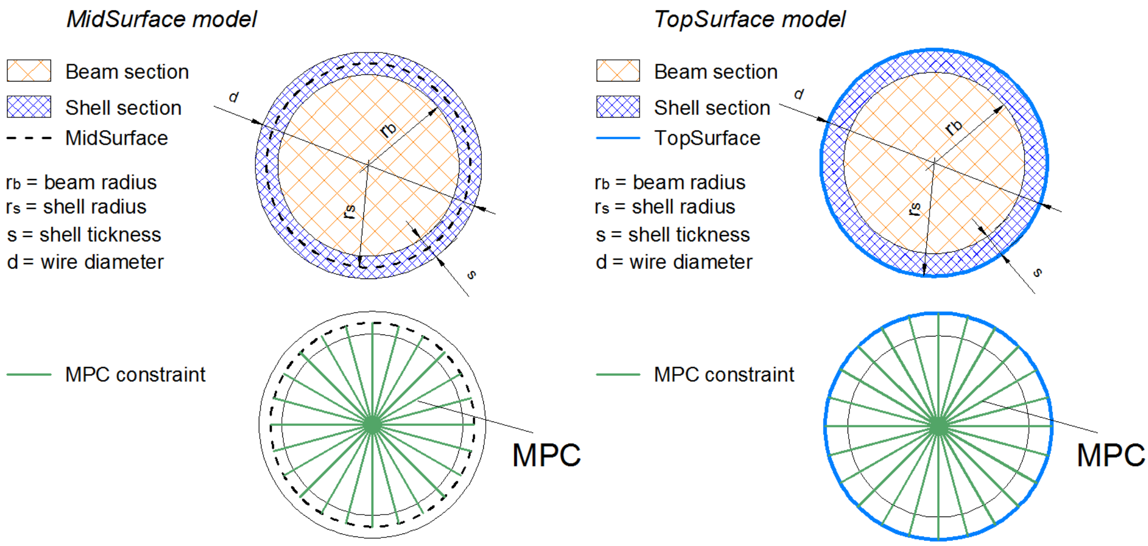

Figure 4.4: Geometrical cross section properties of Midsurface and Topsurface models

In the Assembly module instances related to the parts are created. Their relative position is defined in a global coordinate system, thus creating the assembly. Part instances are positioned by applying simple translations and rotations, in order to have the cylindrical axis of the Shell part coincident with the longitudinal axis of Beam part profile.
To create a kinematic connectivity between Beam and Shell parts a particular kinematic constraint is addressed: the Multi-points constraint (MPC). An MPC allows to constrain the motion of the slave nodes of a region to the motion of a single point. The Abaqus user can create an MPC by specifying a control point and a region composed of nodes, edges, and surfaces. For the simplified model, the control points are the Beam part mesh points; the slave nodes are the Shell part mesh nodes belonging to the circumference lying in the plane orthogonal to the wire axis, passing through the control point (see Figure 4.6 and Figure 4.8). Note that MPCs for the Midsurface model are "anchored" on the middle surface nodes, while for the TopSurface case these join the reference nodes directly with the top section surface (see Figure 4.4).
According to these definitions, the creation of MPCs along the entire model, is correlated to mesh discretization of either parts. For example (Example 1), if the Beam part is discretized by 4 beam elements (5 mesh nodes) the Shell part will be meshed in order to obtain 5 sets of nodes corresponded to the 5 beam elements nodes. In this way it is possible to create 5 distincts MPCs. The Shell part discretization along the x-axis is strictly connected to the number of nodes that subdivided the Beam part, while the circular edge could be meshed without too many restrictions. For greater clarity in Figure 4.5 the scheme described above is illustred.

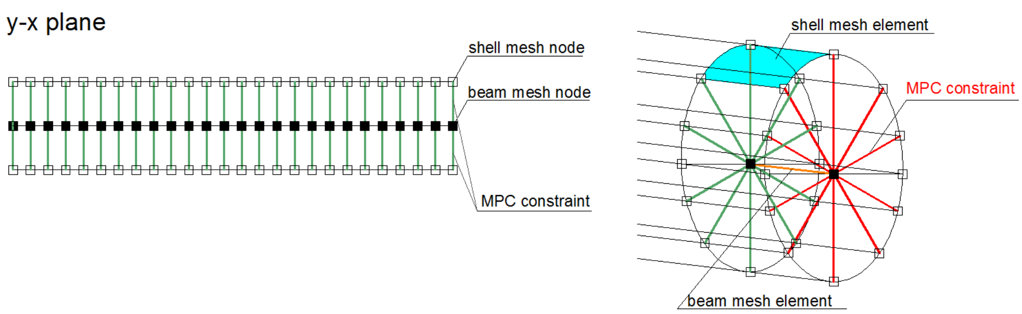

Figure 4.5: Parts discretization for construction of MPC

MPCs are created in the Interaction module: the voice MPC constraint is selected from the type list, the control point and the slave nodes for each MPC must be specified. Editing MPC it is possible to use existing sets for the definition of the control point and the slave nodes. This avoid confusion during selection of nodes when these are directly selected from the element assembly view. Thus, referring to Example 1, 5 distinct sets are created respectively from Beam part and Shell part. In Figure 4.6 the configuration of created sets is reported for the Example 1.

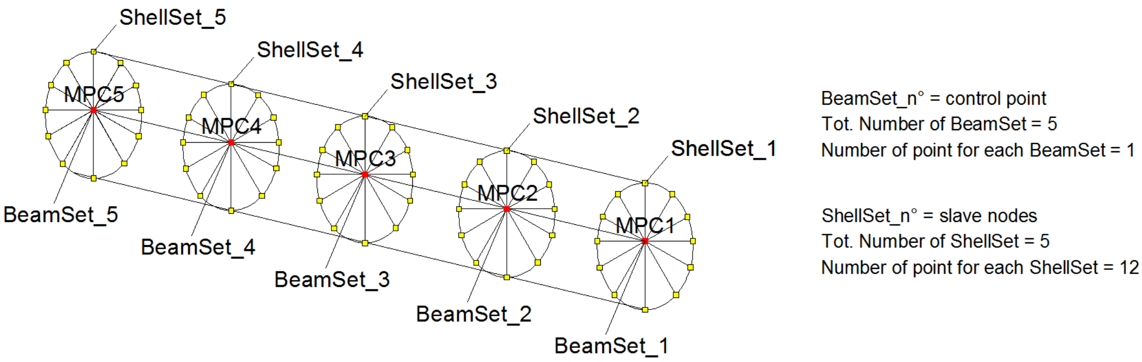

Figure 4.6: Example 1: sets definition for control points and slave nodes

Once defined MPC "geometry", from the editor appears the list of MPC type available for this kinematic constraint.
In the following, the various types of MPC are described and tested through a simple problem, which results lead to the MPC type chosen for the simplified model.

MPC constraints tests

The available typologies of MPC constraints are:

- ***Beam*** to define a rigid beam connection to constrain the displacement and rotation of each slave node to the displacement and rotation of the control point, corresponding to the presence of a rigid beam between the two nodes;
- ***Tie*** to make all active degrees of freedom equal at each slave node and the control point;
- ***Link*** to define a pinned rigid link between each slave node and the control point;
- ***Pin*** to define a pinned joint between each slave node and the control point;
- ***Select User-defined*** to define a multi-point constraint in user subroutine MPC for (Abaqus/Standard).

In order to understand the different types of constraint and choose the most appropriate for the simplified model, a simple test is performed for each type of MPC. The data in the following table are related to the simple problem of a "cantilever" wire, modelled according to the scheme presented in section 4.1. The wire is subjected to different load cases (concentrated forces and moments) applied to an extreme of the central beam element (Point 1). Displacements and rotations of the nodes indicated in Figure 4.7, are reported for each load case.
Observing the data given in Table 4.1, neither *link type* nor *pin type* are appropriate for the purpose of the objective pursued. In fact, by applying a tensile along the x axis, *MPC link* makes zero displacement U1 at points 2 and 3. This involves an extension of the central element (beam) along the x axis, while the surrounding shell is not in tension, remaining in the initial position. Applying a moment about the x axis, in *MPC pin* the displacement of the points 2 and 3 along z is zero, contrary to what is expected for a section subjected to a torque action. The same result is observed for the *MPC tie*. Data related to *MPC beam* are the most realistic, therefore this type of constraint is chosen for the simplified model.

MPC	F type	nodo	U1 (mm)	U2 (mm)	U3 (mm)	UR1	UR2	UR3
beam	Fx pos	1	3,14E-01	≈ 0	≈ 0	≈ 0	≈ 0	≈ 0
beam	Fx pos	2	3,14E-01	≈ 0	≈ 0	≈ 0	≈ 0	≈ 0
beam	Fx pos	3	3,14E-01	≈ 0	≈ 0	≈ 0	≈ 0	≈ 0
beam	Fy neg	1	0	-1,50E-03	0	≈ 0	≈ 0	-1,19E-03
beam	Fy neg	2	-5,92E-04	-1,50E-03	0	≈ 0	≈ 0	-1,19E-03
beam	Fy neg	3	5,92E-04	-1,50E-03	0	≈ 0	≈ 0	-1,19E-03
beam	Fz neg	1	0	0	-1,50E-03	0	1,20E-03	≈ 0
beam	Fz neg	2	-1,50E-04	≈ 0	-1,50E-03	0	1,20E-03	≈ 0
beam	Fz neg	3	0	≈ 0	-1,50E-03	0	1,20E-03	≈ 0
beam	Mx	1	-2,00E-07	0	0	4,00E-03	≈ 0	≈ 0
beam	Mx	2	-2,00E-07	4,50E-04	-2,00E-03	4,00E-03	≈ 0	≈ 0
beam	Mx	3	-2,00E-07	0	2,00E-03	4,00E-03	≈ 0	≈ 0
beam	My	1	0	0	-1,20E-03	≈ 0	2,00E-03	≈ 0
beam	My	2	-2,00E-04	≈ 0	-1,20E-03	≈ 0	2,00E-03	≈ 0
beam	My	3	0	≈ 0	-1,20E-03	≈ 0	2,00E-03	≈ 0
beam	Mz	1	0	1,20E-03	≈ 0	≈ 0	≈ 0	1,60E-03
beam	Mz	2	7,50E-04	1,20E-03	≈ 0	≈ 0	≈ 0	1,60E-03
beam	Mz	3	7,50E-04	1,20E-03	≈ 0	≈ 0	≈ 0	1,60E-03
tie	Fx pos	1	3,14E-01	≈ 0	≈ 0	≈ 0	≈ 0	≈ 0
tie	Fx pos	2	3,14E-01	≈ 0	≈ 0	≈ 0	≈ 0	≈ 0
tie	Fx pos	3	3,14E-01	≈ 0	≈ 0	≈ 0	≈ 0	≈ 0
tie	Fy neg	1	5,50E-07	-1,50E-03	≈ 0	≈ 0	≈ 0	-1,19E-03
tie	Fy neg	2	5,50E-07	-1,50E-03	≈ 0	≈ 0	≈ 0	-1,19E-03
tie	Fy neg	3	5,50E-07	-1,50E-03	≈ 0	≈ 0	≈ 0	-1,19E-03
tie	Fz neg	1	6,00E.07	≈ 0	-1,50E-03	≈ 0	1,20E-03	≈ 0
tie	Fz neg	2	6,00E.07	≈ 0	-1,50E-03	≈ 0	1,20E-03	≈ 0
tie	Fz neg	3	6,00E.07	≈ 0	-1,50E-03	≈ 0	1,20E-03	≈ 0
tie	Mx	1	-2,00E-07	≈ 0	≈ 0	4,00E-03	≈ 0	≈ 0
tie	Mx	2	-2,00E-07	≈ 0	≈ 0	4,00E-03	≈ 0	≈ 0
tie	Mx	3	-2,00E-07	≈ 0	≈ 0	4,00E-03	≈ 0	≈ 0
tie	My	1	0,8E-06	0	-1,20E-03	≈ 0	1,75E-03	≈ 0
tie	My	2	0,8E-06	≈ 0	-1,20E-03	≈ 0	1,75E-03	≈ 0
tie	My	3	0,8E-06	≈ 0	-1,20E-03	≈ 0	1,75E-03	≈ 0
tie	Mz	1	0,8E-06	1,20E-03	≈ 0	≈ 0	≈ 0	1,75E-03
tie	Mz	2	0,8E-06	1,20E-03	≈ 0	≈ 0	≈ 0	1,75E-03
tie	Mz	3	0,8E-06	1,20E-03	≈ 0	≈ 0	≈ 0	1,75E-03
link	Fx pos	1	3,14E-01	≈ 0	≈ 0	≈ 0	≈ 0	≈ 0
link	Fx pos	2	0	≈ 0	≈ 0	≈ 0	≈ 0	≈ 0
link	Fx pos	3	0	≈ 0	≈ 0	≈ 0	≈ 0	≈ 0
pin	Fx pos	1	3,14E-01	≈ 0	≈ 0	0	≈ 0	≈ 0
pin	Fx pos	2	3,14E-01	≈ 0	≈ 0	≈ 0	4,50E-07	2,00E-06
pin	Fx pos	3	3,14E-01	≈ 0	≈ 0	≈ 0	≈ 0	-2,00E-06
pin	Mx	1	-2,00E-07	≈ 0	≈ 0	4,00E-03	≈ 0	≈ 0
pin	Mx	2	-2,00E-07	≈ 0	≈ 0	0	≈ 0	≈ 0
pin	Mx	3	-2,00E-07	≈ 0	≈ 0	0	≈ 0	≈ 0

Table 4.1: Displacements and rotations at nodes A,B,C related to different load cases

Using the MPC constraint the pinch effect of the section is neglected. This is related to the rigid beam (see Figure 4.8) interposed between the master node and the slave node. This element axially non-deformable does not allow the outer shell section to shrink, as example when a traction is applied to the wire. Nevertheless, considering the load cases analysed for the simplified models tests and the purpose of the work, this approximation can be considered acceptable. Kinematic constraints, as MPC, can be defined in Abaqus/Explicit in any order without regard to constraint dependencies. Thus, nodes involved in a combination of multi-point constraints, rigid body constraints and constraints due to boundary conditions will simultaneously satisfy these constraints as long as they are not conflicting. This aspect will be very important during test phase, where kinematic constraint associated to MPC model and constraints related to problem BCs are simultaneously considered.

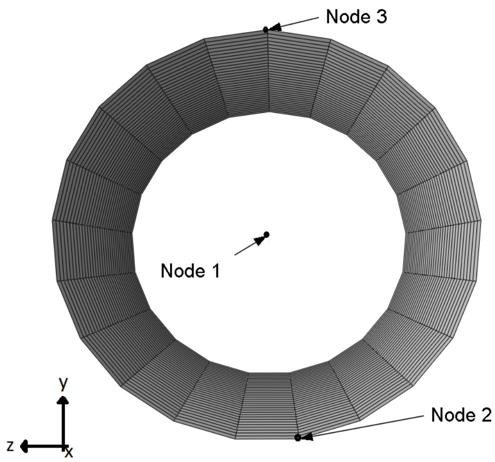

Figure 4.7: Considered nodes for the MPC test

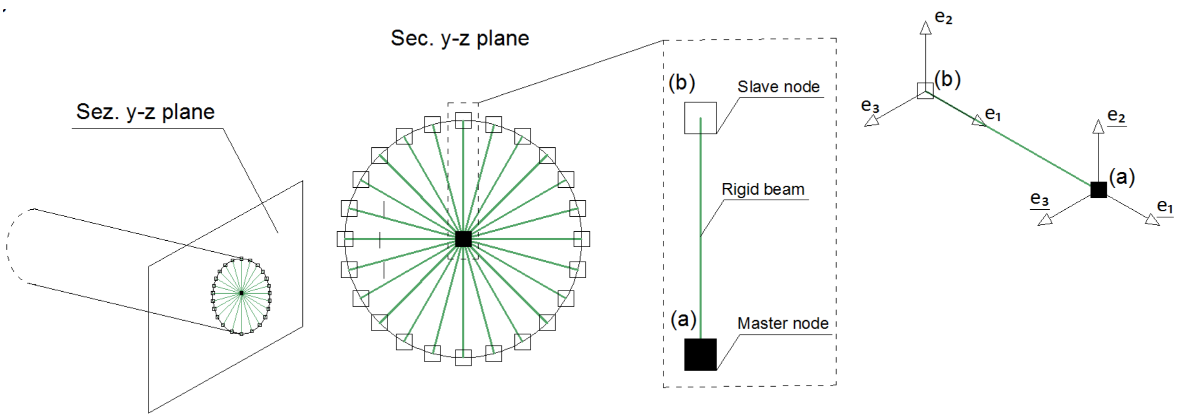

Figure 4.8: Control nodes and slave nodes in MPC

4.2 Tests on MPC Beam Model

Some simple problems are analysed for MPC Beam Model. This will be compared with an equivalent 3D finite element model[2]. Discussion and result analysis are given for the following numerical tests:

- *Single_wire tests*: a wire is subjected to different load cases in order to emphasize tensile, bending and contact behavior of MPC Beam model;
- *Double_wire test*: two superimposed wires are bent in order to emphasize contact and bending behavior of MPC Beam model when wires come into contact with each other.

Within the numerical analysis, factors that could influence MPC Beam model's behavior and outputs are taken into account:

- Shell thickness;
- Shell reference surface (MidSurface model-TopSurface model);
- Mesh discretization both for 3D model and MPC Beam model;
- Applications of BCs for the MPC Beam model.

All the considered cases and the assumptions made are described in detail in the following paragraphs.

4.2.1 Single_wire tests

Consider as real reference object a wire having the features reported in Figure 4.9:

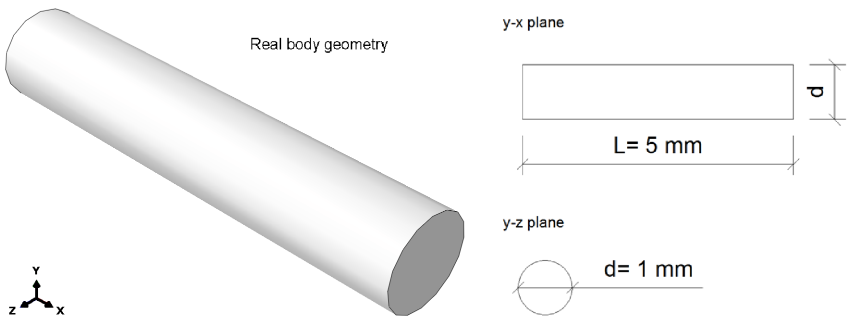

Figure 4.9: Real reference wire

Three problems are studied for the object in exam:

1. PROBLEM 1: wire leaning against a rigid surface, with a fixed-end and subjected to traction on the other extreme;
2. PROBLEM 2: "cantilever" wire, embedded to an extreme and subjected to bent on the other one;
3. PROBLEM 3: wire suitably constrained, inflected on both ends.

A logical scheme of the performed analysis is reported for each problem, showing the variable factors considered. All analysis are executed using the Abaqus/Explicit solver.

[2]In the following the name 3d Model will be used to indicate a model based on 3D solid finite elements

PROBLEM 1: Traction

Influence factor taken into account:

– **Variability of mesh discretization for 3D model**.

In the first step of problem 1, three mesh are tested for 3D model. The choice of a suitable mesh is very important to obtain realistic results and to simulate the correct wire behavior. In this particular problem, the contact phenomenon is evaluated through the interaction of the wire with a rigid surface. There are a number of issues that need to consider when modeling contact problems in Abaqus/Explicit rigid surfaces are involved. The rigid surface is always the master surface in a contact interaction. The deformable mesh (in this case the wire mesh) must be refined enough to interact with any feature on the rigid surface, preventing the rigid surface from penetrating the slave surface. As consequence, with a sufficiently refined mesh on the deformable surface, the emergence of strange errors in the output result is avoided. Thus, three combinations of mesh (Mesh1, Mesh2 and Mesh3) for the rigid surface and the wire 3D will be created, then results obtained will be compared to define the elements' dimension. Parts mesh definition for the simplified model will be based on Mesh 2 element dimension. The second aspect highlighted in problem 1 is related to the choice of the MPC beam type for the simplified model. The punch effect, neglected in MPC beam model, is observed for 3D model after the application of tension load. The magnitude of this error will be evaluated from the comparison of displacement output. In Figure 4.10 a flowchart of the analysis performed for problem 1 is provided.

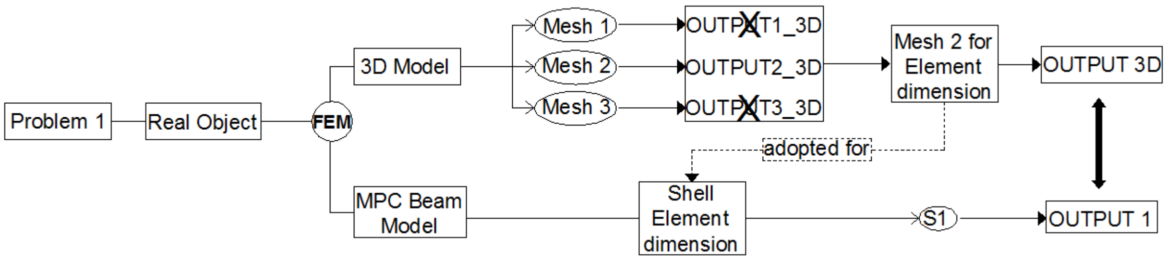

Figure 4.10: Analysis scheme for Problem 1

- **3D model**: Traction

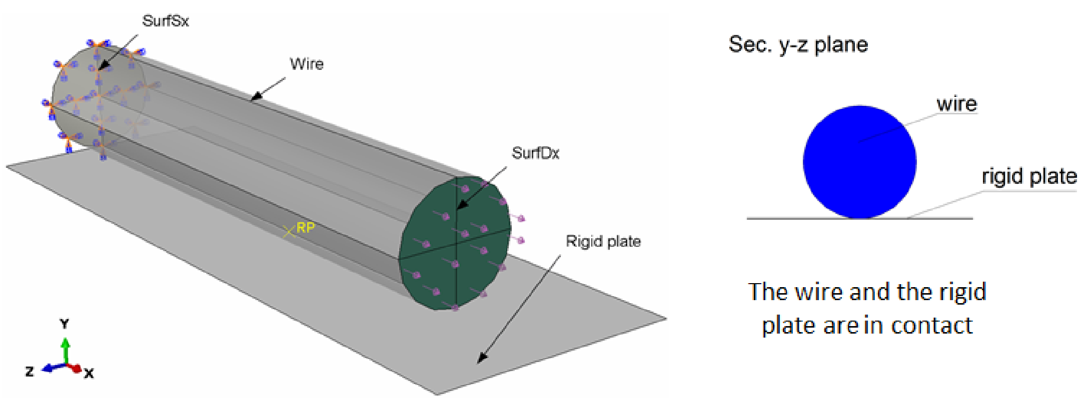

Figure 4.11: Problem 1 definition for 3D model

For 3D model case a rigid surface on which is supported a wire of length 5 mm is defined . The wire is fully-fixed to an extreme and on the opposite one, a distributed traction is applied on the cross section. The wire and the rigid plate are in contact. Linear, isotropic and elastic steel material is chosen for the wire part. For structural discretization C3D8R element is used for the solid wire, while four-node three dimensional rigid element (R3D4) is used for the rigid surface. The *Genaral contact (Explicit)* type of interaction is created for the model, associating to it *Tangential Behavior* property and specifying *Penalty* option as *Friction Formulation*. Tables below resume geometric problem characterisation and specifications related to material, mesh, BCs localization, load/step application and magnitude. Features indicated in tables are adopted throughout *Single_wire tests* for 3D wire model, with the exception of those related to the specific problem in exam.

Part	**Part type**	**Section**	**Material**	**Element type**
BeamSolid	Wire	r = 0.5 mm	Steel	C3D8R
RigidPlate	Shell	-	-	R3D4

Table 4.2: Problem 1, 3D model parts description

Steel material	
Young modulus $E[N/mm^2]$	210000
Poisson's ratio ν	0.3
Density $\rho[Kg/mm^3]$	$7.86 \cdot 10^{-6}$

Table 4.3: Problem 1, 3D model material properties

Wire geometry		**Rigid plate geometry**	
L [mm]	*r [mm]*	L*min [mm]*	*Lmax [mm]*
5	0.5	2	6

Table 4.4: Problem 1, 3D model geometric properties

Step	**Δt step [s]**	**Δt increment [s]**
Initial	-	-
Load	0.1	3.2E-07

Table 4.5: Problem1, 3D model step definition

BCs	**Type**	**Set**	**Initial step**	**Load step**
rpBC	Encastre	RP	created	propagated
BC1	Encastre	SurfSx	created	propagated

Table 4.6: Problem 1, 3D model boundary conditions

Load	**Type**	**Set**	**Value**	**Axis**	**Step**
Traction	Pressure	SurfDx	636.62 N/mm^2	x	Load

Table 4.7: Problem 1, 3D model load definition

Three different meshed models are generated, varying mesh discretization for *RigidPlate* part and *BeamSolid* part. These different mesh are reported in Table 4.8. Figure 4.12 shows 3D model discretizations and considered points (A,B,C) in output evaluation. Moving from Mesh1 to Mesh3 the mesh level accuracy increases for the rigid plate. Instead, from Mesh2 to Mesh3 the number of elements of BeamSolid part decreases, in order to try different combinations. Below, U2 displacement (Y axis) for nodes A and B is reported respectively for the three mesh cases. As result of a uniform traction it is expected a negative U2 in A and a positive one (having the same modulus) in B. Displacements related to the first mesh are incorrect and do not show the expected linear trend. Both Mesh2 and Mesh3 results are closer to the foreseen behavior, with little oscillations for the latter. Thus, Mesh2 is considered the most appropriate discretization for 3D model. The characteristic element dimensions of Mesh2 are 0.098mm x 0.100 mm for the BeamSolid elements, while they are 0.08 mm x 0.08 mm for RigidPlate elements.

	Mesh1		**Mesh2**		**Mesh3**	
Part	n° elements	n° nodes	n° elements	n° nodes	n° elements	n° nodes
BeamSolid	1452	1870	4800	5736	3192	3913
RigidPlate	1200	1281	1875	1976	4800	4961

Table 4.8: Problem 1, 3D model mesh discretizations

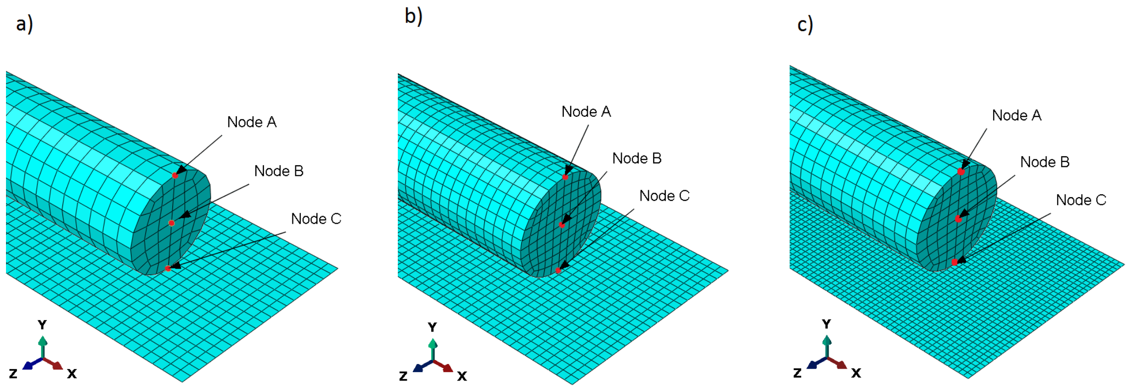

Figure 4.12: Problem 1, 3D model discretization: a) Mesh1; b) Mesh2; c) Mesh3

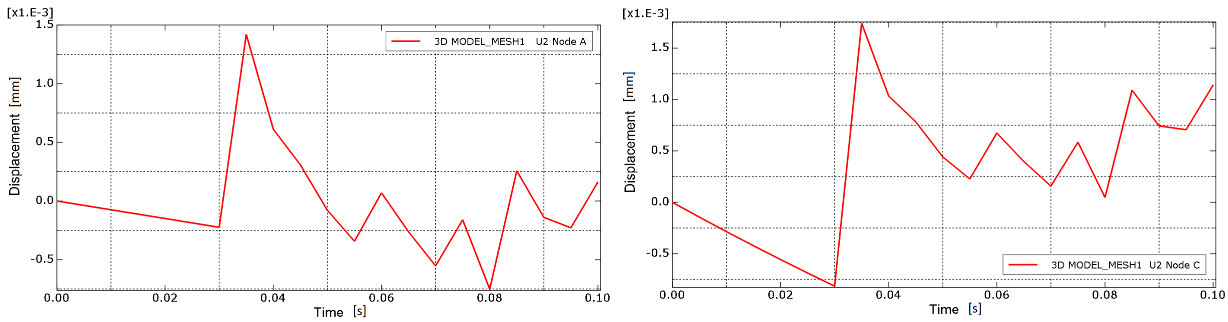

Figure 4.13: Problem 1, 3D model Mesh1: U2 displacement in node A and C

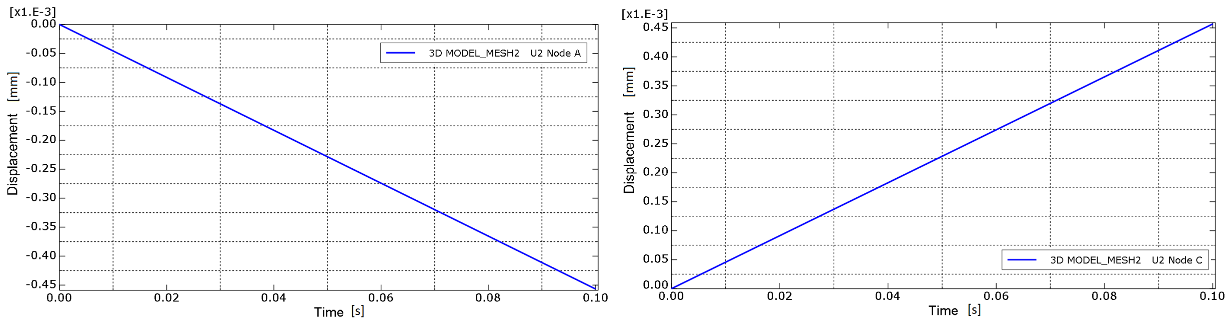

Figure 4.14: Problem 1, 3D model Mesh2: U2 displacement in node A and C

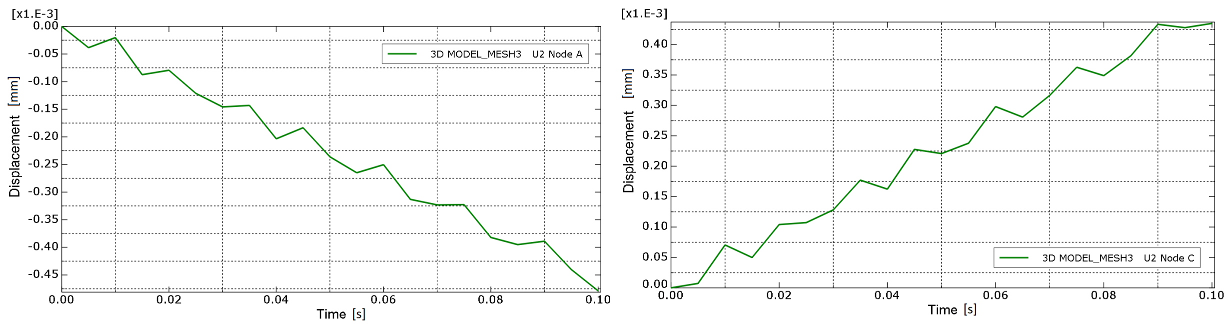

Figure 4.15: Problem 1, 3D model Mesh3: U2 displacement in node A and C

- **MPC beam model**: Traction

For MPC beam model case a rigid surface on which is supported a wire of length 5 mm is defined. The wire is fully-fixed node B' of the Beam part (see Figure 4.16) and a concentrated traction force is applied in node B. The wire and the rigid plate are in contact. In problem 1 **MidSurface** is chosen as the shell reference surface of the model, this can be seen by looking Figure 4.16.

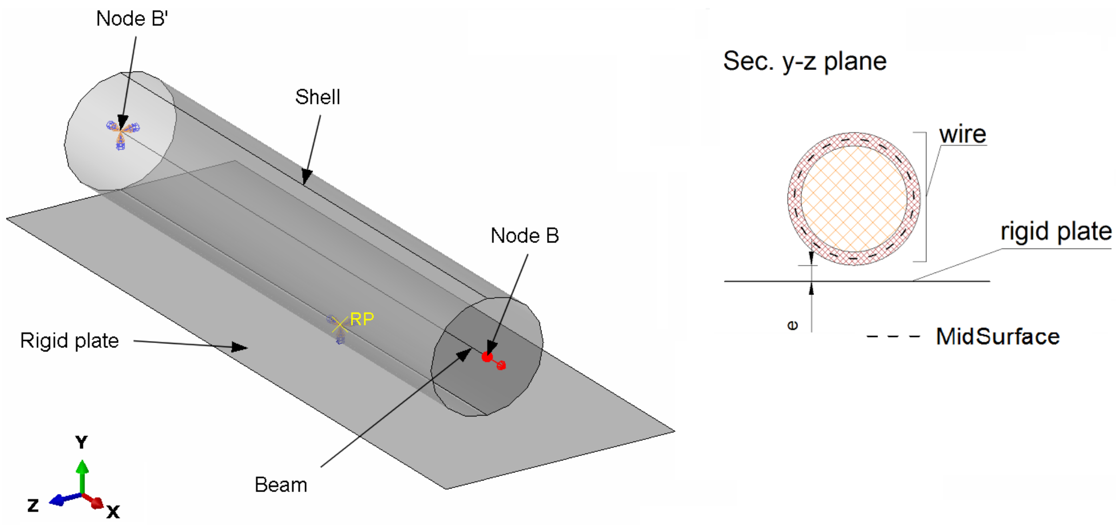

Figure 4.16: Problem 1 definition for MPC Beam model

Linear, isotropic and elastic steel material is chosen for both the wire parts (the Beam part and the Shell part). For structural discretization, B31 element is used for the Beam part, S4R element for the Shell part, while R3D4 is used for the rigid surface. MPC Beam model mesh size has been defined on the basis of Mesh2, chosen for the 3D model. After a series of verification tests, the dimensions adopted for Shell part elements are 0.096 mm x 0.108 mm (as consequence, given the constraint related to MPC connectivity, Beam part elements dimension is 0.108 mm); RigidPlate part maintains the same number of elements asociated to 3D model. The meshed model is shows in Figure 4.17. The *General contact (Explicit)* type of interaction is created for the model, associating to it *Tangential Behavior* property and specifying *Penalty* option as *Friction Formulation*. Tables below resume geometric problem characterisation and specifications related to material, mesh, BCs localization, load/step application and magnitude. Features indicated in tables are adopted throughout *Single_wire tests* for MPC Beam model, with the exception of those related to the specific problem in exam.

Part	**Part type**	**Section**	**Material**	**Element type**	n° elements	n° nodes
Beam	Wire	r_b = 0.48 mm	Steel	B31	46	47
Shell	Shell	r = 0.02 mm	Steel	S4R	1472	1504
RigidPlate	Shell	-	-	R3D4	1875	1976

Table 4.9: Problem 1, MPC Beam model parts description

Figure 4.18 shows U2 displacement at node A for MPC Beam model (U2 at node C is not reported because is equal to displacement of node A). Displacements magnitude is almost equal to zero (E-18) in either points, while for the 3D model the U2 displacement has a modulus equal to $0.45 \cdot 10^{-3}$. This result confirms the limitation associated to the simplified model, with the punch effect totally neglected. Nevertheless, non-zero values are obtained from a specific problem, created to underline this phenomenon. Generally in real applications wire contraction plays a little role, therefore for the purpose of work this aspect could be considered acceptable.

Steel material	
Young modulus $E[N/mm^2]$	210000
Poisson's ratio ν	0.3
Density $\rho[Kg/mm^3]$	$7.86 \cdot 10^{-6}$

Table 4.10: Problem 1, MPC Beam model material properties

Wire geometry		Rigid plate geometry	
L [mm]	*r [mm]*	L*min [mm]*	L*max [mm]*
5	0.5	2	6

Table 4.11: Problem 1, MPC Beam model geometric properties

Step	Δt step [s]	Δt increment [s]
Initial	-	-
Load	0.1	5.3E-07

Table 4.12: Problem 1, MPC Beam model step definition

BCs	Type	Set	Initial step	Load step
rpBC	Encastre	RP	created	propagated
BC1	Encastre	node B'	created	propagated

Table 4.13: Problem 1, MPC Beam model boundary conditions

Load	Type	Set	Value	Axis	Step
Traction	Concentrated force	node B	500 N	x	Load

Table 4.14: Problem 1, MPC Beam model load definition

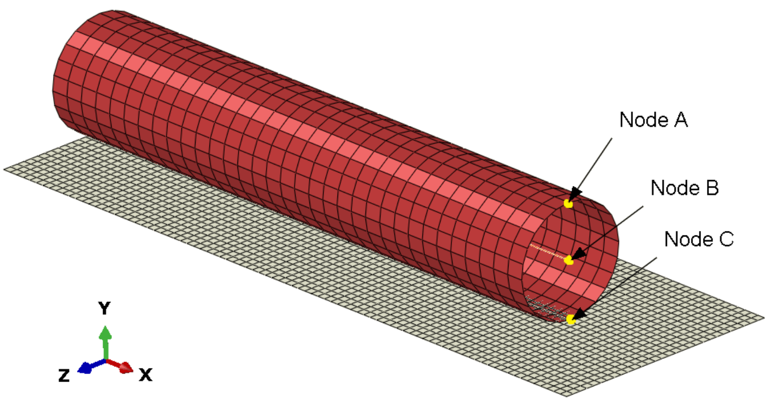

Figure 4.17: Problem 1, MPC Beam model discretization

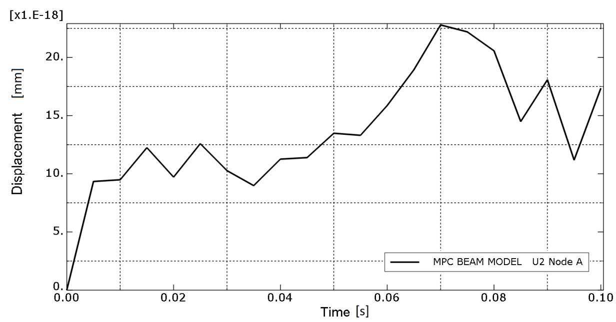

Figure 4.18: Problem 1, MPC Beam model: U2 displacement in nodes A

PROBLEM 2: Bending

Influence factor taken into account:

- **Applications of BCs for the MPC Beam model**;
- **Shell thickness**.

Through problem 2 the behavior of an embedded wire subjected to bending moment is simulated. In this problem three different shell thickness are tested for MPC Beam model. For BCs definition two different approaches are used: in the first approach BCs are applied on Beam part end nodes (indicated with "BC1" in Figure 4.19); in the second approach, an additional reference point is the retained point for the "rigid body" nodes (indicated with "BC2" in Figure 4.19). Referring to the wire end section, this rigid region is composed by the Beam part node and the Shell part nodes. From the first shell-thickness test, comparing two methods for BCs definition, the obtained output result identical. Thus, in subsequent tests the comparison between MPC Beam model and 3D model is carried out only varying shell thickness. In this problem contact wire behavior is not addressed.

In Figure 4.19 a flowchart of the analysis performed for problem 2 is provided

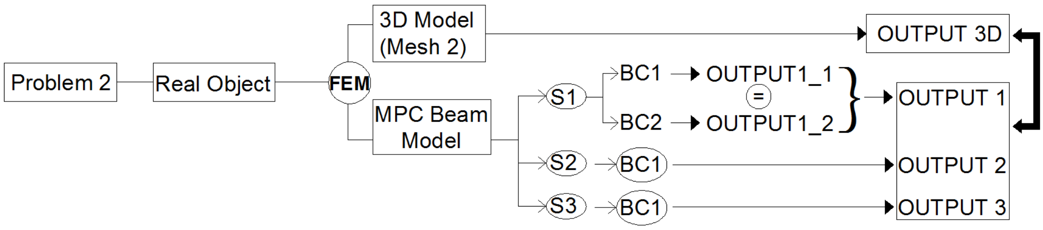

Figure 4.19: Analysis scheme for Problem 2

- **3D model**: Bending

For 3D model case a "cantilever" wire is defined. The wire is embedded to an extreme and, on the opposite one, subjected to a bending moment acting about the z-axis. Both encastre condition and bending moment are applied on reference points (see Figure 4.20). These are the retained points for the two rigid bodies composed by nodes of solid end surfaces (SurfDx and SurfSx).

Figure 4.20: Problem 2 definition for 3D model

BCs	Type	Set	Initial step	Load step
BC1	Encastre	RP1	created	propagated

Table 4.15: Problem 2, 3D model boundary conditions

Tables above resume problem features related to BCs localization, load/step application and magnitude. The duration of the step *load* remains equal to 0.1 s, only changing the Δt stable. The

Load	Type	Set	Value	Axis	Step
Mz	Moment	RP2	-15 Nmm	z	Load

Table 4.16: Problem 2, 3D model load definition

wire geometry, material and mesh specifications are the same reported in Tables 4.2-4.4 (note that in this case the problem only provides for the Beam Solid part, not involving the rigid surface). Mesh2 is adopted for 3D model (see Table 4.8).

- **MPC beam model**: Bending

For MPC beam model a "cantilever" wire is defined. The wire is embedded to an extreme and, on the opposite one, subjected to a bending moment acting about the z-axis. As previously mentioned, two different methods for the definition of BCs and bending load have been tested. The first approach is to apply the constraint/force to nodes B and B'; the second one is to apply the constraint/force to retained points RP1 and RP2, acting as master nodes for the terminal section of the wire (see Figure 4.21). As the two methods give the same results, here is considered only the first approach and its correlated output. The three tested shell-thickness are specified during results comparison phase. In problem 2 **MidSurface** is chosen as the shell reference surface of the model.

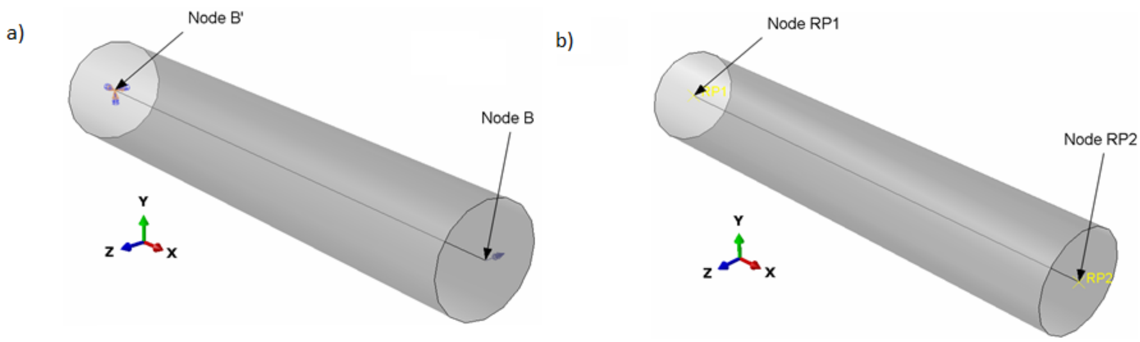

Figure 4.21: Problem 2 definition for MPC Beam model

Tables below resume problem features related to BCs localization, load/step application and magnitude. The duration of the step *load* remains equal to 0.1 s, only changing the Δt stable. Geometry of wire, material and mesh specifications are the same reported in Tables 4.9-4.11 (note that in this case the problem only provides for the Beam part and the Shell part, not involving the rigid surface).

BCs	Type	Set	Initial step	Load step
BC1	Encastre	node B	created	propagated

Table 4.17: Problem 2, MPC Beam model boundary conditions

Load	Type	Set	Value	Axis	Step
Mz	Moment	node B'	-15 Nmm	z	Load

Table 4.18: Problem 2, MPC Beam model load definition

In order to emphasize models behaviour, in the following, results related to 3D model and MPC Beam model are directly compared. In this problem displacements and stress output are evaluated.

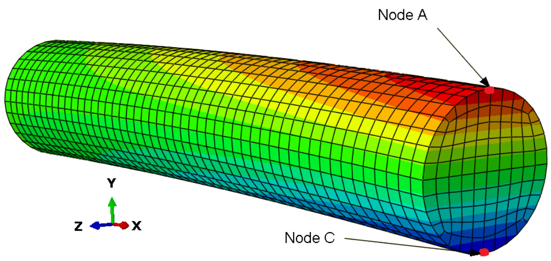

Figure 4.22: Problem 2, 3D model: U2 displacement contour plot

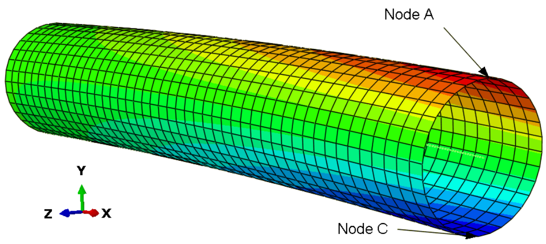

Figure 4.23: Problem 2, MPC Beam model: U2 displacement contour plot

For simplicity, only figures and diagrams correlated to MPC Beam model characterised by s_1 shell thickness are presented.
Thickness chosen for Shell part are respectively:

- $\mathbf{s_1 = 0.02}$ **mm**;
- $\mathbf{s_2 = 0.01}$ **mm**;
- $\mathbf{s_3 = 0.005}$ **mm**.

3D model and MPC Beam model show a similar contour plot for U1 displacement. This is clearly visible by the colour distribution illustrated in Figures 4.22 and 4.23. Figure 4.23 refers to MPC Beam model having s_1 thickness, but similar contour plot can be found both for s_2 and s_3. The same consideration can be made for U1 displacement and Mises stress output (see Figures 4.24-4.27). The displacement along y-axis is measured in nodes A and C, where the value is maximum, while for displacement along x-axis only the point A is considered. Correlated results will be used to estimate the percentage variation between models.

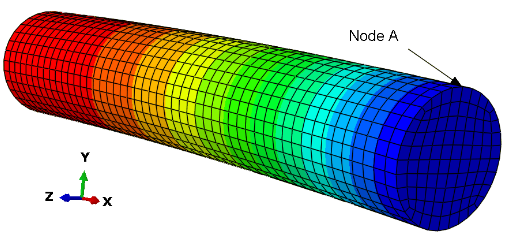

Figure 4.24: Problem 2, 3D model: U1 displacement contour plot

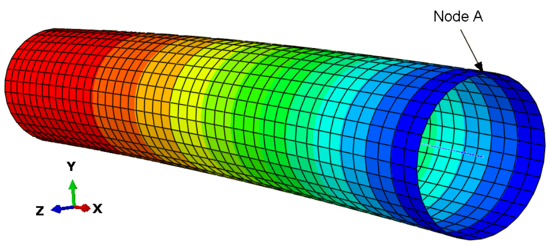

Figure 4.25: Problem 2, MPC Beam model: U1 displacement contour plot

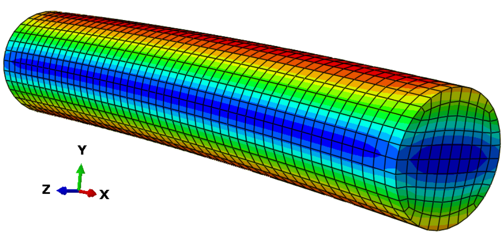

Figure 4.26: Problem 2, 3D model: Mises stress contour plot

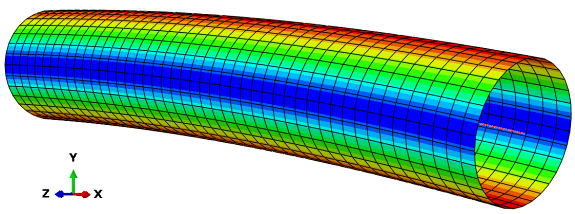

Figure 4.27: Problem 2, MPC Beam model: Mises stress contour plot

MPC Beam model	**Error%** s_1	**Error%** s_2	**Error%** s_3
U1 displacement	3.6	2.2	1.4
U2 displacement	1.7	0.2	$\cong 0$
Mises stress	5	7.7	9.1

Table 4.19: Problem 2, percentage error correlated to MPC Beam model

The percentage error correlated to the MPC Beam model use is evaluated. The percentage error gives the difference between the approximate and exact values, in this case respectively 3D solid values and MPC Beam model values. This is calculated referring to maximum values obtained for U1-U2 displacements and Mises stress. Moving from s_1 to s_3 thickness the error decreases in terms of displacement but increase for Mises stress. This fact, also noticed in subsequent tests, is probably due to the variation of beam part section radius when different thickness are associated to the shell part. As it can be observed by seeing Table 4.19, globally the lower percentage errors are associated to s_1, remaining below 5%.

PROBLEM 3: Bending + contact

Influence factors taken into account:

– **Shell reference surface (MidSurface model-TopSurface model)**;

– **Shell thickness**.

Bending and contact behavior of a wire interacting with a rigid surface is investigated in Problem 3. For MPC Beam model both **MidSurface** and **TopSurface** options are tested as shell reference surface. Both for MidSurface and TopSurface model, three different shell thickness are evaluated (in Figure 4.28 "MS" and "TS" refer respectively to MidSurface and TopSurface, while different shell thickness are indicated with "S1", "S2"and "S3").

In Figure 4.28 a flowchart of the analysis performed for problem 3 is provided.

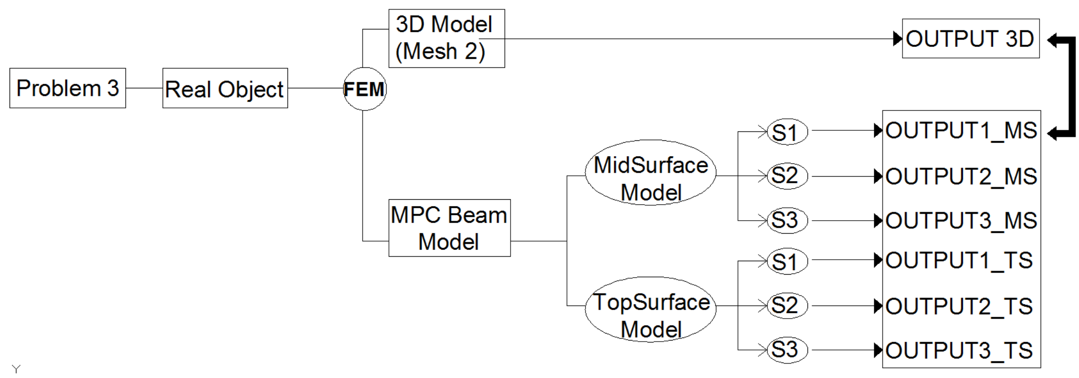

Figure 4.28: Analysis scheme for Problem 3

- **3D model**: Bending + contact

For 3D model case a rigid surface and a wire of length 5 mm are defined. Initially the wire and the rigid plate are not in contact; by applying an equal bending moment to both wire extremities, this comes into interaction with the rigid surface. In wire ends are defined two BCs (BCdx and BCsx) through which all translational degrees of freedom are constrained. Bending moments and

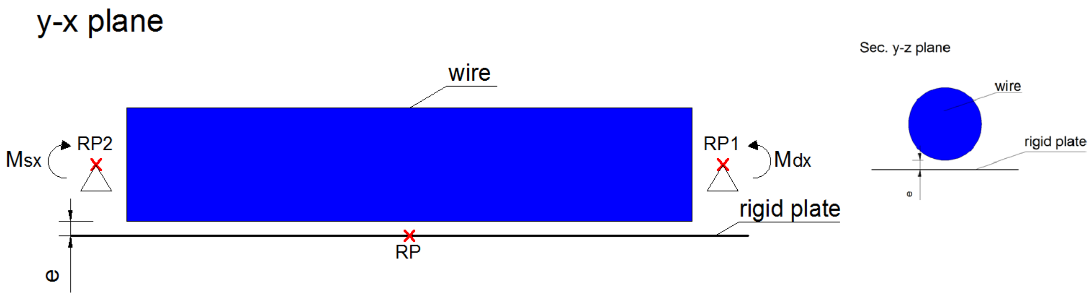

Figure 4.29: Problem 3 definition for 3D model

BCs are applied through reference points (see Figure 4.29). These are the retained points for the rigid bodies composed by nodes of solid end surfaces (SurfDx and SurfSx).
Tables below resume problem features related to BCs localization, load/step application and magnitude. The duration of the step *load* remains equal to 0.1 s, only changing the Δt stable. Wire geometry, material and mesh specifications are the same reported in Tables 4.2-4.4. Mesh2 is adopted for 3D model (see Table 4.8).

BCs	**Type**	**Set**	**Initial step**	**Load step**
rpBC	Encastre	RP	created	propagated
BCdx	U1=U2=U3=0	RP1	created	propagated
BCsx	U1=U2=U3=0	RP2	created	propagated

Table 4.20: Problem 3, 3D model boundary conditions

Load	**Type**	**Set**	**Value**	**Axis**	**Step**
Mdx	Moment	RP1	15 Nmm	z	Load
Msx	Moment	RP2	-15 Nmm	z	Load

Table 4.21: Problem 3, 3D model load definition

- **MPC beam model**: Bending + contact

For MPC Beam model case a rigid surface and a wire of length 5 mm are defined. Initially the wire and the rigid plate are not in contact; by applying an equal bending moment to both wire extremities, this comes into interaction with the rigid surface.
In wire ends are defined two BCs (BCdx and BCsx) through which all translational degrees of freedom are constrained. Bending moments and BCs are applied at nodes B and B' (see Figure 4.30). Tables below resume problem features related to BCs localization, load/step application and magnitude. The duration of the step *load* remains equal to 0.1 s, only changing the Δt stable. Geometry of wire, material and mesh specifications are the same reported in Tables 4.9-4.11.

BCs	**Type**	**Set**	**Initial step**	**Load step**
rpBC	Encastre	RP	created	propagated
BCdx	U1=U2=U3=0	RP1	created	propagated
BCsx	U1=U2=U3=0	RP2	created	propagated

Table 4.22: Problem 3, MPC Beam model boundary conditions

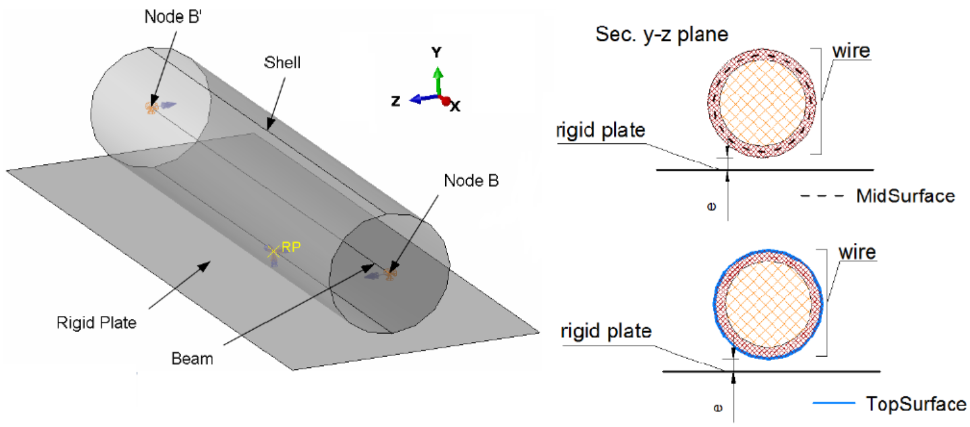

Figure 4.30: Problem 3 definition for MPC Beam model

Load	Type	Set	Value	Axis	Step
Mdx	Moment	RP1	15 Nmm	z	Load
Msx	Moment	RP2	-15 Nmm	z	Load

Table 4.23: Problem 3, MPC Beam model load definition

Tests are performed both for MidSurface and TopSurface model (in Figure 4.30 the position of either reference surfaces is indicated) and for each case the following shell thickness are tested:

- $s_1 = \mathbf{0.02}$ **mm**;
- $s_2 = \mathbf{0.01}$ **mm**;
- $s_3 = \mathbf{0.005}$ **mm**.

In order to emphasize models behaviour, in the following, results related to 3D model and MPC Beam model are directly compared. In this problem displacements, stress and contact output are evaluated. For simplicity, only figures and diagrams correlated to TopSurface MPC Beam model characterised by s_1 shell thickness are presented.
3D model and MPC Beam model show a similar contour plot for U2 displacement. This is visible by the colour distribution in Figures 4.31 and 4.32. Figure 4.32 refers to MPC Beam model having s_1 thickness, but similar contour plot can be found both for s_2 and s_3. The same consideration can be made for the others output taking into account (see Figures 4.34-4.39). The displacement along x-axis is measured in nodes A and C, where the value is maximum.

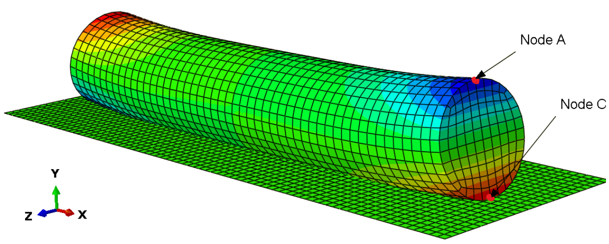

Figure 4.31: Problem 3, 3D model: U1 displacement contour plot

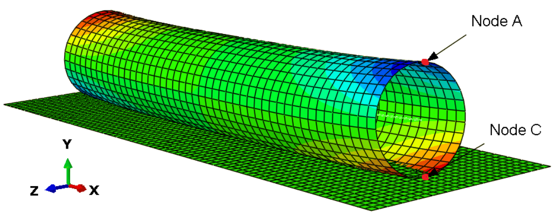

Figure 4.32: Problem 3, MPC Beam model: U1 displacement contour plot

Figure 4.33 shows the U1 displacement-time curves at node A for 3D model and MPC Beam model (U1 at node C has equal modulus but opposite sign than node A) . The two curves present the same trend and they are characterised by a change of slope occurring at $\Delta t \cong 0.025$ s. This is the simulation point in which the wire comes into contact with the rigid surface: when the contact occurs the shortening at node A is opposed by friction and its growth rate decreases linearly. In Figure 4.33 are underlined maximum values of for either models. These values will be used for the estimate of percentage error occurring between two models.

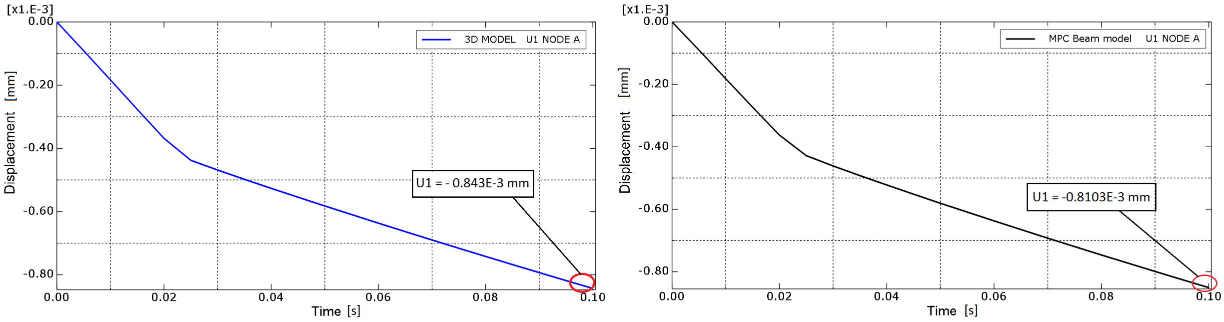

Figure 4.33: Problem 3, U2 displacement in node A and C respectevely for 3D model and MPC Beam model (TopSurface, shell thickness equal to s_1)

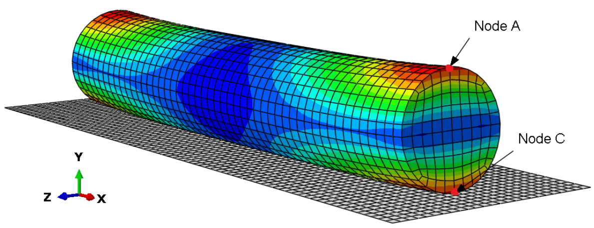

Figure 4.34: Problem 3, 3D model: Mises stress contour plot

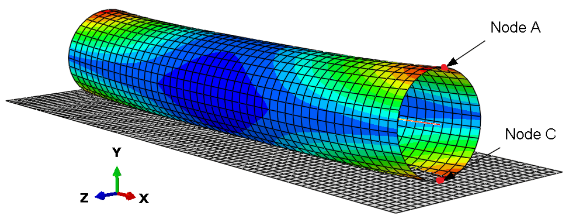

Figure 4.35: Problem 3, MPC Beam model: Mises stress contour plot

Figures 4.36 and 4.37 show the contour plot of contact normal force (CNORMF) for 3D model and MPC Beam mode, while in Figures 4.38 and 4.39 contact frictional shear force (CSHEAR) output are reported. Through these images it is possible to seen the distribution of normal and frictional shear force exchanged between the wire and the rigid plate during contact. Both for CNORMF and CSHEAR output, from an exclusively visual analysis, MPC Beam model force distribution is in good agreement with the plotted distribution of 3D model.
The percentage error correlated to the MPC Beam model use is evaluated. This is calculated referring to maximum values obtained for U1 displacement, Mises stress and contact output variables. Since numerical analysis are carried out with MidSurface approach and TopSurface approach, Tables 4.24 and 4.25 report the error for both analysed case. From Table 4.24, moving from s_1 to s_3 thickness the error decreases in terms of displacement but increase for Mises stress. Conversely, Table 4.25 shows an inverse trend for U1 displacement which increase when the shell thickness decrease. This is linked to the different modeling of shell reference surface. As already introduced during simplified model description, the use of offset approach for the definition of shell reference surface is suitable when the element is involved in a contact problem. This is confirmed by results on CNORMF and CSHEARF errors, reported in Table 4.25. Using TopSurface approach in MPC Beam point, contact output are in better agreement with those relative to 3D model, if s_1 thickness is considered.
As for problem 2, seeing Tables 4.24 and 4.25, globally the lower percentage errors are associated to s_1, remaining below 5%.

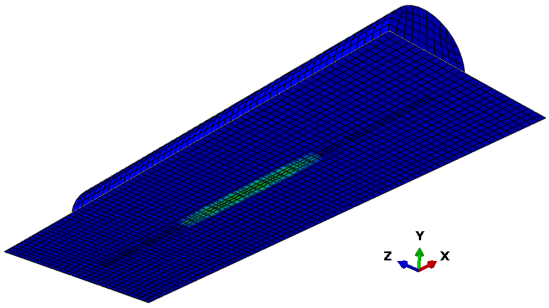

Figure 4.36: Problem 3, 3D model: CNORMF contour plot

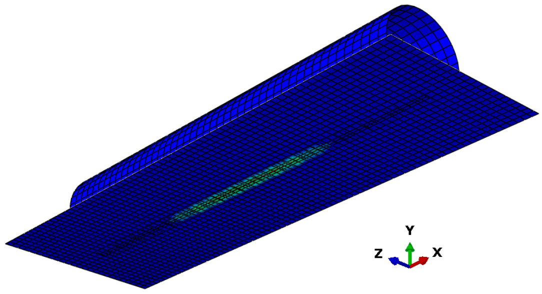

Figure 4.37: Problem 3, MPC Beam model: CNORMF contour plot

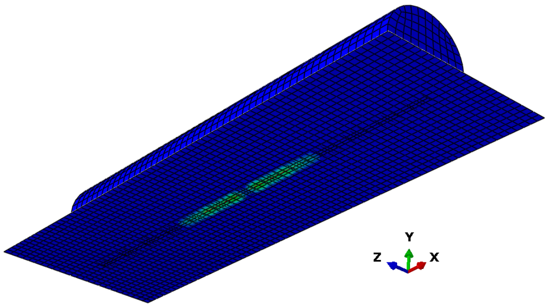

Figure 4.38: Problem 3, 3D model: CSHEARF contour plot

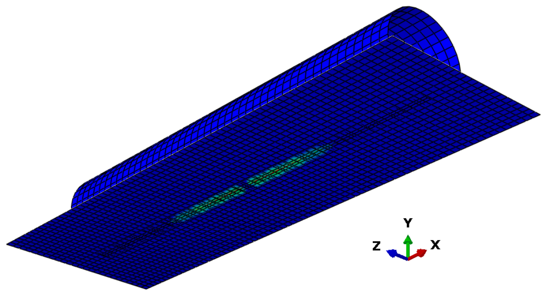

Figure 4.39: Problem 3, MPC Beam model: CSHEARF contour plot

MPC Beam model	**Error%** s_1	**Error%** s_2	**Error%** s_3
U1 displacement	3.9	0.9	3.3
Contact (CNORMF)	4.4	7.8	15
Contact (CSHEARF)	4.6	7.8	15
Mises stress	17	20	22

Table 4.24: Problem 3, Percentage error correlated to MPC Beam model considering MidSurface approach

MPC Beam model	**Error%** s_1	**Error%** s_2	**Error%** s_3
U1 displacement	0.45	0.9	4.2
Contact (CNORMF)	1	6.7	15
Contact (CSHEARF)	1	6.7	16.8
Mises stress	17	20	22

Table 4.25: Problem 3, Percentage error correlated to MPC Beam model considering TopSurface approach

4.2.2 Double_wire test

Consider as real reference object two wires having the features reported in Figure 4.40:

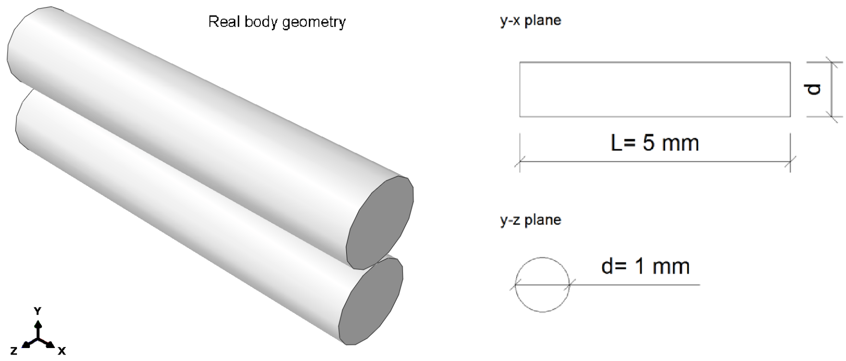

Figure 4.40: Real reference wires

Through *Double_wire* test the problem of two wires superimposed on each other is investigated, focusing on bending and contact behavior. For MPC Beam model both **MidSurface** and **TopSurface** options are tested as shell reference surface. Within the two models, three different shell thickness are evaluated. All analysis are executed using the Abaqus/Explicit solver.

- **3D model**: Bending + contact

For 3D model case two wires of equal length 5 mm are defined. Practically, a unique geometric part is created in Abaqus, then the second wire is generated and positioned by assembly module commands. In the initial configuration the wires are already in contact. The bottom wire (see Figure 4.41) present fully-fixed extremities; in top wire ends are defined two BCs (BCdx and BCsx) through which all translational degrees of freedom are constrained. An equal bending moment is applied to both top wire extremities. Bending moments and BCs are applied through reference points indicated in Figure 4.41. These are the retained points for the rigid bodies composed by nodes of solid end surfaces (see problem 2 and 3 of *Single_wire* tests).

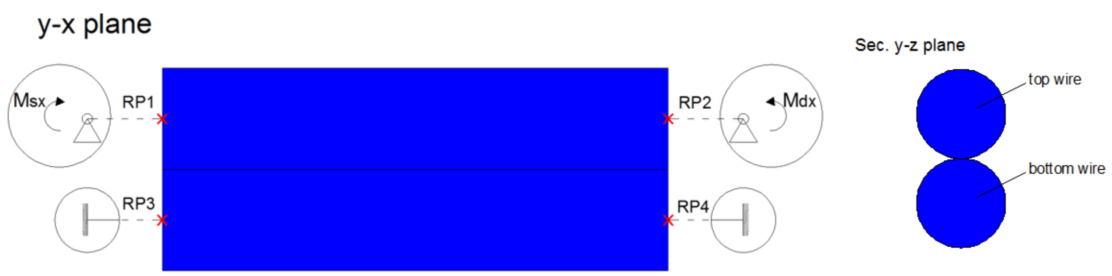

Figure 4.41: *Double_wire* test definition for 3D model

Linear, isotropic and elastic steel material is chosen for the wire parts. For structural discretization C3D8R element is used for the solid wires. The *Genaral contact (Explicit)* type of interaction is created for the model, associating to it *Tangential Behavior* property and specifying *Penalty* option as *Friction Formulation*. Tables below resume geometric problem characterisation and specifications related to material, mesh, BCs localization, load/step application and magnitude. Features indicated in tables are adopted throughout *Double_wire test* for 3D wire models.

Part	Part type	Section	Material	Element type	n° elements
BeamSolid	Wire	r = 0.5 mm	Steel	C3D8R	4800

Table 4.26: *Double_wire test*, 3D model parts description

Steel material	
Young modulus $E[N/mm^2]$	210000
Poisson's ratio ν	0.3
Density $\rho[Kg/mm^3]$	$7.86 \cdot 10^{-6}$

Table 4.27: *Double_wire test*, 3D model material properties

Step	Δt step [s]	Δt increment [s]
Initial	-	-
Load	0.1	1.95E-07

Table 4.28: *Double_wire test*, 3D model step definition

Wire geometry	
L [mm]	*r [mm]*
5	0.5

Table 4.29: *Double_wire test*, 3D model geometric properties

BCs	Type	Set	Initial step	Load step
Encastre	Encastre	RP3,RP4	created	propagated
BCdx	U1=U2=U3=0	RP2	created	propagated
BCsx	U1=U2=U3=0	RP1	created	propagated

Table 4.30: *Double_wire test*, 3D model boundary conditions

Load	Type	Set	Value	Axis	Step
Mdx	Moment	RP1	15 Nmm	z	Load
Msx	Moment	RP2	-15 Nmm	z	Load

Table 4.31: *Double_wire test*, 3D model load definition

- **MPC Beam model**: Bending + contact

For MPC Beam model case two wires of equal length 5 mm are defined. Practically, two geometric parts are created in Abaqus (Shell part and Beam part) to define the first wire, then the second wire is generated and positioned by assembly module commands. In the initial configuration the wires are already in contact. The bottom wire (see Figure 4.42) present fully-fixed extremities; in

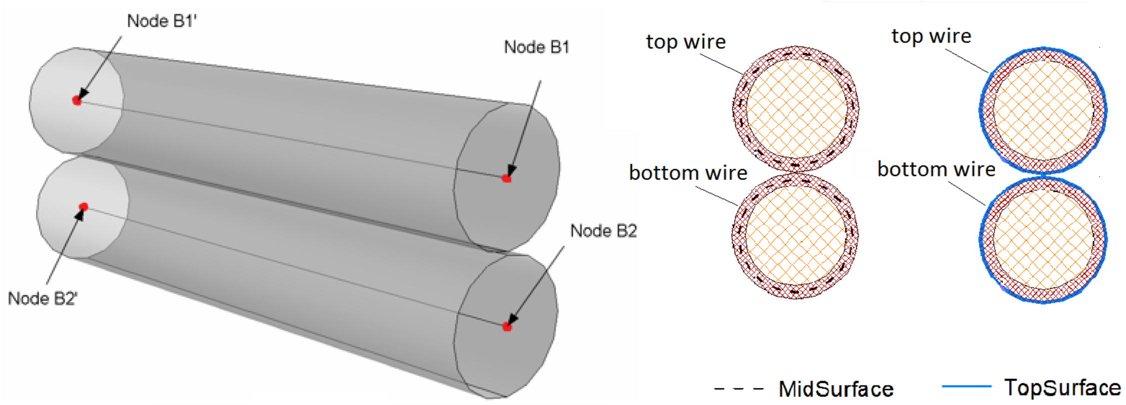

Figure 4.42: *Double_wire* test definition for MPC Beam model

top wire ends are defined two BCs (BCdx and BCsx) through which all translational degrees of freedom are constrained. An equal bending moment is applied to both top wire extremities. Top wire bending moments and BCs of are applied at nodes B1 and B1'; bottom wire encastre BCs are applied at nodes B1 and B2'(see Figure 4.42).

Part	Part type	Section	Material	Element type	n° elements	n° nodes
Beam	Wire	r_b = 0.48 mm	Steel	B31	46	47
Shell	Shell	r = 0.02 mm	Steel	S4R	1472	1504

Table 4.32: *Double_wire test*, MPC Beam model parts description

Steel material	
Young modulus $E[N/mm^2]$	210000
Poisson's ratio ν	0.3
Density $\rho[Kg/mm^3]$	$7.86 \cdot 10^{-6}$

Table 4.33: *Double_wire test*, MPC Beam model material properties

Step	Δt step [s]	Δt increment [s]
Initial	-	-
Load	0.1	3.96E-07

Table 4.34: *Double_wire test*, MPC Beam model step definition

Wire geometry	
L [mm]	*r [mm]*
5	0.5

Table 4.35: *Double_wire test*, MPC Beam model geometric properties

BCs	Type	Set	Initial step	Load step
Encastre	Encastre	B2,B2'	created	propagated
BCdx	U1=U2=U3=0	B1	created	propagated
BCsx	U1=U2=U3=0	B1'	created	propagated

Table 4.36: *Double_wire test*, MPC Beam model boundary conditions

Load	Type	Set	Value	Axis	Step
Mdx	Moment	B1	15 Nmm	z	Load
Msx	Moment	B1'	-15 Nmm	z	Load

Table 4.37: *Double_wire test*, MPC Beam model load definition

Tests are performed both for MidSurface and TopSurface model (in Figure 4.42 the position of either reference surfaces is indicated) and for each case the following shell thickness are tested:

- s_1 **= 0.025 mm**;
- s_2 **= 0.02 mm**;
- s_3 **= 0.01 mm**;
- s_4 **= 0.005 mm**.

In order to emphasize models behaviour, in the following, results related to 3D model and MPC Beam model are directly compared. In this problem displacements, stress and contact output are evaluated. For simplicity, only figures and diagrams correlated to TopSurface MPC Beam model characterised by s_1 shell thickness are presented. 3D model and MPC Beam model show a similar contour plot for U1 displacement. This is visible by the colour distribution in Figures 4.43 and 4.44. Figure 4.44 refers to MPC Beam model having s_1 thickness, but similar contour plot can be found for other analysed thickness. The same consideration can be made for the others output taking into account (see Figures 4.45-4.50). The displacement along x-axis is measured in nodes A1 and C1, where the value is maximum. Figures 4.45 and 4.46 show tho contour plot of the CNORMF for 3D model and MPC Beam mode, while in Figures 4.47 and 4.48 CSHEAR output are reported. In order to make more immediate viewing contact areas, from the assembly view only the bottom wire is considered and shown in figures. Through these images it is possible to seen the distribution of normal and frictional shear force exchanged between the wires. Both for CNORMF and CSHEAR output, from an exclusively visual analysis, MPC Beam model force distribution is in good agreement with the plotted distribution of 3D model.

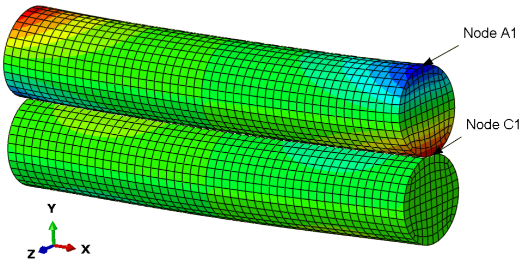

Figure 4.43: *Double_wire test*, 3D model: U1 displacement contour plot

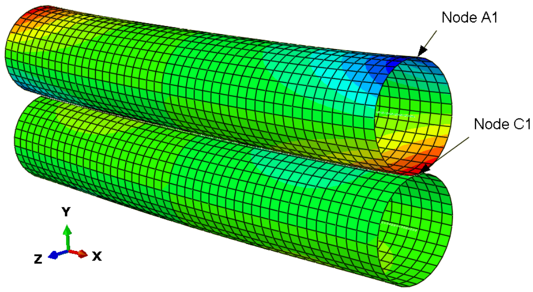

Figure 4.44: *Double_wire test*, MPC Beam model: U1 displacement contour plot

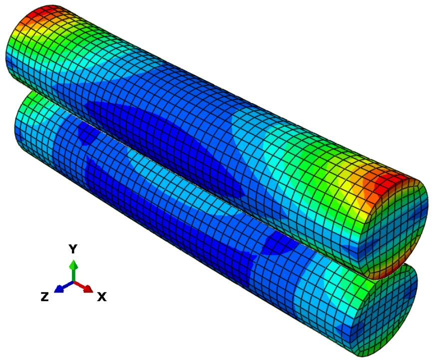

Figure 4.45: Problem 3, 3D model: Mises stress contour plot

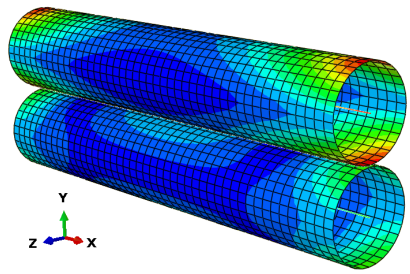

Figure 4.46: Problem 3, MPC Beam model: Mises stress contour plot

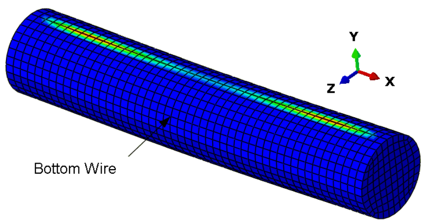

Figure 4.47: *Double_wire test*, 3D model: CNORMF contour plot

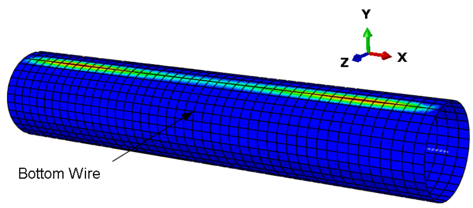

Figure 4.48: *Double_wire test*, MPC Beam model: CNORMF contour plot

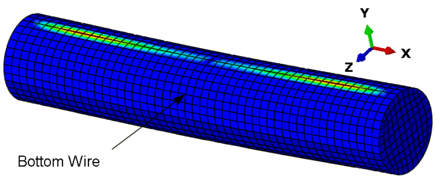

Figure 4.49: *Double_wire test*, 3D model: CSHEARF contour plot

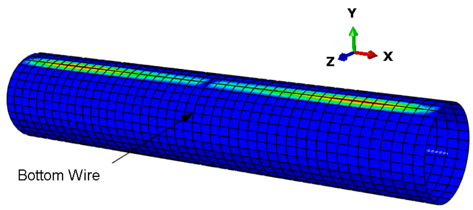

Figure 4.50: *Double_wire test*, MPC Beam model: CSHEARF contour plot

MPC Beam model	Error% s_1	Error% s_2	Error% s_3	Error% s_4
U1 displacement	5.8	2.4	8.5	25
Contact (CNORMF)	4.8	5.2	29	44
Contact (CSHEARF)	4.8	5.2	29	44
Mises stress	9.5	11	14.6	16.7

Table 4.38: *Double_wire test*, Percentage error correlated to MPC Beam model considering TopSurface approach

MPC Beam model	Error% s_1	Error% s_2	Error% s_3	Error% s_4
U1 displacement	0.34	1.9	11.6	26
Contact (CNORMF)	2.3	10	31	44.6
Contact (CSHEARF)	2.3	10	31	44.6
Mises stress	9.3	7.4	15	16.7

Table 4.39: *Double_wire test*, Percentage error correlated to MPC Beam model considering TopSurface approach

The percentage error correlated to the MPC Beam model use is evaluated. This is calculated referring to maximum values obtained for U1 displacement, Mises stress and contact output variables. Since numerical analysis are carried out with MidSurface approach and TopSurface approach, Tables 4.38 and 4.39 report the error for both analysed case. From Table 4.38, moving from s_1 to s_3 thickness the error decreases in terms of displacement but increase for Mises stress. Conversely, Table 4.39 shows an inverse trend for U1 displacement which increase when the shell thickness decrease. This is linked to the different modeling of shell reference surface. As found in *Single_wire tests* problem 3, the use of TopSurface approach in MPC Beam model has a positive effect on contact output; these appear in better agreement with those relative to 3D model is s_1 thickness is considered. As for problem 2 and 3 of *Single_wire tests*, seeing table related to MidSurface approach, globally the lower percentage errors are associated to s = 0.02 mm. Instead, from Table 4.39 it possible to seen that for TopSurface approach the best thickness value is $s_1 = 0.025$ mm.

4.3 Matlab code for MPC Beam model implementation

In section 4.1 steps required to model a simple wire with MPC Beam method has been presented. When complex geometries such as strands are involved in numerical analysis, the use of the presented simplified approach appears complicated. The problems faced during the modeling phase concerning the definition of MPC constraints. As explained in section 4.1, to create an MPC constraint it needs to define a set for the control point and a set for the slave points of shell section. As example, if 20 MPC constraints are defined for the model, corresponding 40 nodal sets must be created, 100 MPC imply 200 nodal sets and so on. Therefore, if the problem studied refers to a simple wire with a discrete mesh it is possible to made this operation manually, through Abaqus/CAE commands. Obviously this is not conceivable for complex cases, such as the strand studied in chapter 3.
In order to simplify and make serviceable the implementation of MPC Beam model, a Matlab code has been created. The purpose of the program is generate in an automatically manner the Abaqus input file for the construction of strand geometry and MPC constraints. This input file includes parts geometry and mesh features (coordinates, number of elements, type of element), assembly instances and MPC constraints (with relative nodal sets). The Matlab code has been thought on the basis of strand reference model. With this program it is possible to create a strand characterised by a central core, two outer layers (wrapped in a right-hand or left-hand way), selecting freely the desired mesh. Geometric parts created by matlab code, for a total number of 6

parts, are illustred in Figure 4.51.

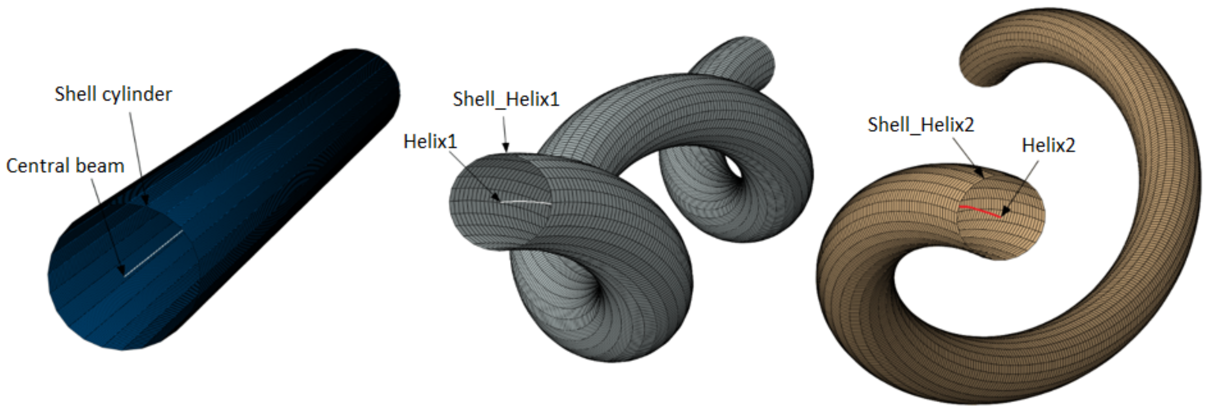

Figure 4.51: Geometric parts generated by Matlab code

The default wires' number of the first layer is 6, while for the second layer is 12. However, this parameter can be changed within the subroutine that generate the assembly configuration. Both circular and elliptic section can be defined for shell parts. Input parameters necessary to run the program and to generate the strand are specified in the following[3] :

CENTRAL WIRE

- **beta_0** → central wire lay
- **L_0** → strand length
- **mesh_node_coil** → number of element for each coil
- **r_shell** → shell part radius
- **n_nodes_circ** → number of elements in shell edge subdivision (circumference)

LAYER 1

- **flag_handed** → way of winding
- **r_1** → helix radius for layer 1
- **r1_coil** → shell part radius for layer 1

LAYER 2

- **flag_handed** → way of winding
- **beta_2** → pitch length for layer 2
- **r_2** → helix radius for layer 2
- **r2_coil** → shell part radius for layer 2

In Figure 4.52 three models with progressively finer mesh are illustrated. These have been obtained using the Matlab code which allows to simply generate the required MPC constraints depending on the type of mesh chosen.

[3]Input parameters provided, refers to a strand having all component wires characterised by circular section

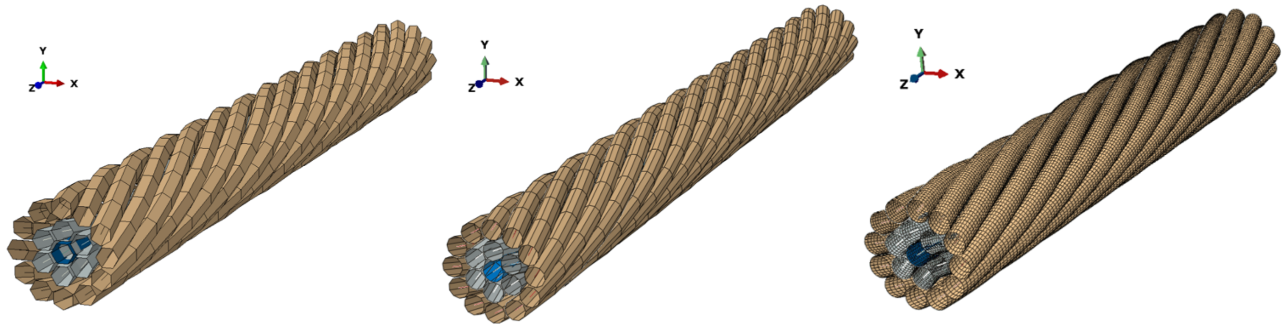

Figure 4.52: Different mesh generated by Matlab code for a 19-wires strand

4.4 MPC Beam Model in strand analysis

In the present section, the simplified model is tested for the strand problem. The goal of this test is create a strand MPC Beam model with the following features:

- a reduced number of DOFs compared to the reference model;
- ease in model implementation (matlab code for the automatic generation of the strand model);
- able to simulate the quasi-static problem presented for the reference model.

This simplified model is compared with an equivalent 3D model. For either cases, the Reference strand model described in chapter 3 is taken for cable design and load case definition. Linear, isotropic and elastic steel material is chosen for the strand. In the following, MPC Beam model and 3D model jobs are respectively indicated with *MPC BEAM MODEL_ CS* and *3D MODEL_ CS*. For simplicity, a circular section is adopted for all strand wires, both for MPC Beam model and 3D model (this justify the use of suffix "CS" in job names). Therefore, default parameters of input (indicated in section 4.3) are inserted in matlab code to automatically generate the MPC Beam strand. The TopSurface option is adopted as the shell reference surface in MPC Beam model. All strand wires section present a radius equal to 0.3 mm and a thickness equal to 0.02 mm is chosen for Shell part. This value comes from some tests performed on two wire having r = 0.3 mm and same length of reference strand model. The characteristic 3D elements dimension is 0.086 mm x 0.086 mm, that imply a mesh of $\cong 1 \cdot 10^6$ nodes. In order to obtain a similar global seeding for MPC Beam model, the shell characteristic dimension is chosen equal to 0.078 mm x 0.08 mm. Below, a summary of the two models characteristics is reported.

Models features

- *3D MODEL_ CS*

- Geometry of 19-wires strand: central core, first layer of 6 wires (wrapped in right-hand way), second layer of 12 wires (wrapped in left-hand way). The total strand length is equal to 62.8 mm, with a radius of 0.3 mmm characterising each wire and a total strand diameter of 3 mm;
- Material: conventional steel, with Young modulus E = 210000 N/mm^2, Poisson ratio ν = 0.3 and density $\rho = 7.86 \cdot 10^{-6}$ kg/mm^3;
- Mesh: the discretization is realised on parts and the total nodes number is $\cong 1 \cdot 10^6$. C3D8R type element type is used for the mesh;
- Analysis steps:

- step initial → encastre constraint definition;
- step displacement → longitudinal displacement definition (0.8 mm Z-direction) and assignment of the sinusoidal transversal cycle displacement (10 mm Y-direction, 0 X direction) associated with the respective Amplitudes.

- Contact interaction: General Contact (Abaqus/Explicit);
- Output:
  - contact area and total force of contact → *contact-surf* surface;
  - history of nodal assigned displacements → *central node* set;
  - forces/reactions → *bottom-surf* surface;
  - forces/reactions → *up-surf* surface;
  - energy → *whole model* .

Reference strand model is adopted also for MPC Beam strand, except for the following specifications:

- *MPC BEAM MODEL_ CS*

- Geometry of 19-wires strand: geometric parts are generated directly through the matlab code. ;
- Mesh : the discretization is realised on parts through the matlab code. The mesh created is of $\cong 4 \cdot 10^5$ nodes. B31 element type is used for the Beam part, while S4R element type is used for the Shell part;
- Kinematic constraints: MPC beam type constraints are generated through the matlab code;
- BCs: encastre constraint, longitudinal displacement and sinusoidal transversal cycle are applied on extremities section nodes (see Figure 4.53);
- Output:
  - contact area and total force of contact → *contact-surf* surface;
  - history of nodal assigned displacements → *central node* set;
  - forces/reactions → these are obtained through the sum of all single forces/reactions calculated on extremities section nodes;
  - energy → *whole model* .

Analysis presented in this section are performed on CINECA hardware resources, using parallel execution method. Parameters chosen to run both simulations are the same reported in chapter 5, Figure 5.3. The high number of DOFs characterising 3D model make it very expensive from the computational point of view. For the *3D MODEL_ CS* job, a mass scaling of 2 % is chosen, in order to complete strand simulation time. An attempt of simulation without using mass scaling approach has been carried out through *3D MODEL_ CS_ 0MS* job, but this has been interrupted for an exceeding of time. These assumptions will be explained in chapter 5, where computational resources used to run all strand analysis are motivated and described in detail.

3D and MPC Beam strand FEA are summarized in Table 4.40. Starting from the same computational resources (CPUs, nodes and RAM/node), it can be observed that 3D model completes the simulation time only helped by mass scaling, while this is not required for MPC Beam case. MPC BEAM MODEL_CS job however use less time to reach the end of the simulation. It should be noted that MPC Beam model has a Δt stable equal to 3E-07 s, less than 3D model stable time increment (although this value is forcedly set to Δt=4.38E-07 s by mass scaling). Nevertheless,

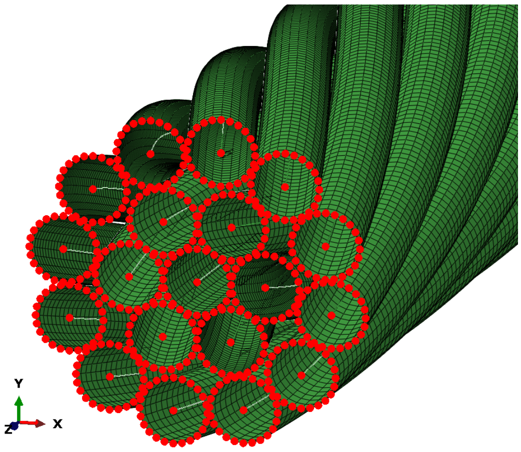

Figure 4.53: Extremities section nodes of MPC Beam strand model

Job Name	Material	N°nodes	DOFs	Walltime	M.Scaling	Step completed
3D MODEL_CS_0MS	Steel	$\cong 1 \cdot 10^6$	$\cong 3 \cdot 10^6$	$>$ 24 h	-	17 of 20
3D MODEL_CS	Steel	$\cong 1 \cdot 10^6$	$\cong 3 \cdot 10^6$	15 h	2 %	20 of 20
MPC BEAM MODEL_CS	Steel	$\cong 4 \cdot 10^5$	$\cong 3 \cdot 10^6$	14 h	-	20 of 20

Table 4.40: 3D model and MPC Beam model strand FEA

the strong decrease of DOFs involved in MPC BEAM MODEL_CS job has allowed the achievement of final simulation step, without intervening in the dynamics of the problem through mass scaling. Following, some interesting FEA results are reported. The output considered, refer to the condition of inter-wires contact, the energy dissipated by strand, the total axial and transversal force.

- **Kinetic and internal energy**

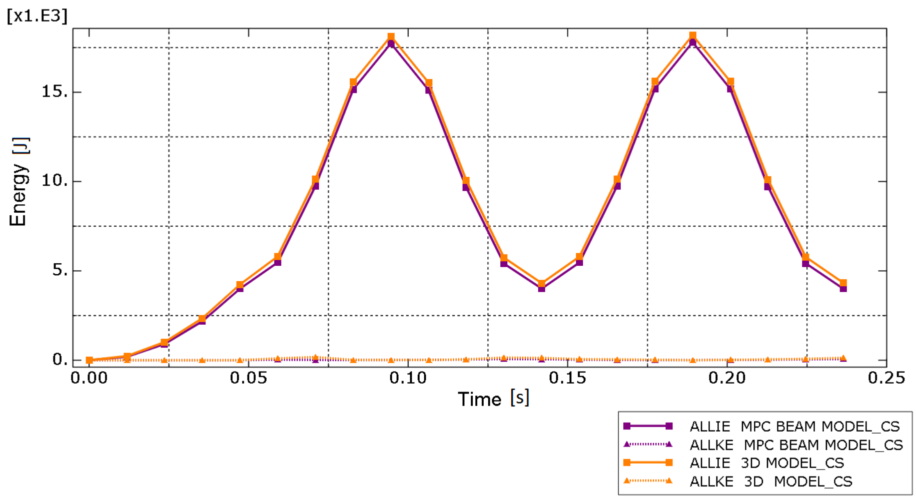

Figure 4.54: Kinetic and internal energy on the *whole model* related to MPC Beam and 3D model analysis

The problem analysed by Reference strand model, thus in 3D MODEL_CS and MPC BEAM MODEL_CS jobs is a quasi-static simulation. An indicators of problems when reviewing the energy balance is excessive of kinetic energy (ALLKE). This rate energy should be a small fraction (typically 5–10%) of the internal energy (ALLIE). Therefore, a first control on the validity of simulation, especially for MPC Beam model case, is made on over-cited energy output. Figure 4.54 shows a convergence of curves relative to the different two models and overall and a compliance with the condition imposed on kinetic energy.

- **Area in contact**

Figure 4.55 present the trend of area in contact over the simulation time. As it can be observed from diagram, MPC Beam model seems to overestimate the area in contact and disagree with 3D model curve, although the trend shape is quite similar. This can be attributed to shell thickness chosen; as shown during *Single_wire tests* and *Double_wire test* the variability of shell thickness has a strong influence on output values, especially for contact output (see Tables 4.24,4.25, 4.38,4.39).

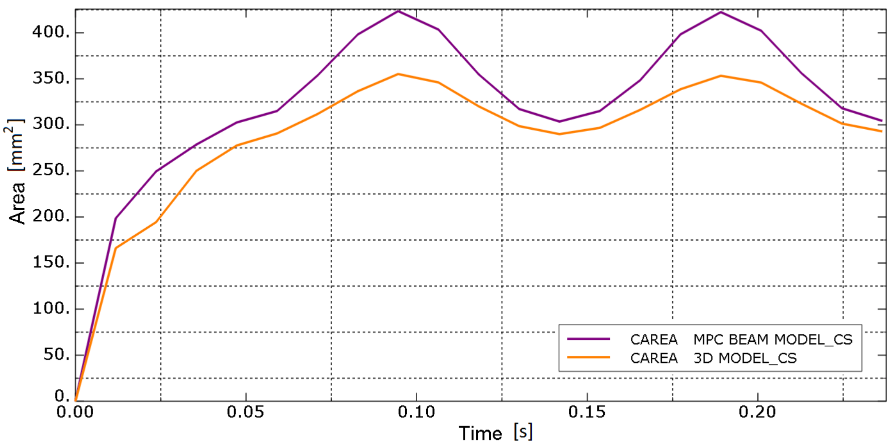

Figure 4.55: Area in contact on the *contact-surf* surface related to MPC Beam and 3D model analysis

- **Total axial force and transversal force**

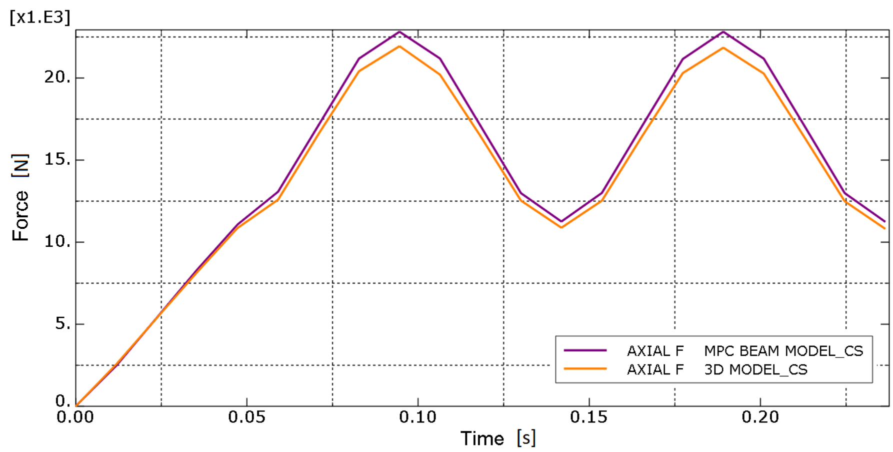

Figure 4.56: Total axial force related to MPC Beam and 3D model analysis

The axial loading behavior of strand is investigated by an axial displacement of 0.8 mm applied on section surface and on extremities section nodes respectively for 3D model and MPC Beam model. This value is reached at 0.05 s, then the pretension is kept constant throughout the simulation, during the application of the sinusoidal transversal cycle. Figure 4.56 shows the total axial force obtained for 3D MODEL_CS and MPC BEAM MODEL_CS jobs. The percentage of deviation between two curves is found to be of 7%. Figure 4.57 shows the result transversal force obtained for 3D MODEL_CS and MPC BEAM MODEL_CS jobs. In this case the influence of mass scaling used in 3D model simulation is most evident and the instability of output values probably is due to this phenomenon. The percentage of deviation between two curves is found to be of 8%. For both quantities, the percentage error is estimated referring to maximum stress values.

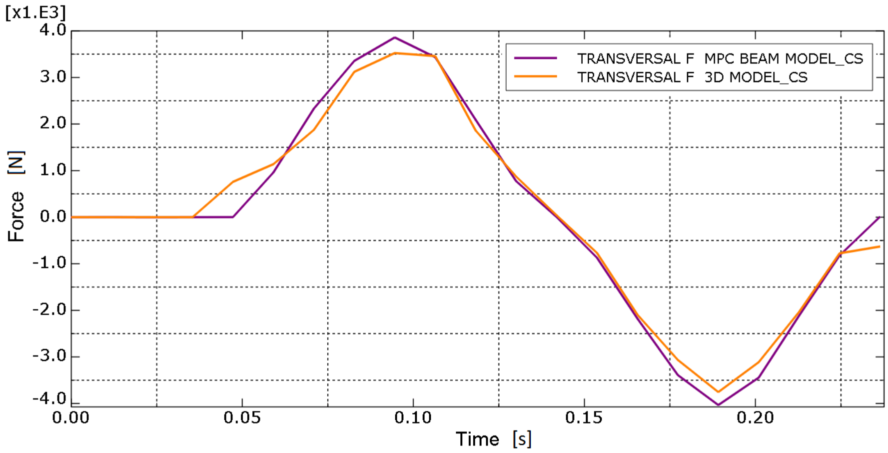

Figure 4.57: Total transversal force related related to MPC Beam and 3D model analysis

- **Frictional energy dissipation**

Figure 4.58 present the frictional energy dissipation (ALLFD) on the *whole model*. As it can be observed from diagram, MPC Beam model and 3D model curves diverge progressively with the increase of time increment. MPC Beam model has a greater area in contact than 3D model, while ALLFD energy is less for the first model. The ratio between area in contact and the friction dissipated energy is not trivial: the first depends strongly on mesh density, while friction dissipation is associated to forces exchanged between wires. The greater "stiffness" characterising the MPC Beam model, linked to the MPC kinematic constraint, may have led to an erroneous estimation of these forces. Mass scaling use for 3D MODEL_CS could have influenced 3D model energy results.

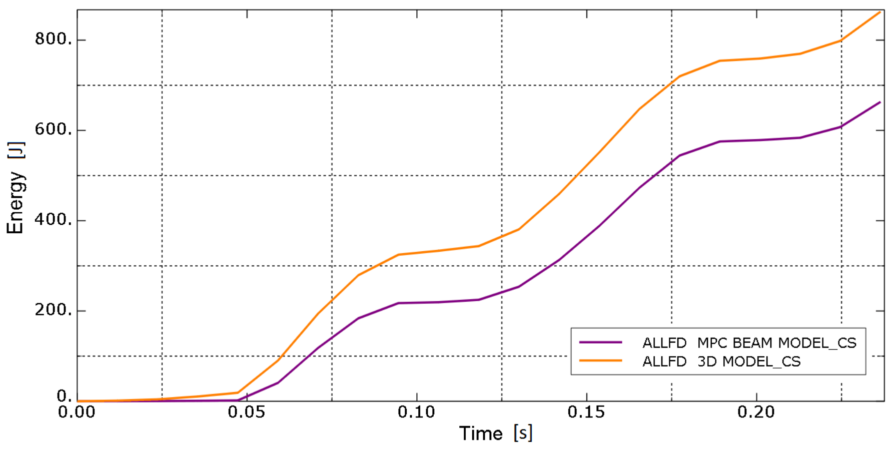

Figure 4.58: Frictional energy dissipation on the *whole model* related to MPC Beam and 3D model analysis

4.5 Considerations about MPC Beam model

Within FEA, several factors that could influence MPC Beam model behavior have been taken into account. Factors considered are the variation of shell thickness, the shell reference surface approach (*MidSurface* model and *TopSurface* model), mesh discretization (both for 3D model and MPC Beam model) and method of application of BCs on the MPC Beam model. Numerical results show that:

- an adequate mesh discretization is fundamental for the correct prediction of models response both for 3D and MPC Beam model, overall when a rigid surface is involved in the problem analysed ((*Single_wire tests*, problem 1, 3D model);

- problem 1 results for MPC Beam model (*Single_wire tests*) confirm that this model totally neglects punch effect linked to application of a traction load on the wire. Nevertheless, in real strands this effect plays generally a little role and this limitation is not considered so effective in problem evaluation;

- the variation of shell thickness strongly affects percentage error deviation between 3D and MPC Beam model. This is clearly observed by seen Tables 4.24-4.25 of *Single_wire tests* (problem 3) and Table 4.38-4.39 of (*Single_wire tests*). It is observed that for a wire of radius equal to 0.5 mm, the most reasonable value for the shell thickness stands in the range of 0.02-0.025 mm. Especially in terms of contact output, the percentage errors increase when a thickness less than 0.02 mm is chosen;

- using two different approaches for BCs definition (BCs applied on Beam part end nodes or BCs applied on Reference points after the definition of extremities rigid bodies) leads to identical output results, thus this factor not influence the MPC Beam model response;

- MPC Beam model based on TopSurface approach leads to best results for all performed tests.

In order to test the simplified model in a complex real problem, a MPC Beam strand model has been created on the basis of Reference strand model. Given the difficulties in manually implementing the 19-wires strand problem for the simplified model, a Matlab code that allows to automatically generate geometry, mesh and constraints has been developed. MPC Beam strand model has been compared with the equivalent 3D 19-wires strand model. In either cases, circular sections with equal radius have been adopted for each wire. Evaluated output refer to inter-wires contact condition, kinetic energy, frictional dissipated energy and total transversal/axial force calcuted on strand extremity. The comparison between MPC Beam model and 3D model FEA shows that:

- MPC Beam model presents a strong reduction of DOFs if compared to the equivalent 3D model ($\cong 2 \cdot 10^6$ DOFs against $\cong 3 \cdot 10^6$ DOFs of 3D model), leading to a reduced cost from the computational time point of view;

- MPC Beam model respects condition imposed on kinetic energy rate and it is able to reproduce a quasi-static simulation;

- MPC Beam model otuput are in good agreement with those relative to 3D model in terms of total axial force and transversal axial force prediction. Instead, contact output and specifically the area in contact show a greater discrepancy between two models;

- frictional energy dissipation curves globally presen a not trivial error deviation, although a similar trend is noticed.

Results associated to *Single_wire tests* and *Double_wire test* appear promising, relatively to the considered output. Comparing analysis times, there is a strong saving in terms of computational costs using MPC Beam model. For example, considering *Double_wire test*, 3D model takes 52 minutes to complete the simulation, while MPC Beam model only 6 minutes (for equal computational resources). Nevertheless, factors that could influence the goodness and the validity of MPC Beam model are in number too high for a practical use of the method. An accurate investigation should be carried out on parameters calibration, on the influence of the ratio shell thickness-section dimensions and on problems encountered in the performed tests. Another disadvantage is the "stiffness" introduced in the model by MPC constraints, that inhibit stretching-induced geometric non-linearity presented between wires when these come into interaction with each others. These weaknesses are underlined moving from simple tests to the complex strand problem. Analisyng results from 3D MODEL_CS and MPC BEAM MODEL_CS jobs it can be seen a good correspondence in the total axial and transversal force measured at the strand extremity, but the same considerations can not be made over contact and energy output. Further output such as normal and shear contact pressure,not reported in this context, have been compared showing a progressive increase of error in MPC Bema model strand. Though the model offers a first approximation of the cable response, similar to that provided by 3D modeling, there is need for a more accurate and validated model for use in real structural cables simulations. For this reason, for the comparison of Steel and SMA strand behavior only conventional 3D modeling is considered. The complexity of SMA material behavior associated to the intrinsic problematic of strand problem require a robust well tested modeling method, while simplified model is approximate and dependent on variables till uncertain. .

Chapter 5

Steel and SMA strand comparison

In this chapter differences between conventional steel strands and SMA strands response are highlighted, referring to a particular case of study. For both material, the Reference strand model described in chapter 3 is taken for cable design and load case definition. Three different mesh are considered for the strand in exam and mass scaling approach is addressed. Due to the problem complexity and cost from the computational point of view, a cluster outfitted with different CPUs[1] is required. CINECA HPC[2] systems are presented, focusing on used hardware and software resources, reporting the launch setting parameters to run strands FEA. Finally, analysis results are compared and considerations about some specific quantities are made to underline different materials behavior.

5.1 CINECA HPC resources

At the end of the 60' the need of powerful supercomputers for the scientific computing was clearly felt by the Italian academia. In 1969 the Ministry of Education supported four Italian Universities in their effort of consortiating with the aim of creating a supercomputing center, CINECA, hosting the first CDC 6600 designed by Seymour Cray[3], the father of supercomputing and the first supercomputer located in Italy. Today CINECA is a non profit Consortium, made up of 69 Italian Universities and 3 Institutions. SCAI (SuperComputing Applications and Innovation) is the High Performance Computing department of CINECA. The mission of SCAI is to accelerate the scientific discovery by providing high performance computing resources, data management and storage systems, aiming to develop and promote technical and scientific services related to high-performance computing for the Italian and European research community.

CINECA HPC resources are divided in Hardware resources and Software resources.

- **Hardware resources**

CINECA hardware resources are among the most powerful available in Italy.
At present the main HPC system is ***FERMI***, composed of 10240 computing nodes characterised with a memory of 16GB/node and 16 cores each , for a totalling 163840 compute cores. The ***PLX-GPU***[4] supercomputer has been introduced in June 2011 and it is available to Italian industrial and public researchers: it is composed of 274 computing nodes of 48 GB of memory each,

[1]CPU is the acronym for Central Processing Unit

[2]HPC is the acronym for High Performance Computing

[3]Seymour Roger Cray (September 28, 1925 – October 5, 1996) was a U.S. electrical engineer and supercomputer architect who designed a series of computers that were the fastest in the world for decades, and founded the company Cray Research which would build many of these machines. Called "the father of supercomputing," Cray has been credited with creating the supercomputer industry through his efforts

[4]A graphics processing unit (GPU), also occasionally called visual processing unit (VPU), is a specialized electronic circuit designed to rapidly manipulate and alter memory to accelerate the creation of images in a frame buffer intended for output to a display

528 GPUs, with a totalling 3288 compute cores. Supercomputer ***EURORA*** (EURopean many integrated cORe Architecture) is the result of a project founded by PRACE[5] framework. The new supercomputer design addresses the current, most important HPC constraints (sustainable performance, space occupancy and cost) by combining hybrid technology to efficient cooling and a custom interconnection system. Eurora prototype is composed of 64 computing nodes characterised with a memory of 16GB/node, with a totalling 1024 compute cores.

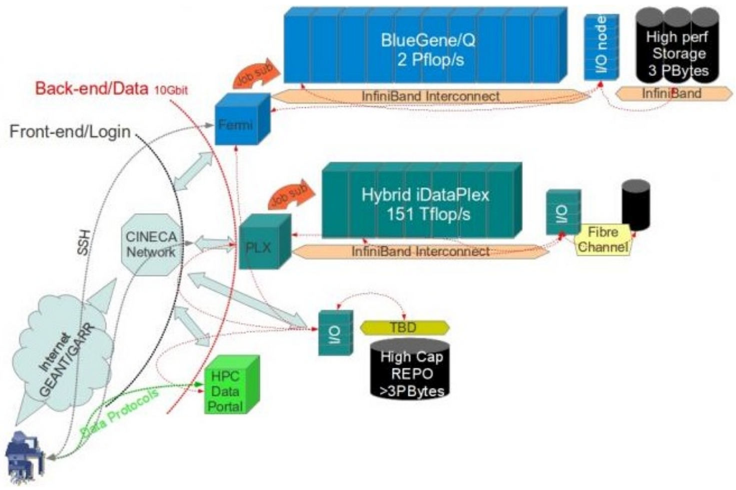

Figure 5.1: The SCAI Hardware Infrastructure

– **Software resources**

To support scientific and technological research with computational tools, CINECA provides *System Softwares* and programming environments (Fortran77, Fortran90, C, C++ compilers; the MPI library, standard for the development of parallel computing codes etc.).
Cineca offers a variety of third-party applications and community codes that are installed on its HPC systems. The packages available are subdivided by discipline (Chemistry, Physics, Engineering, Astronomy etc.). Within the Engineering software resources, several application programs are available, including Abaqus Finite Element Analyzer. Abaqus FEA can be performed on EURORA and IBM PLX systems.

In order to have access to use CINECA HPC resources it needs to be associated to a valid project. At present, among the active projects on HPC systems there are LISA Projects: the projects' goal is to activate applied plans to increase and enhance the attraction and the national and International integration of the Lombard territory in advanced areas of research and development.
Within LISA project Abaqus strands FEA are conduced. In subsection 5.1.1 used software resources are specified together with the parameters of launch to run Abaqus simulations.

5.1.1 PBS batch job for strands FEA

For the present case of study, PLX system is chosen between the hardware resources available for Abaqus software. This choice has been achieved after a series of analysis carried out on Reference strand model, testing the different computational queues available on EURORA and PLX systems and related possible resources requirements.
Parallel execution method is used to run strands FEA on CINECA resources. Parallel execution in

[5]PRACE (Partnership for Advanced Computing in Europe) created a persistent European Research Infrastructure (RI) providing High Performance Computing (HPC) resource, with a strong interest in improving energy efficiency of computing systems and reducing their environmental impact

Abaqus/Explicit reduces run time for analyses that contain a large number of nodes and elements. It is available for both shared memory computers and computer clusters using an MPI-based domain decomposition parallel implementation. The domain-level method splits the model into a number of topological domains. These domains are referred to as parallel domains to distinguish them from other domains associated with the analysis. The domains are distributed evenly among the available processors. The analysis is then carried out independently in each domain. However, information must be passed between the domains in each increment because the domains share common boundaries [51].
As first attempt, FEA are submitted on EURORA *parallel* queue. This queue is characterised by a max nodes number equal to 32 and a maximum walltime[6] of 4 hours, aimed to parallel production usage. The walltime available is resulted insufficient since the first tests, even addressing a large number of nodes. Thus, given the possibility within the LISA project of using also PLX resources, the subsequent attempts of simulation are performed on a specific queu provided on the mentioned cluster. On PLX it is possible to submit jobs on different queues, each identified by different resource allocation:

job type	Max nodes	Max CPUs/GPUs	max wall time	wait time
debug	2	24/ 4	0:30:00	minutes
parallel	44	528/88	6:00:00	hours
$\boxed{\text{longpar}}$	22	264/44	24:00:00	1 day
archive	1	1	04:00:00	-
big1	1	32/1	72:00:00	-
big2	1	40/0	72:00:00	-

Figure 5.2: PLX available queues

In Figure 5.2 the chosen job type is highlighted. The *longpar* queue is characterised by a maximum number of nodes equal to 22 and a limit of walltime equal to 24 hours. Before defining the resource requirements some clarifications about Abaqus software are needed. Abaqus is not a massively parallel code, thus a strong increase of cores number does not correspond to a proportional decrease of computational time. However, the real problem is the availability of licenses: Abaqus has a maximum of 40 licenses (actually 28 at the moment of request since 12 were already in use), and each parallel job requires it 4 + n core licences. According to these considerations, the PBS[7] batch job to run Abaqus analysis is defined. With PBS a batch job is created which and then submit to PBS. A batch job is a file (a shell script under UNIX) containing the set of commands you want to run. It also contains directives which specify the characteristics (attributes) of the job, and resource requirements (e.g. number of processors and CPU time) that your job needs.
The PBS batch job used to run strands FEA asks for 24 hours to the maximum wall clock time and run a MPI application, requesting 2 node with 12 CPUs/node and sending the job in the longpar scheduler queue. The requested memory for the single node is of 47 GB. In this way a total of 28 licences are required by the parallel job, 4 licences for Abaqus application software and 1 license for each CPUs, remaining within the limits allowed. Figure 5.3 shows the typical job script defined for the strands analysis accompanied by a summary table of requirements.
All HPC systems share the same logical disk structure and file systems definition. The available storage areas can be *temporary* or *permanent*. In this case script job file and input job file are saved within the *$CINECA_SCRATCH* temporary area. This is a local temporary storage, conceived

[6]In computing, walltime or wall-clock time means the actual time taken by a computer to complete a task.[1] It is the sum of three terms: CPU time, I/O time, and the communication channel delay (e.g. if data are scattered on multiple machines). In contrast to CPU time, which measures only the time during which the processor is actively working on a certain task, wall time measures the total time for the process to complete. The difference between the two consists of time that passes due to programmed delays or waiting for resources to become available. For programs executed in parallel, the CPU time will be the sum of CPU times devoted to the task by each CPU running it. In this case the wall time will be substantially reduced (it takes less perceived time to finish), whereas the total CPU time will remain equal to the one for serial execution (plus some overhead for parallelization)

[7]Portable Batch System (or simply PBS) is the name of computer software that performs job scheduling. Its primary task is to allocate computational tasks, i.e., batch jobs, among the available computing resources

```
#PBS -N abq_job                                    --> specify job name
#PBS -r n
#PBS -j oe
#PBS -l walltime=24:00:00
#PBS -l select=2:ncpus=12:mpiprocs=12:mem=47GB     --> MPI job
#PBS -A LI01p_PASCA2LP                             --> only for account based usernames
#PBS -q longpar                                    --> specify the queue destination
```

Walltime	24 h
N nodes	2
N CPUs/node	12
N tot CPUs	24
RAM/node	47 GB

Figure 5.3: PBS batch job used to run strands FEA

for hosting large temporary data files, since it is characterized by the high bandwidth of a parallel file system. It behaves very well when I/O[8] is performed accessing large blocks of data, while it is not well suited for frequent and small I/O operations.

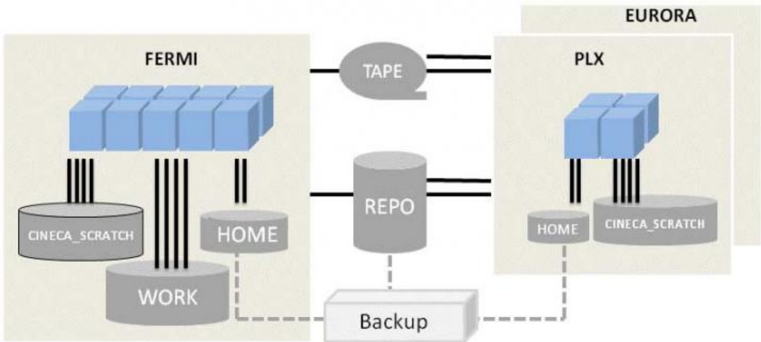

Figure 5.4: HPC system avalilable data areas

5.2 Analysis framework

The job-test for the parameters of launch is the *Strand3D_Mesh0* job, corresponding to the Strand Reference model. Editing history output request for this simulation, the frequency of output writing is setted every 20 time increments. This contributes to reducing the time of calculation together with the mass scaling and the parallel job execution. The *Strand3D_Mesh0* status file indicates that the job has been interrupted during the analysis due to an excess of walltime, completing 17 steps of 20. A SMA strand (*Strand3d_Mesh0_SMA* job) with the same Reference model cable design is created. Using the fixed parameters of launch this analysis has been submitted, but as for *Strand3D* job it has been interrupted for exceeding the walltime. In this case, 0 step of 20 have been completed and correlated output are practically unusable.
For the reasons explained in the previous section, a change on parameters of launch, for example an increase of nodes or CPUs, is not effective to obtain reduced computational times. An approach to obtaining economical quasi-static solutions with an explicit dynamics solver is the *Mass scaling* method, discussed below. Furthermore, in order to obtain a more complete output for the SMA-steel comparison, three different mesh are considered:

- **Mesh0** of $\cong 1 \cdot 10^6$ nodes, corresponding to Reference model strand discretization (approximate seed global size equal to 0.085);
- **Mesh1** of $\cong 7 \cdot 10^5$ nodes (approximate seed global size[9] equal to 0.1);
- **Mesh2** of $\cong 5 \cdot 10^5$ nodes (approximate seed global size equal to 0.12).

[8] I/O is the acronym for Input/Output operation
[9] In Abaqus mesh module it is possible to specify the average element size for every edge of the entire part or part instance

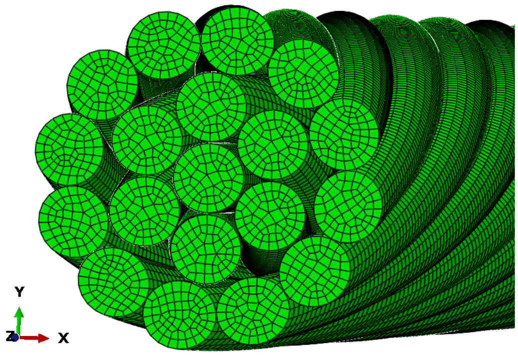

Figure 5.5: Mesh0

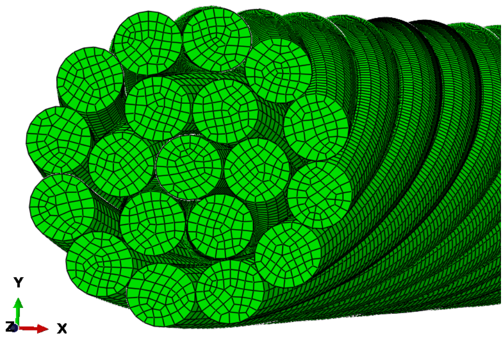

Figure 5.6: Mesh1

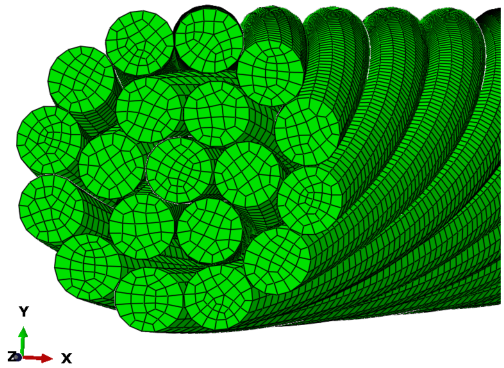

Figure 5.7: Mesh2

Mass Scaling

Through mass scaling, it is possible to analyse the model in its natural time period by artificially increasing the stable time increment. The following equations show how the stable time increment is related to the material density. The stability limit for the model is the minimum stable time increment of all elements [52]. An estimate of this limit in the explicit dynamics procedure can be expressed as:

$$\Delta t = \frac{L^e}{c_d}$$

where L^e is the characteristic element length and c_d is the dilatational wave speed of the material. The dilatational wave speed for a linear elastic material with Poisson's ratio equal to zero is given by:

$$c_d = \sqrt{\frac{E}{\rho}}$$

where E is the elastic modulus and ρ is the material density.
According to the above equations, artificially increasing the material density by a factor of f^2 decreases the wave speed by a factor of f and increases the stable time increment by a factor of f. Two types of mass scaling are available in Abaqus/Explicit: fixed mass scaling and variable mass scaling. For the simulations in exam, the second method is adopted, by scaling only elements with element stable time increments below a user-specified value. This is appropriate for both quasi-static and dynamic analyses and it is useful for increasing the element stable time increment of the most critical elements. When the mesh of an analysis contains a few very small elements that control the stable time increment size, increasing the mass of only these controlling elements means that the stable time increment can be increased significantly, yet the effect on the overall

behavior of the model may be negligible.
When the global stability limit is increased, fewer increments are required to perform the same analysis, which is the goal of mass scaling. Scaling the mass, however, has exactly the same influence on inertial effects as artificially increasing the loading rate. Therefore, excessive mass scaling, just like excessive loading rates, can lead to erroneous solutions. Generally the maximum allowed increase of Δt is equal to 10%, i.e., if the stable time increment is $\Delta t = 1 \cdot 10^{-5}$, the maximum specified element-by-element stable Δt is euqual to $1 \cdot 10^{-4}$.

In the following, analysis performed are characterised by specifying where mass scaling approach and different types of mesh have been used.

5.2.1 Finite element simulations of strand

All performed strand simulations are here summarized, grouping the jobs according to the mesh type and then specifying the adopted mass scaling factor.

- **Mesh0**

Starting from *Strand3D_Mesh0* job (Steel material), three models are created in order to reproduce the process with the most mass scaling. These models are characterized by three different factors of mass scaling, in progression from highest to lowest.
For *Strand3d_SMA* job two mass scaling factors are tested. However, both analysis present a very low stable time increment (it is of the order of $1 \cdot 10^{-9}$ against $1 \cdot 10^{-7}$ related to *Strand3D* job) and also using a "strong" mass scaling factor (20% for *Strand3D_MS1_SMA*) these fail to complete the simulation time. Furthermore, analysing the output files generated by the analysis some "warnings" about VUMAT convergence are found (the material subroutine initially does not converge in austenite and martensite reversal Newton loop and in austenite only Newton loop).

- **Mesh1**

Two models characterised by Mesh1 discretization are created: *Strand3D_Mesh1* job for steel material and *Strand3D_Mesh1_SMA* for SMA material. Mass scaling is not necessary for the steel model, while to the second job a factor of 10% is applied. Despite the lower number of elements involved in this analysis, some problems are yet reported for SMA model. As for *Strand3d_SMA*, it presents a very low Δt and only 9 of 20 steps are completed within the available 24 hours of walltime. Analyzing the output files generated by the analysis some "warning" about VUMAT convergence are found (the material subroutine initially does not converge in austenite and martensite reversal Newton loop).

- **Mesh2**

To obtain a SMA model able to complete the simulation time, the numbers of total elements is further reduced, getting a mesh with approximately half of the Reference model nodes. Two jobs characterised by Mesh2 discretization are defined: *Strand3D_Mesh2* job for steel material and *Strand3D_Mesh2_SMA* for SMA material. In both cases mass scaling is not required and 20 of 20 completed steps are achieved.

3D strand FEA are summarized in Table 5.1. According to data reported in Table 5.1, relatively to SMA material, only *Strand3D_Mesh2_SMA* job can be considered in the comparison between SMA and steel strands. Comparing *Strand3D_Mesh0_MS1*, *Strand3D_Mesh0_MS2* and *Strand3D_Mesh0_MS3* output the negative effect associated with the use of a mass scaling of 10% is noticeable. For this reason and given the simulation progress for the *Strand3D_Mesh1_SMA* with a 10% scaled Δt, a further increase of the mass scaling is considered pointless (this will be better shown in section 5.3). In relation to steel material, almost all simulations have been completed, both for more refined Mesh0 and for less refined Mesh1 and Mesh2.

Job Name	Material	N°nodes	Walltime	M.Scaling	Step completed
Strand3D_Mesh0	Steel	$\cong 1 \cdot 10^6$	> 24 h	-	17 of 20
Strand3D_Mesh0_SMA	SMA	$\cong 1 \cdot 10^6$	> 24 h	-	0 of 20
Strand3D_Mesh0_MS1	Steel	$\cong 1 \cdot 10^6$	$\cong 4$ h	10 %	20 su 20
Strand3D_Mesh0_MS2	Steel	$\cong 1 \cdot 10^6$	$\cong 7$ h	5 %	20 su 20
Strand3D_Mesh0_MS3	Steel	$\cong 1 \cdot 10^6$	$\cong 13$ h	2.5 %	20 su 20
Strand3D_Mesh0_MS1_SMA	SMA	$\cong 1 \cdot 10^6$	> 24 h	20 %	7 su 20
Strand3D_Mesh0_MS2_SMA	SMA	$\cong 1 \cdot 10^6$	> 24 h	10 %	0 su 20
Strand3D_Mesh1	Steel	$\cong 7 \cdot 10^5$	$\cong 21$ h	-	20 of 20
Strand3D_Mesh2	Steel	$\cong 5 \cdot 10^5$	$\cong 7$ h	-	20 of 20
Strand3D_Mesh1_SMA	SMA	$\cong 7 \cdot 10^5$	> 24 h	10 %	9 of 20
Strand3D_Mesh2_SMA	SMA	$\cong 5 \cdot 10^5$	$\cong 9$	-	20 of 20

Table 5.1: 3D Strand FEA

The goal of the study is to compare SMA strand with steel strand response. However, only for two analysis characterised by the same mesh and the same mass scaling factor (in this case 0), valid output are obtained. Thus, the direct comparison between SMA and steel will be made through *Strand3D_Mesh2* and *Strand3D_Mesh2_SMA* output (PHASE B). Due to the reduced number of elements characterising Mesh2 models, consistency of their results may result uncertain if these are compared to those of Mesh0 models. In order to validate the comparison made in PHASE B and to estimate the error in using a model with $\cong 5 \cdot 10^5$ nodes rather than one with $\cong 1 \cdot 10^6$ nodes , this is preceded by a first control phase (PHASE A). Here, output related to different studied mesh for the steel material case are placed in parallel, highlighting the quantities of interest that will be considered in PHASE B.

Figure 5.8 shows the analysis scheme adopted to reach final SMA-Steel strand comparison.

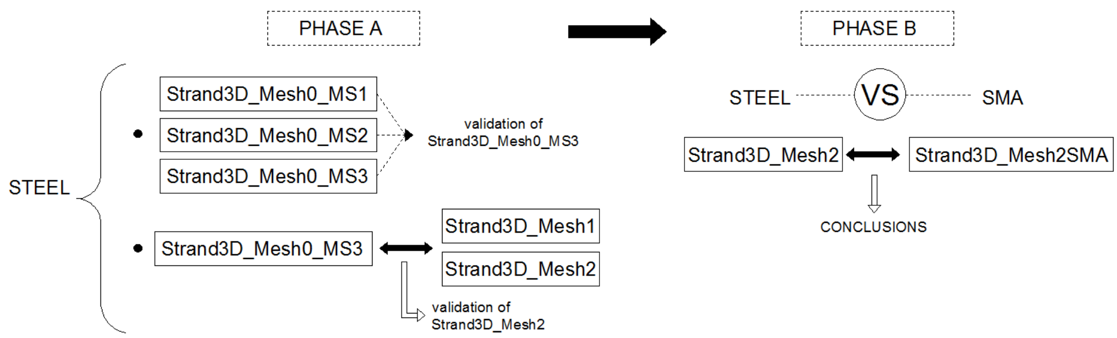

Figure 5.8: Analysis scheme for the comparison SMA-steel strand

Below, a summary of the characteristics of the Reference strand model is reported. It represents the base model for all overcited simulations, both for steel and SMA material.

Model features

- Geometry of 19 wires model: central core, first layer of 6 wires (wrapped in right-hand way), second layer of 12 wires (wrapped in left-hand way). The total strand length is equal to 62.8 mm with a total diameter of 3 mm;
- Material: conventional steel, with Young modulus E = 210000 N/mm^2, Poisson ratio $\nu =$ 0.3 and density $\rho = 7.86 \cdot 10^{-6}$ kg/mm^3;
- Mesh: the discretization is realised on parts. C3D8R element type is used for all three meshed models (Mesh0, Mesh1, Mesh2);
- Analysis steps:
  - step initial → encastre constraint definition;
  - step displacement → longitudinal displacement definition (0.8 mm Z-direction) and assignment of the sinusoidal transversal cycle displacement (10 mm Y-direction, 0 X direction) associated with the respective Amplitudes.
- Contact interaction: General Contact (Abaqus/Explicit);
- Output:
  - contact area and total force of contact → *contact-surf* surface;
  - history of nodal assigned displacements → *central node* set;
  - forces/reactions → *bottom-surf* surface;
  - forces/reactions → *up-surf* surface;
  - energy → *whole model* .

The same model is adopted for SMA strand, except for the following specifications:

- Material: ABQ_SUPER_ELASTIC_N3D (see Chapter 2, Table 2.1);
- Predefined field: within the Load module a *Temperature predefined field* is defined in step initial. *Constant through region* option is selected to obtain a constant temperature over a section. In the *Magnitude* text field, a magnitude of 300 K is entered as the temperature across the section.

5.3 SMA-Steel strands analysis results

Herein, the results of the comparisons performed during PHASE A and subsequently in PHASE B are shown. The output considered refer to the condition of inter-wires contact, the energy dissipated by strand, the history of displacement and the total axial force.

5.3.1 PHASE A: Steel strand FEA results

This preliminary phase focusing on steel strand FEA comparison. The output specified refer to *Strand3D_Mesh0_MS3* ,*Strand3D_Mesh1* and *Strand3D_Mesh2* jobs.
Strand3D_Mesh0_MS1 and *Strand3D_MS2* jobs are not taken into consideration due to their higher mass scaling factor compared to 2.5 % mass scaling applied to *Strand3D_Mesh0_MS3*. The problem studied for the strand consists of a quasi-static simulation. In a quasi-static analysis the kinetic energy of the deforming material should not exceed a small fraction of its internal energy, typically means 5–10%. Hence, examination of the energy content provides a measure to evaluate whether the results from an ABAQUS/Explicit simulation reflect a quasi-static solution, varying the mass scaling. Figure 5.9 compares the internal and kinetic energy histories for each case of mass scaling. Figure 5.9 shows a substantial overlap between the various case of mass scaling for

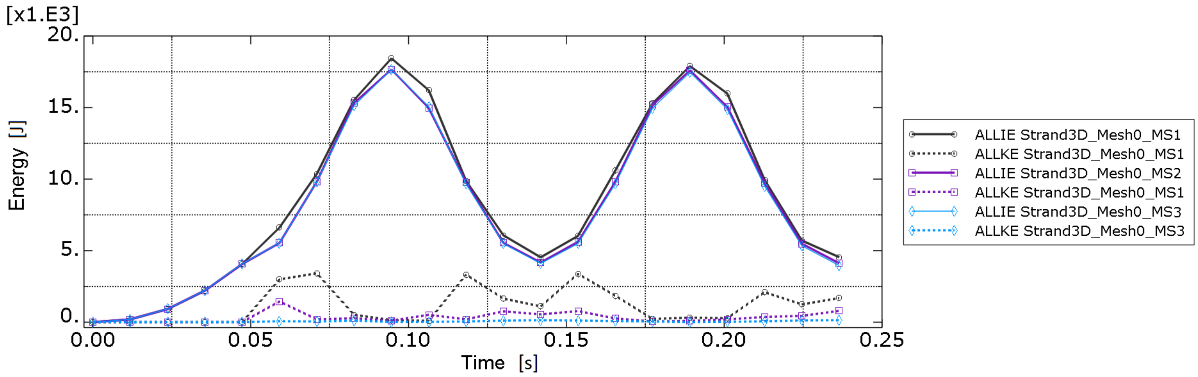

Figure 5.9: Kinetic and internal energy histories related to the Mesh0 steel models, for mass scaling of 2.5%, 5% and 10%

the ALLIE[10], while evident differences are observed for ALLKE[11]. The mass scaling case using a factor of 2.5% yields results that are not affected by the increased loading rate (see blue dashed line). The case with a mass scaling factor of 5% shows a high kinetic-to-internal energy ratio. The final case, with a mass scaling factor of 10%, shows evidence of strong dynamic effects with the kinetic-to-internal energy ratio unstable and quite high. A comparison of the final deformed shapes among the three cases demonstrates that the deformed shape is significantly affected in the last case. Thus, among Mesh0 models, the *Strand3D_Mesh0_MS3* analysis is the one that best approaches the problem studied for the Strand Reference model.

- **Area in contact**

Especially in contact as well as all other types of analyses, the solution improves as the mesh is refined. Coarse meshes can yield inaccurate results in analyses, such as problem in an appropriate identification of the contact area. This aspect is shown in Figure 5.10, where the three strand models with different mesh discretization are reported. Although the models of $\cong 1 \cdot 10^6$ and $\cong 7 \cdot 10^5$ present a contact area not perfectly coincident during simulation time, they show contained

[10]ALLIE : Total internal energy
[11]ALLKE : Kinetic energy

differences with a maximum error of 8% and a similar global trend. Conversely, the error registered for the model of $\cong 5 \cdot 10^5$ nodes is not in agreement with the more refined meshed models, reaching a maximum error of 27% if compared to *Strand3D_Mesh0_MS3* job. Given the excessive error related to the refinement of the mesh, contact area is not considered in Phase B comparison.

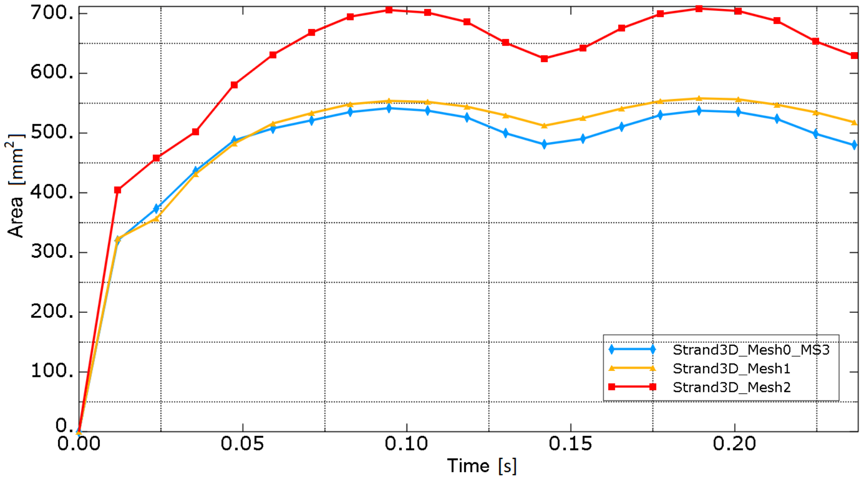

Figure 5.10: Steel FEA, Area in contact measured on the *contact-surf* surface

- **Total axial force**

The axial loading behavior of strand is investigated by an axial displacement of 0.8 mm applied on the *up-surf* surface. This value is reached at 0.05 s, then the pretension is kept constant throughout the simulation, during the application of the sinusoidal transversal cycle. Figure 5.11 shows the total axial force obtained through stresses integration over the strand cross section. The values from the less refined mesh models tend to agree with that of *Strand3D_Mesh0_MS3* job. The maximum percentage of deviation between *Strand3D_Mesh1* and *Strand3D_Mesh2* jobs with the model of $\cong 1 \cdot 10^6$ nodes is found to be 4.5% and 6% respectively.

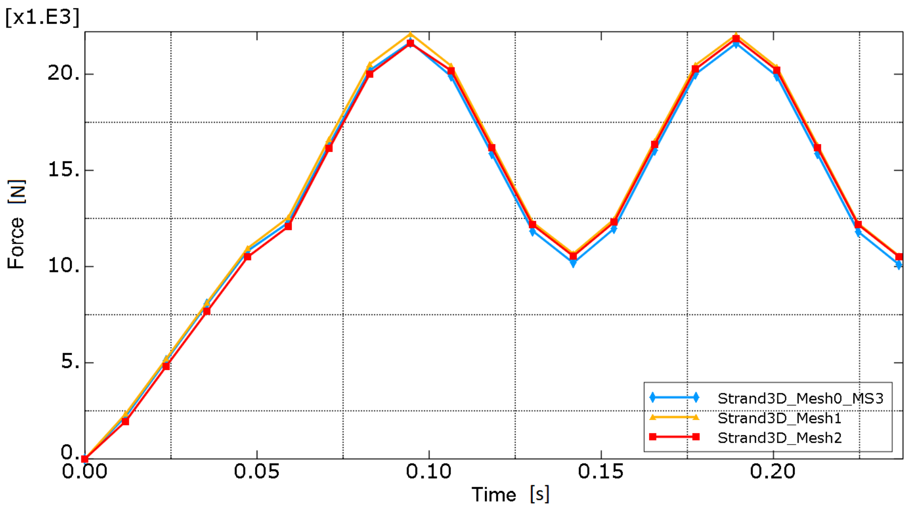

Figure 5.11: Steel FEA, Total axial force measured on the *up-surf* surface

- **Total transversal force**

A further comparison of Mesh0,Mesh1 and Mesh2 models is carried out on total transversal force calculated through stresses integration over the strand cross section. As for the axial force case, curves reported in Figure 5.12 have a generally coincident trend; also for the *Strand3D_Mesh2* job there isn't a strong discrepancy with the dense mesh model. The maximum percentage of deviation between *Strand3D_Mesh1* and *Strand3D_Mesh2* jobs with the model of $\cong 1 \cdot 10^6$ nodes is found to be 7.8% and 8% respectively.

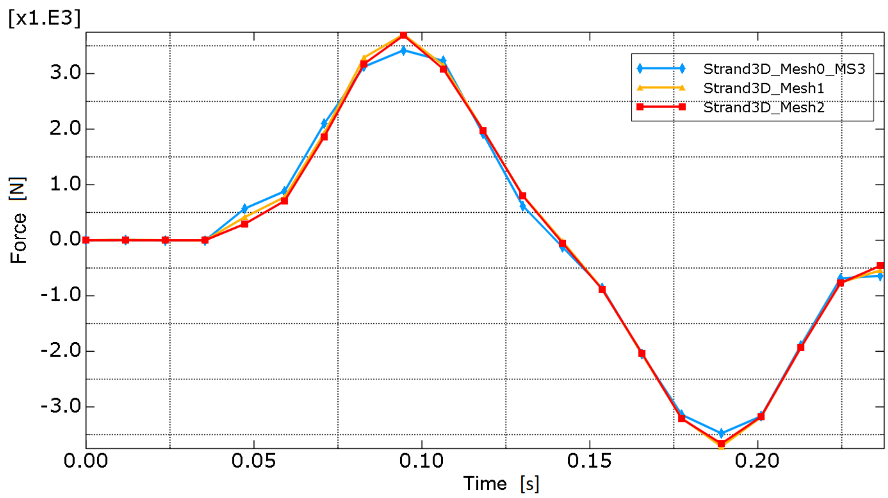

Figure 5.12: Steel FEA, Total transversal force measured on the *up-surf* surface

- **Frictional dissipation**

Among the energy output obtained for the performed jobs, the energy dissipated by friction is evaluated in Figure 5.13. The maximum percentage of deviation between *Strand3D_Mesh1* and *Strand3D_Mesh2* jobs with the model of $\cong 1 \cdot 10^6$ nodes is found to be 14% and 11% respectively.

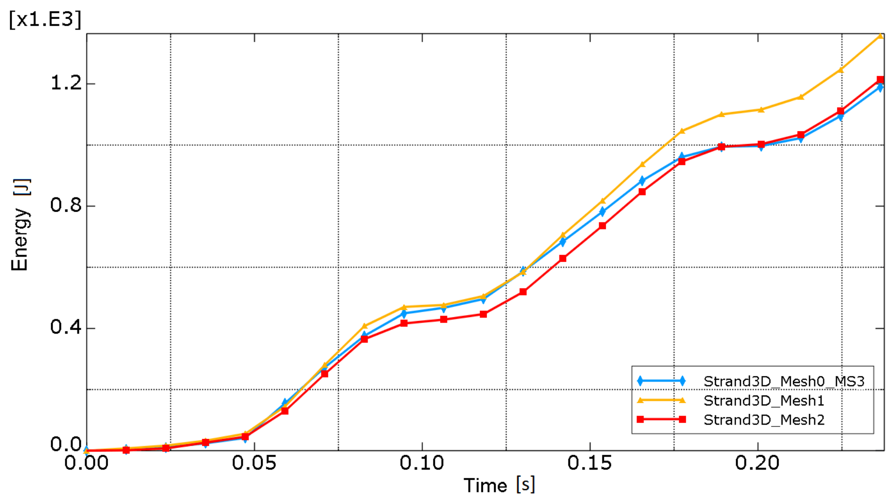

Figure 5.13: Steel FEA, Frictional energy dissipation on the *whole model*

Although these errors are not trivial, evaluating energy output it needs to consider the influence of mass scaling use in *Strand3D_Mesh0_MS3* simulation. Mass scaling may have caused dynamic effects that could have altered the actual frictional energy curve. Despite this, the three curves are substantially in agreement and for comparison purposes this output can be taken into account.

Some specific results related to the three types of mesh used to model the strand have been reported here. Figures above show a good correlation between the model of $\cong 1 \cdot 10^6$ and those with reduced mesh. Specifically, *Strand3D_Mesh2* results can be considered acceptable to represent the behavior of a steel strand subjected to a load case rather generic. Although there are percentage of error between the *Strand3D_Mesh2* and *Strand3D_Mesh0_MS3* output, these are adequate to the purpose of the comparison made in PHASE B. Having to do a comparison in terms of materials, steel and SMA, the degree of accuracy found in results of the $\cong 5 \cdot 10^5$ nodes model is considered suitable. As anticipated in section 5.2, the Mesh1 has not provided comparable results for the case of SMA strand; curves relating to *Strand3D_Mesh1* job have anyway been reported in order to provide a more complete comparison.

5.3.2 PHASE B: Comparison between steel and SMA strand

This phase focusing on comparison between steel strand and SMA strand. The output specified refer to *Strand3D_Mesh2* and *Strand3D_Mesh2_SMA* jobs. Referring to what obtained during phase A, the quantities investigated are the axial/transversal force produced on the strand and dissipation energy rates.

- **Total axial force**

In Figure 5.14 the total axial force measured on the *up-surf* surface is reported. From the inspection of the figure it is possible to see a wide gap between the steel curve and SMA curve. Considering the maximum value of Y coordinate, the axial force magnitude for the SMA strand is about a quarter of steel strand stessing force.

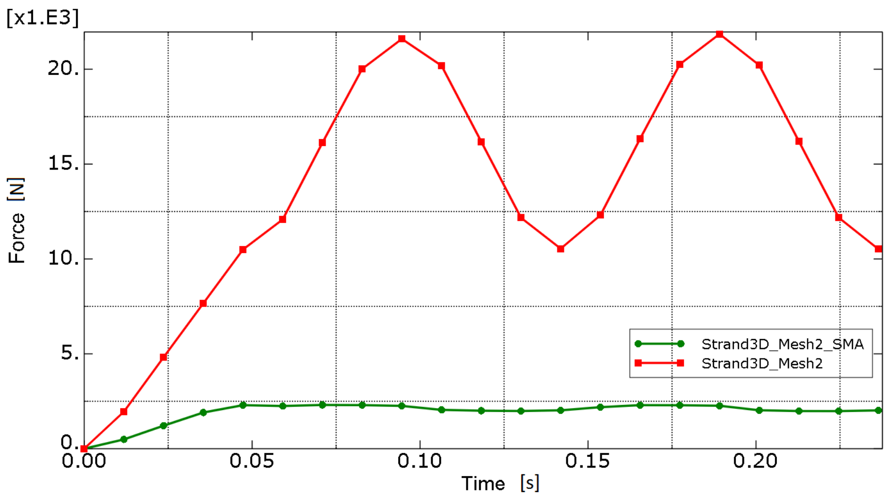

Figure 5.14: Steel and SMA FEA, Total axial force measured on the *up-surf* surface

- **Total transversal force**

In Figure 5.15 the total transversal force measured on the *up-surf* surface is reported. As expected, also in this case the steel curve is much greater than SMA curve. From figure 5.15 it is possible to note that SMA and steel curves converge when strand is only subjected to traction stress (at Δt going from 0 to 0.047 s and at $\Delta t \cong 0.14$ s).

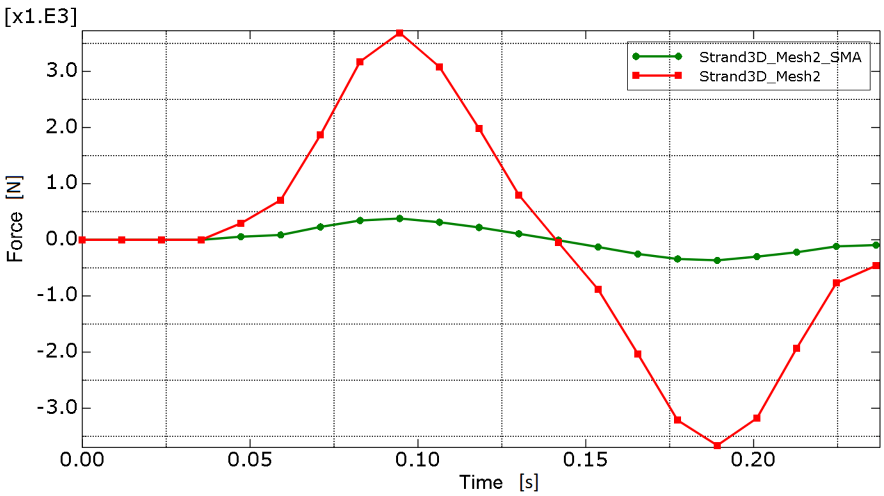

Figure 5.15: Steel and SMA FEA, Total transversal force measured on the *up-surf* surface

- **Frictional and plastic dissipation**

Among the energy output obtained for the performed jobs, the energy dissipated by friction (ALLFD) and plastic deformation (ALLPD) are evaluated.

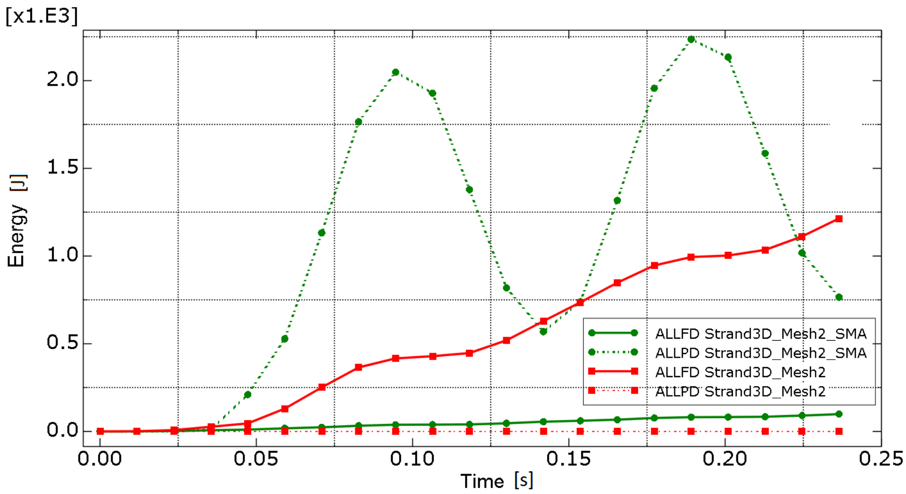

Figure 5.16: Steel and SMA FEA, Frictional and plastic dissipation energy on the *whole model* related to steel and SMA analysis

Figure 5.16 shows the two energy curves both for steel and SMA case, with continue and dash dot line respectively used for frictional dissipation and plastic dissipation. From the inspection of the figure is possible to note a plastic dissipation equal to zero for steel material, while this source of energy dissipation is predominant for SMA material. On the contrary, in the case of the frictional dissipation this is greater in steel strand rather than SMA strand. ALLFD of steel section presents a monotonic trend and shows two plateau nearby the inversion displacement cycle points (corresponding to $\Delta t \cong 0.09$ s and $\Delta t \cong 0.19$ s). In the neighbourhood of these points the ALLFD energy remains constant. This is linked to the strand velocity direction inversion. Within this range (placed near the maximum wire displacement position) there is the transition from kinematic friction to static one. Thus, given the absence of inter-wires relative displacement, here ALLFD energy does not increase. The wide gap between ALLFD and ALLPD in *Strand3D_Mesh2_SMA* is probably due to the trend of SMA wires to deform plastically rather than slide between them (phenomenon linked to friction dissipation). Relatively to SMA strand, it can be also observed that ALLPD curve shows two peaks, reached when the strand is in the maximum deformed shape.

Frictional and plastic rate are summed and plotted in Figure 5.17 (in steel case the total dissipated energy is represented only by the frictional component, given the zero value plastic term). As it can be seen from Figure 5.17 at $\Delta \cong 0.14$ s and $\Delta \cong 0.22$ s the two curves intersect. In these points SMA strand and steel strand present the same total dissipation energy, this occur when the strand returns in an horizontal position after an entire cyclic loading phase. This convergence between SMA and steel energies can be motivated by returning of the cable in its "original indisturbated" position (where it is subjected only to the tension load), considering however the share of energy loss during previous Δt. This fact shows that when persist in the cable only a traction stress, SMA and steel materials energetic behavior is practically equal in terms of dissipation. The curves values diverge when bending stresses are associated to traction ones.
The average value of dissipated energy by steel strand is $\cong$ 557 J, while for the SMA strand is $\cong$ 1150 J. The standard deviation σ is calculed for both material curves: for steel strand $\sigma = 396$, while for SMA strand $\sigma = 1154$.

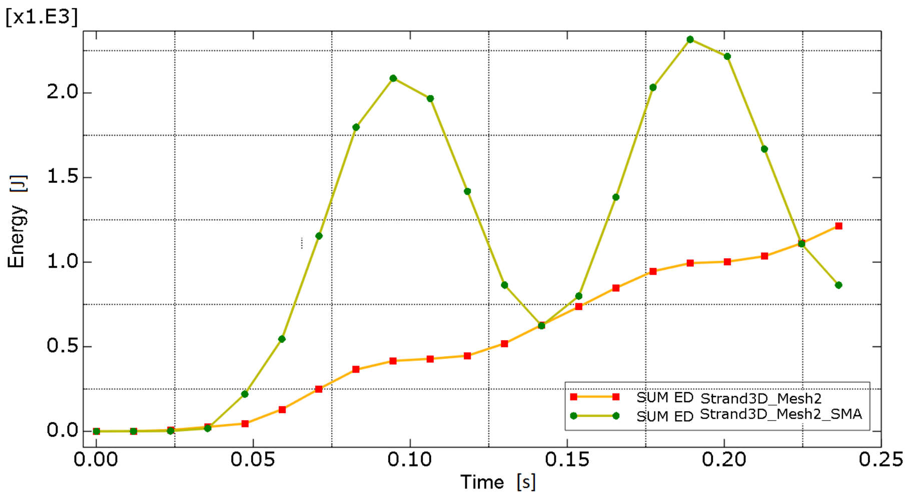

Figure 5.17: Steel and SMA FEA, Total dissipated energy on the *whole model* related to steel and SMA analysis

Chapter 6

Conclusions

The introductory overview about structural cables and SMA material has highlighted the points of strength linked to the simultaneous use of this two elements. Conventional and innovative properties, such as PE and SME, presented by SMA make efficient the employ of this material in civil engineering applications in which the use of strands and cables is addressed. Despite these advantages, a detailed characterization of SMA cables, overall from the FEM modeling point of view, is not found in the open literature.
This work continued the research about SMA strand, focusing on FEM modeling aspects through a particular strand problem. Initially an introduction on constitutive model and parameters chosen for SMA strand simulations has been reported. After a brief review on conventional 3D strand modeling, the Reference strand model considered in this thesis has been presented in detail. Following, the study has been carried out through two different directions: on the one end by the development of the simplified model and on the other one by the direct comparison of steel and SMA material through 3D strand models simulations.
In chapter 4 the simplified model has been described, focusing on elements type adopted for the discretization (shell and beam elements against 3D solid conventional elements)and on MPC Beam constraints, peculiar feature of the model. Simple tests have been performed on MPC Beam model (*Single_wire tests* and *Double_wire test*), comparing it with the equivalent 3D models. Tensile, bending and contact behavior of wires has been analysed. Taking a comprehensive overview on the results obtained, the simplified model resulted inadequate to be used in the comparison between SMA-steel materials. Although this is able to simulate the resultant forces acting on a strand, the model is incorrect in the evaluation of dissipated energy which is the principal output of interest in comparison SMA-steel strand behaviour. For this reason the evaluation of steel strand versus SMA strand response has been carried out only using conventional 3D modeling procedure.
In chapter 5, differences between conventional steel strands and SMA strands behavior have been highlighted, referring to the particular case of study of Reference strand model. All models considered are characterised by 3D solid elements mesh discretization. Due to the complexity of numerical analysis, high performance supercomputing tools have been used to run all strands jobs. Three different mesh has been implemented for the strand in exam, both for SMA and steel case. A preliminary phase (PHASE A) has been carried out in order to validate the jobs considered during the steel-SMA strand comparison phase (PHASE B). The direct comparison between SMA and steel has been made only on *Strand3D_Mesh2* and *Strand3D_Mesh2_SMA* jobs, due to the high computational cost and issues associated to Mesh0 and Mesh1 models. Evaluated output refer to frictional and plastic dissipation energy and total transversal/axial force calculated on strand extremity. From FEA results it can be observed that:

- Total axial force measured in steel strand has a greater magnitude than SMA strand case, as expected. The same result is registered for the total transversal force output;
- Comparing frictional and plastic dissipation energy, the plastic rate is null in steel material while in SMA strand this represents the predominant dissipation source;

- the plot of total dissipated energy on the whole model, for SMA and steel strand, shows a greater global dissipation in SMA device;
- Total dissipated energy curves converge at time instants in wich strand return in the orizontal position after an entire cyclic loading phase. In these points SMA strand and steel strand present the same total dissipation energy, since the source of dissipation energy is only the frictional rate for both materials.

Observing the work from a macroscopic point of view, some concluding remarks must be made. The simplified model here presented, has been developed without aiming to substitute the consistent and well known modeling based on 3D solid conventional finite elements. MPC Beam model shows a good agreement with 3D model in terms of kinematic displacements and contact, but this result is strictly relative to performed simple tests and specific parameters chosen for the model. To better validate the model it needs an accurate investigation on parameters calibration (shell thickness, correlation between thickness and wire dimensions, material definition for the shell part). Therefore, 3D modeling currently represents the most appropriate method in the prediction of structural cables response. Nevertheless, high computational cost associated to the use of 3D elements within a strand simulation is a real fact. When strands problems are associated to a material with a complex constitutive model such as SMA, the difficulty in managing simulations considerably increase. This has been underlined in chapter 5 by the poverty of completed simulations concerning SMA strand case, while having used high computational resources. Also computational parameters definition, necessary to run simulations involving a large number of DOFs, is not trivial, as the access to this type of supercomputing resources. The needs for more manageable methods for strands modeling is evident overall if, as in the present case, the research focusing on problems involving SMA cables applications.

Bibliography

[1] George A. Costello. *Theory of Wire Rope*. Springer, 2nd edition, 1997.

[2] McGraw-Hill. *McGraw-Hill Dictionary of Scientific and Technical Terms*. McGraw-Hill Companies, Inc., 6th edition, 2003.

[3] L. G. Khandros G. V. Kurdjumov. First reports of the thermoelastic behaviour of the martensitic phase of au-cd alloys. *Doklady Akademii Nauk SSSR*, 66:211–213, 1949.

[4] Christian Lexcellent. *Shape-memory Alloys Handbook*. Wiley-ISTE Ltd, 1st edition, 2013.

[5] E. Patoor et al. Shape memory alloys, part I: General properties and modeling of single crystals. *Mechanics of Materials*, 38:391–429, 2006.

[6] J. Lubliner F. Auricchio, Robert L.Taylor. Shape-memory alloys: macromodelling and numerical simulations of the superelastic behavior. *Computer methods in applied mechanics and engineering*, 146:281–312, 1997.

[7] K. N. Melton T. W. Duerig and D. Stöckel. *Engineering Aspects of Shape Memory Alloys*. Butterworth-Heinemann, 1st edition, 1990.

[8] J. Van Humbeeck. Damping capacity of thermoelastic martensite in shape memory alloys. *Journal of Alloys and Compounds*, 355:58–64, 2003.

[9] B. Reedlunna et al. Superelastic shape memory alloy cables: Part I – isothermal tension experiments. *International Journal of Solids and Structures*, 50:3009–3026, 2013.

[10] D. Cardone M. Dolce. Mechanical behaviour of shape memoryalloy s for seismic applications 1. martensite and austenite niti bars subjected to torsion. *International Journal of Mechanical Sciences*, 43:2631–2656, 2001.

[11] L. Janke et al. Applications of shape memory alloys in civil engineering structures - overview, limits and new ideas. *Materials and Structures*, 38:578–592, 2005.

[12] J. Van Humbeeck. Non-medical applications of shape memory alloys. *Materials Science and Engineering*, A273–275:134–148, 1999.

[13] G. Song et al. Applications of shape memory alloys in civil structures. *Engineering Structures*, 28:1266–1274, 2006.

[14] M.G. Castellano. Seismic protection of the basilica in San Francesco at Assisi. http://rin365.arcoveggio.enea.it/GLIS/HTMLgrdassisi/g5assisi.htm., 2000.

[15] Krstulovic-Opara et al. Active confinement of concrete members with self-stressing composites. *ACI Materials Journal*, 97:297–308, 2000.

[16] B. Reedlunna et al. Superelastic shape memory alloy cables: Part II – subcompnent isothermal responses. *International Journal of Solids and Structures*, 50:3027–3044, 2013.

[17] C.A. Rogers C. Liang. One-dimensional thermomechanical constitutive relations for shape memory materials. *Journal of intelligent Materials, System and Structure*, 1:207–234, 1990.

[18] C.A. Rogers C. Liang. A multi-dimensional constitutive model for shape memory alloys. *Journal of Engineering Mathematics*, 26:429–443, 1990.

[19] F.A.Cozzarelli E.J. Graesser. A proposed three-dimensional constitutive model for shape memory alloys. *Journal of intelligent Materials, System and Structure*, 5:78–89, 1994.

[20] F. Falk and P. Konopka. Three-dimensional landau theory describing the martensitic phase transformation of shape- memory alloys. *J. Phys.: Cond. Matter*, 2:61–77, 1990.

[21] S. Fu. Y. Huo and I. Muller. Thermodynamics of pseudoelasticity-an analytical approach. *Acta Mech*, 99:1–19, 1993.

[22] B. Raniecki and C. Lexcellent. R_L models of pseudoelasticity and their specification for some shape memory solids. *Europ.J. Mech. A/Solids*, 13:21–50, 1994.

[23] Keh Chih Hwang Qing Ping Sun. Micromechanics modelling for the constitutive behavior of polycrystalline shape memory alloys—I. derivation of general relations. *Journal of the Mechanics and Physics of Solids*, 41:1–17, 1993.

[24] Keh Chih Hwang Qing Ping Sun. Micromechanics modelling for the constitutive behavior of polycrystalline shape memory alloys—II. study of the individual phenomena. *Journal of the Mechanics and Physics of Solids*, 41:19–33, 1993.

[25] Dimitris C. Lagoudas. *Shape Memory Alloys Modeling and Engineering Applications*. Springer, 1st edition, 2008.

[26] J. Lubliner F. Auricchio. Generalises plasticity and shape-memory alloys. *J. Solid Structures*, 3:991–1003, 1995.

[27] Robert L.Taylor F. Auricchio. Shape-memory alloys: modelling and numerical simulations of the superelastic behavior. *Computer methods in applied mechanics and engineering*, 143:175–194, 1997.

[28] Simulia Copyright Dassault Systèmes. Umat-superelastic-plastic.pdf.

[29] Simulia Copyright Dassault Systèmes. Vumat-superelastic-plastic.pdf.

[30] Reali A. Auricchio F., Morganti S. Sma numerical modeling versus experimental results. In *Proceedings of the ESOMAT2009, 8th European Symposium on Martensitic Transformation 2009*, 2009.

[31] F. Auricchio. Numerical implementation of sma constitutive models. Technical report, Universitá degli Studi di Pavia Facoltá di Ingegneria Structural Mechanics Department, 2012.

[32] M. Labrosse A. Nawrocki. A finite element model for simple straight wire rope strands. *Computers and Structures*, 77:345–359, 2000.

[33] A.E.H. Love. Treatise on the mathematical theory of elasticity, 1944 chapter [18-19].

[34] Jones N. Utting, W. S. The response of wire rope strands to axial tensile loads: Part I. *International Journal of Mechanical Science*, 29(9):605–619, 1987.

[35] Jones N. Utting, W. S. The response of wire rope strands to axial tensile loads: Part II. *International Journal of Mechanical Science*, 29(9):621–636, 1987.

[36] Raoof M. Hobbs RE. Interwire sliding and fatigue prediction in stranded cables for tlp tethers. in: Behaviour of offshore structures. *New York: Hemisphere publishing/McGraw-Hill*, 2:77–99, 1982.

[37] Feyrer K. *Wire Ropes: Tension, Endurance, Reliability.* Springer-Verlag, Berlin, 2007.

[38] M. Bechtold. Modeling of steel ropes. In *proceedings of SIMULIA Customer Conference, Bridon International Ltd., Doncaster, UK, 2009*, Doncaster, UK, 2009. SIMULIA Dassault Sistèmes.

[39] Kasper RG. Carlson AD. A structural analysis of multi-conductor cable. Technical Report AD-767 963, Naval underwater systems center, distributed by National Technical Information Service, 1973.

[40] Chiang YJ. Characterizing simple stranded wire cables under axial loading. *Finite Elements in Analysis and Design*, 24:49–66, 1996.

[41] Walton JM. Jiang WG, Yao MS. A concise finite element model for simple straight wire rope strand. *International Journal of Mechanical Sciences*, 41:143–61, 1999.

[42] D. Durivlle. Modélisation du comportement mécanique de câbles métalliques. *Revue européenne des éléments finis.*, 7:9–22, 1998.

[43] D. Durivlle. Numerical simulation of entangled materials mechanical properties. *Journal OF Materials Science*, 40:5941–5948, 2005.

[44] N.D.Vidanović G.M.Kastratovic. Some aspects of 3d finite element modeling of independent wire rope core. *FME Transactions*, 39:37–40, 2011.

[45] C.E. İmrak C. Erdönmez, Ö. Salman. Characterizing the finite element analysis of nested helical geometry and test procedure for wire ropes. In *IV European Conference on Computational Mechanics Palais des Congrès, Paris, France,2010*, Paris, France, 2010.

[46] C. Erdönmez C.E. İmrak. On the problem of wire rope generation with axial loading. *Mathematical and Computational Applications.*, 15:259–268, 2010.

[47] Mohankumar K.V Shibu. G and Devendiran. S. Analysis of a three layered straight wire rope strand using finite element method. In *Proceedings of the World Congress on Engineering 2011 Vol III WCE 2011,July 6-8, 2011, London, U.K.*, London, U.K, 2011.

[48] Ali Semih Anil Ismail Gerdemeli, Serpil Kurt. Fatigue life analysis of wire rope strands with finite element method. *Scientific.net Material Science and Engineering*, 572:513–516, 2013.

[49] F. Degasperi V. Fontanari, B. Monelli UNITN A. Dallago. Structural behaviour of steel ropes subjected to heavy thermal transients simulating fire scenarios. In *Negli atti del 10° congresso OITAF 2011 Rio de Janeiro*, Brasil, Rio de Janeiro, 2011.

[50] N.D.Vidanović G.M.Kastratovic. Modeling and numerical analysis of the wire strand. *Journal of Naval Science and Engineering*, 5:30–38, 2009.

[51] SIMULIA Dassault Sistèmes. Abaqus analysis user's manual.

[52] SIMULIA Dassault Sistèmes. Getting started with abaqus: Keywords edition.

Special thanks

"Last but not least" al solito... credevate davvero che potevo liquidarvi tutti negli aknowledgemets??! In tal caso vi sbagliavate di grosso.
Inizierò subito col dirvi che questi tre anni a Pavia non sono stati per niente semplici e non parlo solo di esami o università. La spensieratezza con cui ho affrontato gli anni di triennale passati ad Ancona è stata spazzata via da una crescente e generale responsabilizzazione e da una (quasi sempre) sana competizione tra colleghi. Tutto ciò mi ha catapultato in giornate tutte uguali, passate sui libri (perchè se vuoi arrivare DEVI studiare) in cui le infinite partite a "ruspo" fatte sui tavoli della polifunzionale erano solo un vago e confuso ricordo. La lontananza dai miei amici marchigiani e non, si è fatta veramente sentire tanto, perchè quando uno è così impegnato ad "arrivare" non è facile crearsi delle amicizie nel poco tempo di vita sociale che la specialistica ti concede. Quindi un mio primo pensiero va a tutti i miei amici lontani, dal Sudafrica a "Montefargù", che in tutti questi mesi mi sono stati vicini magari con una semplice chiamata su skype, un messaggio o una mail in cui c'era la foto del cane appena comprato. Grazie veramente di cuore. D'altro canto questo cambiamento ha portato a tutta una serie di aspetti positivi. Qui a Pavia ho trovato un'ambiente di studio estremamente stimolante, dei professori competenti e preparati (tranne qualche eccezione) che mi hanno fatto appasionare ancora di più a quello che sto studiando ormai da anni e che spero sarà il lavoro della mia vita. Anche la parola Università qui ha assunto tutto un altro valore; tra celebrazioni, feste e goliardia collegiale ho scoperto un mondo che pensavo esistesse solo nelle università Americane o nel film scemi di MTV.
Beh, nel marasma generale, tra pro e contro, risate e pianti alle ore più variegate del giorno e della notte devo ringraziare 3 ragazze che ci sono state sempre, per me e con me. I miei "special thanks" vanno a Pota, Fransis e Gigia. Ognuna di loro è stata fondamentale per me e posso dire con estrema sicurezza che sono state le migliori e dico MIGLIORI conquiline che abbia mai avuto. Descrivere la loro vicinanza e raccontarvi ognuna di loro mi impegnerebbe in una tesi ben più lunga di questa. Fidatevi sulla parola, quando dico che sono speciali è perchè lo sono davvero.
Un grazie lo devo anche agli amici siciliani incontrati a Pavia (e già una bella fetta l'ho acchiappata) e ai miei colleghi ingegneri (si dai pure quelli di Idraulica). Giusto per citare qualcuno voglio ringraziare Charlie, Roberta, Cristiano, Vincenzo, Ornella, Moses, Mariani, il buon Pepes, Caramello etc. etc.. Abbiamo passato dei gran bei momenti insieme che non dimenticherò mai. Un grazie immenso a Yuling, mi hai stupito sin dal primo momento e sarà sempre così, unico. Un grazie a Poggi, senza di te non avrei mai potuto conoscere "il Denny".
Grazie alla mia famiglia, il loro sostegno mi ha permesso di fare tutto quello che ho fatto e incontrare tutte le belle persone che ho nominato. Grazie alle parole dei miei nonni che mi hanno sempre ricordato chi sono e chi devo essere. Grazie pure a Gabriella e Paolo: zia, senza di te ancora sarei a Pedaso ad aspettare qualcuno che mi viene a prendere; Paolo se non c'eri tu chi me la scriveva la tesi in inglese?
Il mio ultimo grazie va a Lorenzo. Solo lui sa cos'è significato scrivere questa tesi per me e non so ancora come abbia fatto a sopportarmi in questi mesi. Auguro a tutti di trovare una persona come lui, dubito questo pensiero possa realizzarsi. Grazie per gli "scossoni" che mi hai dato nei momenti più bui, quando il fato, la tecnologia e qualsiasi cosa potesse andar male andava peggio, senza di te non ce l'avrei mai fatta e sai che quello che dico è vero.

Valentina